Search for Anomalous Single Top Quark Production in Association with a Photon in pp Collisions at $\sqrt{s} = 8$ TeV

Reza Goldouzian

Supervisor:
Dr. Mojtaba Mohammadi Najafabadi

This thesis is presented as part of the requirements for the conferral of the degree:

Doctor of Philosophy in Experimental Particle Physics

Institute For Research in Fundamental Sciences (IPM)
School of Particles and Accelerators

2015

Abstract

This thesis reports the results of a first search for the flavor-changing neutral current (FCNC) through the anomalous production of single top quark in association with a photon due to the anomalous interactions of $tq\gamma$ ($q = u$ or c) in pp collisions. This search is performed using 19.8 fb^{-1} of data collected with the CMS detector at the center-of-mass energy of 8 TeV.

In this study we only concentrate on the muonic decay of the W-boson in top quark decay. The search is conducted in final states with an isolated muon, an isolated photon, jets, at most one of which is consistent with originating from the evolution of a b quark, and missing transverse momentum, corresponding to top quark decays, in which the W boson from the top quark decay is detected in the $\mu\nu$.

A multivariate classification approach is chosen to achieve a powerful discrimination between signal like events and standard model backgrounds. No evidence for the FCNC processes are observed. Upper limits at 95% confidence level on the strengths of the anomalous couplings are found to be $\kappa_{tu\gamma} < 0.025$ and $\kappa_{tc\gamma} < 0.091$. The corresponding upper bounds on the branching ratios are $Br(t \to u\gamma) < 0.013\%$ and $Br(t \to c\gamma) < 0.17\%$. The obtained upper bounds are the most stringent limit up to date.

Upper limits on the signal cross sections are also reported for a restricted phase-space region to provide results that can be more easily compared with theoretical predictions. Observed upper limits on the cross sections are found to be 47 fb and 39 fb at 95% CL for $tu\gamma$ and $tc\gamma$ production, respectively. The restricted phase space defined similarly to the final analysis phase-space and requiring exactly one identified b jet in the data. These are the first results on anomalous $t\gamma$ production within a restricted phase-space region.

Keywords: LHC, CMS, top quark, photon, FCNC

Dedication

"To my parents"

Acknowledgments

It is my pleasure to acknowledge those people who have helped me on the way to achieve the final goal, which manifests itself in this thesis. First and foremost, I would like to thank my advisor doctor Mojtaba Mohammadi Najafabadi for his support, advise and patience along the way. He always took the time to discuss my, certainly many, questions, and gave me guidance and suggestions to solve them.

I also extend my great thanks to professor Andrea Giammanco and doctor Lukas Vanelderen for believing in my abilities in fast-simulation projects. I learned a great deal from both of them about detector simulations in high energy physics. I am also grateful to CMS top and single top conveners especially professor Andreas Meyer and doctor Rebeca Gonzalez Suarez for their help and support.

I have learned and grown as a physicist while at the Institute For Research in Fundamental Sciences (IPM), in the School of Particles and Accelerators, thanks to the encouragement and support of the CMS group here. My gratitude goes to professor Hessamadin Arfaei for providing this environment.

Finally, I thank my brothers -Ali, Hossein- for the myriad ways they have supported me during my time as a graduate student. This dissertation is dedicated to my father Ahmad, from whom I inherited a love of science and technology, and to my mother Shahnaz, whose love and support will remain with me throughout my life.

Contents

Chapter 1

Introduction

The top quark is still the heaviest known elementary particle. Due to its large mass, the top quark plays a special role not only in understanding the details of the electroweak symmetry breaking in the standard model (SM) context but also in searching for new physics beyond the SM. Physics beyond the SM can manifest itself by altering the expected rates or properties of the top quark.

Within the SM, Flavour Changing Neutral Currents (FCNC) are absent at the tree level and are highly suppressed at higher orders by the GIM mechanism [1]. In top quark sector, the GIM suppression is much stronger than the bottom-quark sector due to the large mass of the top quark. For this reason, the SM predicts very small rates for the branching ratios of top quark FCNC decays to an up type quark and a neutral gauge bosons: $Br(t \to X(=\gamma, Z, g) + q(=c, u)) < 10^{-10}$ [2].

On the other hand, many models for new physics predict new heavy particles and interactions which can contribute to top quark FCNCs through the quantum loops and enhance the branching ratios of top quark FCNC decays orders of magnitude with respect to SM expectations. These new physics models include two higgs doublet models [3], exotic quarks [4], supersymmetry [5], or technicolour [6]. The predicted branching ratios for top quarks decaying to an up-type quark and a photon, Z boson, or gluon can be as large as 10^{-7} to 10^{-5} for certain regions of the parameter space in the mentioned models [2].

Although the branching ratio of top quark FCNC decays predicted in SM are far beyond the current experimental sensitivity, the observation of FCNC top decays with a branching ratio at the order of 10^{-5} are around the limit of the projected high luminosity reach at LHC [7]. Therefore, any evidence for FCNC in the top-quark

sector will be a clear indication of physics beyond the SM.

The LHC (Large Hadron Collider) is a top quark factory, producing large number of top quarks at designed center of mass energies and luminosity. This enables physicists to probe various properties of the top quark precisely. Searching for top quark FCNC interactions is one of the interesting topics which is followed by both ATLAS and CMS collaborations [8].

In order to search for physics beyond the SM through top quark FCNC processes, one can choose a specific new-physics scenario or follow a model-independent approach [9]. Experimental collaborations choose the latter approach to find independent signs of new physics or quantify the accuracy with which the new physics is excluded. FCNC interactions of top quarks would be probed through anomalous top quark decays, and through the anomalous production of top quark. From experimental point of view, each of the anomalous production and decay channels has its specific features and various analyses are defined to search for them by the experimental collaborations [8].

In this dissertation, a search is conducted for FCNC couplings of top quark with a light up-type quark and a photon. Using the effective Lagrangian approach, the $tu\gamma$ and $tc\gamma$ FCNC interactions are probed through the anomalous production of the single top quark in association with a photon at the LHC for the first time. The presence of a top quark and a high energy photon in the final state provides a clean signature for the signal channel.

This thesis is organized as follows: Chapter 2 introduces the SM, focusing on the electroweak sector. Various theoretical and experimental aspects of the the top quark FCNCs are also discussed in this section. Chapter 3 describes the details of the CMS detector. Chapter 4 gives an overview of the CMS event reconstruction chain and describes the physics objects used in the analysis. The performances of the detector and reconstruction procedures on data taken in 2012 are also shown. Chapter 5 describes the analysis strategy. Analysis strategy is started by explaining the signal, backgrounds processes, and the datasets. It continues with background estimations and signal extraction procedures and is finalized with presenting the world's best limit for the branching fraction, $Br(t \to q\gamma)$, with 95% confidence level.

Chapter 2

Theoretical motivations and experimental review

2.1 Particles and interactions

Particle physics is concerned with the ultimate constituents of matter at the smallest scale and the interaction among them. Elementary particles which are regarded as the most fundamental building block of matters has changed with time as technology and physicists′s knowledge has increased and improved. Fundamental particles of our own time are six flavors of leptons and quarks with spin-$\frac{1}{2}$, four gauge bosons with spin-1 and one spin-0 particle which are now defined as being point-like, without internal structure or excited states. At present, we know four fundamental interactions among these elementary particles: electromagnetic interaction, weak interaction, strong interaction and gravitational interaction. Among these interactions, the gravity is negligibly weak at elementary particle level and is usually out of game of particle physics.

The best theory which can explain all the phenomena of the particles in terms of the properties and interactions of these particles is called Standard Model (SM) of particle physics [10]. The SM, is a gauge theory based on the $SU(3)_C \otimes SU(2)_L \otimes U(1)_Y$ symmetry group. The strong, weak and electromagnetic interactions are described via the exchange of various spin-1 bosons amongst the spin-half particles.

The $SU(3)$ as color gauge group which describes strong interaction, is found to be unbroken. Quarks are assigned to the fundamental 3 representation and anti-quarks are assigned to the conjugate $3^\star$ representation. The eight massless spin-one

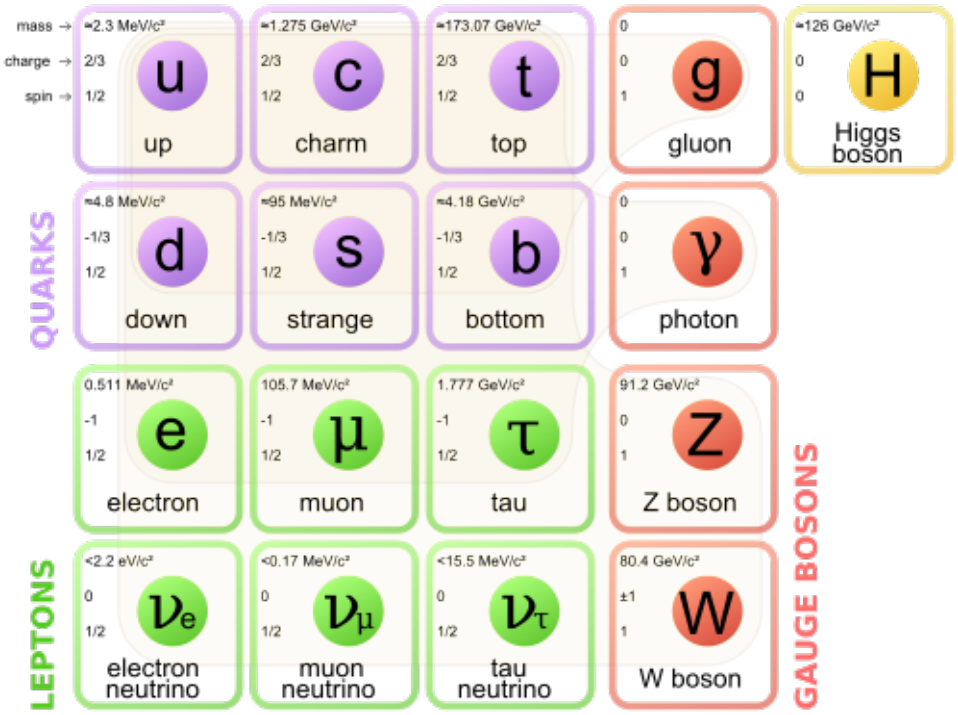

Figure 2.1: A table of all the elementary particles in the standard model in association with some of their properties. The faint gray lines indicate which gauge bosons interact with which fermions [11].

particles associated with $SU(3)_C$ are called gluon. The gluon carry color charges and can interact with each other. These self-interactions are responsible for many of the unique features of QCD, such as asymptotic freedom, chiral symmetry breaking, and color confinement.

In the SM, the left and right handed components of quark and lepton fields are assigned to different representations of the electroweak gauge group $SU(2)_L \otimes U(1)_Y$ to describe a chiral structure for the weak interactions. Thus, the left-handed fields are $SU(2)_L$ doublets, while the right-handed fields transform as $SU(2)_R$ singlets. The $SU(2)_L \otimes U(1)_Y$ gauge symmetry is broken spontaneously to the electromagnetic subgroup when the scalar field acquires a non-zero vacuum expectation value.

$$SU(3)_C \otimes SU(2)_L \otimes U(1)_Y \rightarrow SU(3)_C \otimes U(1)_{\text{QED}} \,. \tag{2.1}$$

The Spontaneous Symmetry Breaking (SSB) of the electroweak group generates the mass of the three weak gauge bosons (W^+, W^- and Z bosons) and fermions. The SSB ensures that photon remains massless and gives rise to the appearance of a scalar particle in the model called the Higgs boson.

Apart from the gauge and Higgs bosons that were discussed, SM includes 12 fermions which are classified according to how they interact. Those fermions which do not take part in the strong interactions are called leptons and those which take part in the strong interactions are called quarks by definition. So far there are known to be six flavour of leptons and quarks arranged into three generations. The flavours of leptons are denoted by e, μ, τ, ν_e, ν_μ and ν_τ and the flavour of quarks are the up, down, charm, strange, bottom and top quarks. In figure 2.1, some properties of the quarks, leptons and gauge bosons including mass, charge and spin are shown.

We focus on the interactions and properties that correspond to the $SU(2)_L \otimes U(1)_Y$ factor of the SM gauge group. The electroweak Lagrangian is given by:

$$\mathcal{L}_{EW} = \mathcal{L}_{gauge} + \mathcal{L}_{Higgs} + \mathcal{L}_{matter} + \mathcal{L}_{Yukawa} \tag{2.2}$$

The $\mathcal{L}_{gauge}$ which describes the kinetic term of the gauge fields is given by

$$\mathcal{L}_{gauge} = -\frac{1}{4} W_{A\mu\nu} W_A^{\mu\nu} - \frac{1}{4} B_{\mu\nu} B^{\mu\nu} \tag{2.3}$$

where $W_{A\mu\nu}$ (A = 1,2,3) and $B_{\mu\nu}$ are field strength tensors of the corresponding $SU(2)_L$ and $U(1)_Y$ gauge fields, respectively. This term includes both triple and quadratic self couplings of the electroweak gauge bosons.

The Higgs self-couplings and Higgs-gauge-bosons couplings are described by $\mathcal{L}_{Higgs}$ after the SSB which is given by

$$\mathcal{L}_{Higgs} = |D_\mu \phi|^2 + \mu^2 \phi^\dagger \phi - \lambda (\phi^\dagger \phi)^2 \tag{2.4}$$

where D_μ is the covariant derivative with the form

$$D_\mu = \partial_\mu - ig \frac{\overrightarrow{\tau}}{2} . \overrightarrow{W}_\mu - ig\prime \frac{\mathrm{Y}}{2} B_\mu \tag{2.5}$$

g and g$\prime$ are the the gauge coupling constants, Y is equal to -1 (-2) for left (right) components of the fermion fields and $\overrightarrow{\tau}$ is used to denote Pauli matrices.

The Yukawa Lagrangian has the form:

$$\mathcal{L}_{Yukawa} = -\sum_{i,j} \left(\Gamma_{i,j}^{(D)} \bar{Q}_{Li} \phi D_{Rj} + \Gamma_{i,j}^{(U)} \bar{Q}_{Li} \tilde{\phi} U_{Rj} + \Gamma_{i,j}^{(L)} \bar{L}_{Li} \phi l_{Rj} + \text{h.c.} \right) \tag{2.6}$$

where

$$Q_{L1} = \begin{pmatrix} u \\ d \end{pmatrix}_L, Q_{L2} = \begin{pmatrix} c \\ s \end{pmatrix}_L, Q_{L3} = \begin{pmatrix} t \\ b \end{pmatrix}_L, \tag{2.7}$$

$$L_{L1} = \begin{pmatrix} \nu_e \\ e^- \end{pmatrix}_L, L_{L2} = \begin{pmatrix} \nu_\mu \\ \mu^- \end{pmatrix}_L, L_{L3} = \begin{pmatrix} \nu_\tau \\ \tau^- \end{pmatrix}_L, \tag{2.8}$$

$$U_1 = u, U_2 = c, U_3 = t, D_1 = d, D_2 = s, D_3 = b, \tag{2.9}$$

$$l_1 = e^-, l_2 = \mu^-, l_3 = \tau^-. \tag{2.10}$$

The Yukawa couplings which are, in general, complex parameters are denoted by $\Gamma_{i,j}$. After the SSB, one can easily obtain the fermion mass matrix from $\mathcal{L}_{Yukawa}$. The mass matrix can be diagonalize by means of bi-unitary transformations and the elements of this diagonal matrix is correspond to the fermion masses. The basis of fields in which the mass matrix is diagonal is called mass eigenstate.

The interactions between the fermions and the electroweak gauge bosons are described by $\mathcal{L}_{matter}$

$$\begin{aligned} \mathcal{L}_{matter} &= \sum_i [i\bar{L}_{Li}\gamma^\mu D_\mu L_{Li} + i\bar{Q}_{Li}\gamma^\mu D_\mu Q_{Li} \\ &+ i\bar{U}_{Ri}\gamma^\mu D_\mu U_{Ri} + i\bar{D}_{Ri}\gamma^\mu D_\mu D_{Ri} + i\bar{l}_{Ri}\gamma^\mu D_\mu l_{Ri}] \end{aligned} \tag{2.11}$$

The right-handed fermion fields are singlets of $SU(2)_L$ and hence do not couple to W^i_μ. The $\mathcal{L}_{matter}$ can be written as the sum of the charged and neutral weak current interaction:

$$\begin{aligned} \mathcal{L}_{matter} &= \mathcal{L}_{CC} + \mathcal{L}_{NC}, \\ \mathcal{L}_{CC} &= \frac{ig}{\sqrt{2}}\left[W^+_\mu\left(\bar{\nu}_m\gamma^\mu P_L e_m + \bar{u}_m\gamma^\mu P_L d_m\right) + W^-_\mu\left(\bar{e}_m\gamma^\mu P_L\nu_m + \bar{d}_m\gamma^\mu P_L u_m\right)\right], \\ \mathcal{L}_{NC} &= \sum_f ieA_\mu\bar{f}\gamma^\mu f + \frac{ie}{\sin\theta_W\cos\theta_W}\sum_f Z_\mu\bar{f}\gamma^\mu(g_V + \gamma_5 g_A)f \end{aligned} \tag{2.12}$$

where θ_W is called weak mixing angle (Weinberg angle) and g_V and g_A values are given in Table 2.2. The electroweak gauge bosons are written in terms of the mass

eigenstates

$$W_\mu^1 = \frac{1}{\sqrt{2}}\left(W_\mu^+ + W_\mu^-\right) \qquad W_\mu^2 = \frac{-i}{\sqrt{2}}\left(W_\mu^- - W_\mu^+\right)$$
$$W_\mu^3 = Z_\mu \cos\theta_W + A_\mu \sin\theta_W \qquad B_\mu = A_\mu \cos\theta_W - Z_\mu \sin\theta_W \tag{2.13}$$

The observed states are mass eigenstates which are different from the weak eigenstates. To write the interactions in terms of the mass basis of the fermion fields we need to transform the fields using two unitary matrices as was discussed previously. Because of the unitarity of the transformation matrices, it is verified that the form of the neutral current interactions are not changed by the process of rotating to the mass eigenstate for the fermion fields. Therefore, we do not have flavour-changing neutral-currents at the tree level in the SM.

fermion	Q	g_V	g_A
ν_e, ν_μ, ν_τ	0	+0.25	+0.25
e, μ, τ	-1	-0.0189	-0.25
u,c,t	$+\frac{2}{3}$	+0.0959	+0.25
d,s,b	$-\frac{1}{3}$	-0.1730	-0.25

Table 2.1: Neutral-current charges of the fermion.

Since there is no mass term for neutrinos [1], the neutrino fields can be redefined while their kinematic terms do not change. Therefore, there is no flavor mixing between the leptons in the weak charged current interactions. The $\mathcal{L}_{CC}$ in mass basis can be written as

$$\begin{aligned}\mathcal{L}_{CC} &= \frac{ig}{\sqrt{2}}[W_\mu^+ \left(\bar{\nu}'_m \gamma^\mu P_L e'_m + V_{mn}\bar{u}'_m \gamma^\mu P_L d'_n\right) \\ &+ W_\mu^- \left(\bar{e}'_m \gamma^\mu P_L \nu'_m + (V^\dagger)_{mn}\bar{d}'_m \gamma^\mu P_L u'_n\right)]\end{aligned} \tag{2.14}$$

V_{mn} is a unitary matrix called the Cabibbo-Kobayashi-Maskawa matrix (CKM matrix) which describes the mixing between different generations. Assuming the uni-

[1] In the Standard Model the neutrino masses are assumed to be zero. However, experimental evidence for neutrinos to be massive has been accumulated.

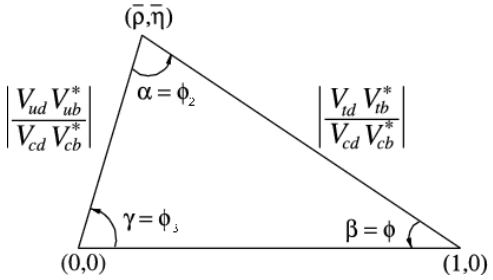

Figure 2.2: The unitary triangle gives a graphical representation of CKM elements.

tarity, the magnitudes of the CKM elements are [12]

$$V_{\rm CKM} = \begin{pmatrix} V_{ud} & V_{us} & V_{ub} \\ V_{cd} & V_{cs} & V_{cb} \\ V_{td} & V_{ts} & V_{tb} \end{pmatrix} = \begin{pmatrix} 0.97428 \pm 0.00015 & 0.2253 \pm 0.0007 & 0.00347^{+0.00016}_{-0.00012} \\ 0.2252 \pm 0.0007 & 0.97345^{+0.00015}_{-0.00016} & 0.0410^{+0.0011}_{-0.0007} \\ 0.00862^{+0.00026}_{-0.00020} & 0.0403^{+0.0011}_{-0.0007} & 0.999152^{+0.000030}_{-0.000045} \end{pmatrix} \quad (2.15)$$

the off-diagonal unitarity conditions impose the following equations

$$\begin{aligned} \mathbf{V}^*_{ud}\mathbf{V}_{us} + \mathbf{V}^*_{cd}\mathbf{V}_{cs} + \mathbf{V}^*_{td}\mathbf{V}_{ts} &= 0\,, \\ \mathbf{V}^*_{us}\mathbf{V}_{ub} + \mathbf{V}^*_{cs}\mathbf{V}_{cb} + \mathbf{V}^*_{ts}\mathbf{V}_{tb} &= 0\,, \\ \mathbf{V}^*_{ub}\mathbf{V}_{ud} + \mathbf{V}^*_{cb}\mathbf{V}_{cd} + \mathbf{V}^*_{tb}\mathbf{V}_{td} &= 0\,. \end{aligned} \quad (2.16)$$

which can be presented as a closed triangle in the complex plane, as is shown in Figure 2.2.

2.2 Top quark

2.2.1 Introduction

The top quark is the most recently discovered quark, which was discovered at the Fermilab Tevatron, a proton-antiproton collider at a center-of-mass energy of 1.8 TeV in 1995 [13–15]. The top quark was predicted as a weak-isospin partner of b quark in the standard model after the discovery of the b quark at 1977. The

presence of top quark could provide a natural way to suppress the experimentally not observed flavour-changing neutral current through the GIM mechanism [16] and make a renormalisable gauge theory of weak interactions by removing the anomaly.

Top quark mass was successfully predicted before its discovery through the radiative corrections in the standard model. Top quark can modify the W and Z masses and widths through the quantum loop corrections. Therefore, precise measurements of the W and Z boson properties provide a very good information to constraint the top quark mass. The most recent indirect measurements of the top quark mass using the Z-pole data, the W-boson mass and total width and several other electroweak quantities yields [17].

$$m_{top} = 179^{+12}_{-9} \tag{2.17}$$

The new direct measurement yields a top quark mass $173.21 \pm 0.51(\text{stat}) \pm 0.71(\text{sys})$ GeV [18]. Top quark is the heaviest of the known quarks and its mass has been measured with the highest precision comparing to any other quark. Due to the heavy mass of top quark, also much heavier than the W-boson, and short lifetime of the top quark, it decays before it can hadronize to a W boson and b quark with almost 100 percent branching fraction. This provides a unique opportunity to study the effects due to its spin through the angular correlations among its decay products.

In the Standard Model, the Yukawa coupling to the top quark ($y_t = m_t/v$, where $v \sim 246$ GeV is the vacuum expectation value), is very close to the unity. Because of this observation, it has often been speculated that new-physics might be accessed via top quark physics specially in the electroweak symmetry breaking scenario. Therefore, precise measurements of the top quark and its interactions may reveal effects from new physics.

2.2.2 Top quark production and decays

At the LHC, the dominant production mechanism of the top quark is through the top quark pair production mediated by the gluon. The representative Feynman diagrams are shown in Figure 2.3. The production of $t\bar{t}$ is the result of an interaction between the quarks and gluons which are the constituents of the incoming protons. Since the

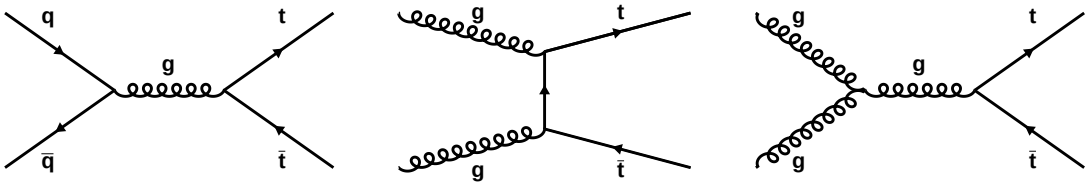

Figure 2.3: Representative Feynman diagrams for top pair production through the quark-quark annihilation and gluon-gluon fusion.

energy scale of the interaction is around the top quark mass, much larger than QCD scale, $t\bar{t}$ production at the LHC can be described by the quantum chromodynamic using perturbative approach.

At the LHC with $\sqrt{s} = 8$ (14) TeV, around 80 (90)% of the total cross section of $t\bar{t}$ is due to the gg fusion, while the remainder is mostly due to the qq annihilation. Since the minimal energy for $t\bar{t}$ production is $2m_t$ which leads to the $x = 0.05$ (0.025) (x is momentum fraction of proton carried by a parton) for the 8 (14) TeV LHC and the gluon distribution inside the proton increases more steeply towards small x than the valence and the sea-quark distributions.

In addition to the pair production, top quark can be produced singly through the electroweak interaction. There are three different channels for the electroweak single top production which are shown in Figure 2.4. All three processes involve the top quark charged current and allow to measure the CKM matrix element $|V_{tb}|^2$ directly. Therefore, the unitarity of the CKM matrix can be verified without any assumption on the number of generation and make a window to search for fourth generation. Measuring the properties of the standard model single top production is very important because it is a background to several new-physics scenarios and the presence of the new physics can make deviation from the SM prediction. For example, the existence of a flavour-changing neutral current $gu \to t$ would lead to the production of the single top quark with the signature very similar to the SM t-channel. At the LHC, the t-channel production mode is dominant, followed by the tW-channel. The s-channel production cross section is very low comparing to the huge background from $t\bar{t}$ with low chance to be observed at the 14 TeV LHC.

The top quark decays almost exclusively to a W boson and a b quark with the

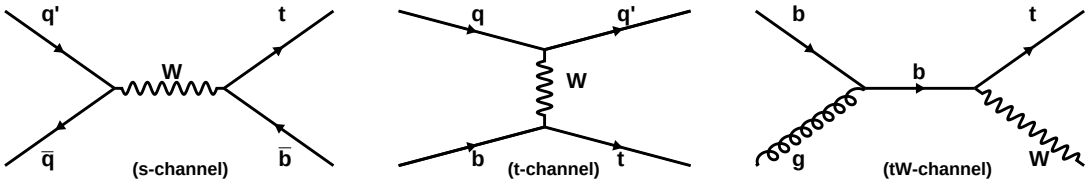

Figure 2.4: Representative Feynman diagrams for single top production at the LHC.

total width in the SM at NLO QCD [19]

$$\Gamma(t \to Wb) = \frac{G_F m_t^3}{8\pi\sqrt{2}} |V_{tb}|^2 \left(1 - \frac{m_W^2}{m_t^2}\right)^2 \left(1 + \frac{m_W^2}{m_t^2}\right) \left[1 - \frac{2\alpha_s}{3\pi}\left(\frac{2\pi^2}{3} - \frac{5}{2}\right)\right] \quad (2.18)$$

where G_F is the Fermi constant. Using $m_t = 172.5$ GeV yields $\Gamma_t = 1.33$ GeV corresponds to a very short lifetime $\tau_t = 5 \times 10^{-25}$ s. The W boson from top quark decay has leptonic and hadronic decay modes with the 10.8% and 67.6% branching ratio respectively. These modes lead to different characteristics of the $t\bar{t}$ and single top final state.

In top decay, the $t \to Ws$ ($BR \sim 0.2\%$) and $t \to Wd$ ($BR \sim 0.005\%$) decay modes are suppressed relative to $t \to Wb$ by the square of the CKM matrix elements.

2.3 Effective field theory and top quark anomalous interactions

2.3.1 Model-independent search for new physics

From the 1930s to the late 1960s, before the electroweak unification was understood, the weak interactions were described by an effective low energy description called 4-Fermi theory. Although the fundamental electroweak theory was not known at that time the 4-Fermi theory could present a very accurate phenomenological description of the weak interactions at low energies by introducing non-renormalizable dimension-6 operators. The value of the Fermi constant G_F, obtained from the precise measurement of the muon decay rate, was used to find the energy scale in which the new physics would appear and that was the mass of the W and Z boson. Therefore, the effective approach can be viewed as a low energy description of the new physics with the heavy states.

As the 4-Fermi effective theory is corresponding to the low energy limits of electroweak theory, the well proven SM would be the low energy limit of a new physics model. If we knew the complete fundamental theory at high energy scales, we could find the effective theory at an arbitrary scale by integrating out the heavy fields (compared to SM) at different energy scale from the theory. The effective field theory at low energy would be an infinite tower of terms of higher dimensions operators which are an $SU(3)_C \otimes SU(2)_L \otimes U(1)_Y$ symmetric built from standard model fields. This is a "top-down" application of the effective field theory [20]. If the theory at high energy respects the SM gauge symmetries, same operators will be obtained at low energy for different theories. The difference between theories will be reflected in the coupling constant and numerical factors associated with each operator.

Since the complete fundamental theory is unknown, we need to use the "bottom-up" approach of the effective field theory. In this approach, the SM Lagrangian is extended by introducing higher dimension operators which have coefficients of inverse powers of mass and they are suppressed by powers of the new physics scale Λ. Therefore, the higher the energy scale of new-physics, the smaller the effects on low-energy experiments.

The effective coupling constants of these operators should be determined by the experiments. The observation of any deviation from the prediction of the SM will require a non-zero value of some effective coupling constants. The value of the effective coupling constants can distinguish between different beyond standard model scenarios.

As was discussed, the higher dimension operators contain the power of the new physics scale in the denominator. Where is the energy scale of the new physics? Is it close to the electroweak scale? or somewhere between electroweak scale and plank scale? FCNC processes can present an interesting clue about this fundamental question.

2.3.2 Dimension-six operators with top quark FCNC interactions

The effective Lagrangian can be written as a series, such that

$$\mathcal{L} \;=\; \mathcal{L}^{SM} \;+\; \frac{1}{\Lambda}\mathcal{L}^{(5)} \;+\; \frac{1}{\Lambda^2}\mathcal{L}^{(6)} \;+\; O\left(\frac{1}{\Lambda^3}\right) \quad , \tag{2.19}$$

where $\mathcal{L}^{SM}$ is the SM Lagrangian of dimension four and $\mathcal{L}^{(5)}$ and $\mathcal{L}^{(6)}$ contain all the dimension five and six operators. All terms are invariant under the $SU(3)_C \otimes SU(2)_L \otimes U(1)_Y$ gauge symmetries of the SM. There is just one allowed term in $\mathcal{L}^{(5)}$ considering the demanded symmetries which breaks lepton number conservation and generates Majorana mass for left-handed neutrinos. Assuming lepton and baryon number conservation, a list of the dimension six operators are given in References [21, 22]. We will focus on the operators which lead to top quark FCNC interactions. The operators can be expressed as [23, 24]

$$\begin{aligned} O^{ij}_{UG\phi} &= C^{ij}_{uG\phi}\,(\bar{Q}_{Li}\lambda^a\sigma^{\mu\nu}U_{Rj})\tilde{\phi}\,G^a_{\mu\nu}\,, \qquad O^{ij}_{QG} = C^{ij}_{QG}\,\bar{Q}_{Li}\lambda^a\gamma^\mu D^\nu Q_{Lj}G^a_{\mu\nu}\,, \\ & \qquad\qquad\qquad\qquad\quad O^{ij}_{UG} = C^{ij}_{UG}\,\bar{U}_{Ri}\lambda^a\gamma^\mu D^\nu U_{Rj}G^a_{\mu\nu}\,. \end{aligned} \tag{2.20}$$

$$\begin{aligned} O^{(3,ij)}_{\phi Q} &= C^{(3,ij)}_{\phi Q} i(\phi^\dagger\tau^I D_\mu\phi)(\bar{Q}_{Li}\gamma^\mu\tau^I Q_{Lj})\,, & O^{ij}_{QW} &= C^{ij}_{QW}\,\bar{Q}_{Li}\gamma^\mu\tau^I D^\nu Q_{Lj}W^I_{\mu\nu}\,, \\ O^{(1,ij)}_{\phi q} &= C^{(1,ij)}_{\phi Q} i(\phi^\dagger D_\mu\phi)(\bar{Q}_{Li}\gamma^\mu Q_{Lj})\,, & O^{ij}_{QB} &= C^{ij}_{QB}\,\bar{Q}_{Li}\gamma^\mu D^\nu Q_{Lj}B_{\mu\nu}\,, \\ O^{ij}_{\phi U} &= C^{ij}_{\phi U} i(\phi^\dagger D_\mu\phi)(\bar{U}_{Ri}\gamma^\mu U_{Rj})\,, & O^{ij}_{UB} &= C^{ij}_{UB}\,\bar{U}_{Ri}\gamma^\mu D^\nu U_{Rj}B_{\mu\nu}\,, \\ O^{ij}_{UW} &= C^{ij}_{UW}\,(\bar{Q}_{Li}\sigma^{\mu\nu}\tau^I U_{Rj})\tilde{\phi}\,W^I_{\mu\nu}\,, & & \\ O^{ij}_{UB\phi} &= C^{ij}_{UB\phi}\,(\bar{Q}_{Li}\sigma^{\mu\nu}U_{Rj})\tilde{\phi}\,B_{\mu\nu}\,, & & \end{aligned} \tag{2.21}$$

where $i, j = 1, 2, 3$ are the flavour indices and C^{ij}_x are complex dimensionless couplings. Here $\bar{Q}_{Li}$, U_{Ri} and D_{Ri} are the quark fields which are introduced in Section 2.1.

Operators which contribute to FCNC decays of the form $t \to u(c)g$ and effect the strong sector are expressed in equation 2.20. Operators in equation 2.21 are analogous to those of 2.20 in the electroweak sector which contribute to top decays of the form $t \to u(c)\gamma$ and $t \to u(c)Z$. The hermitian conjugate of these operators should also be included in the effective Lagrangian.

All operators in the left columns of equations 2.21, 2.20 yield γ^μ and $\sigma^{\mu\nu}q_\nu$ terms, while those in the right columns give $k^\mu \equiv (p_i + p_j)^\mu$ and q^μ terms. Not all these operators are independent. The equation of motion can be used to remove redundant operators from the effective Lagrangian. It is shown in reference [23] that all effective operators which contribute to the trilinear fermion-fermion-gauge $(f_i f_j V)$ vertices involving a W or Z boson, a photon or gluon, only involve γ^μ and $\sigma^{\mu\nu}q_\nu$ terms, with $q = p_i - p_j$. It is proven that the O^{ij}_{QW}, O^{ij}_{QB}, O^{ij}_{UB}, O^{ij}_{QG} and O^{ij}_{UG} can be written in terms of the other operators in equations 2.21, 2.20 plus four-fermion interactions.

On the other hand, as was discussed in Section 2.3, we require that the well known low energy physics should not be affected by the new physics at high energies. In that sense, the O_{QG}, O_{QW} and O_{QB} operators which affect on bottom quark physics are highly constrained from B-physics. These operators are constructed from two left-handed $SU(2)$ doublets (left-left operators) in which the gauge structure can be felt stronger comparing to the operators with two right handed fermion fields. It is shown in Reference [25] that the left-left operators have no chance to be probed at LHC and if the LHC sees the anomalous FCNC decays, they must have came from the left-right or right-right operators.

The photon and Z FCNC interactions can be obtained from the combination of the O_{UW} and $O_{UB\phi}$ using equation 2.13. After electroweak SSB, the scalar field acquires a non-zero vacuum expectation value ($\phi_0 \to \phi_0 + v$) and the operators decompose into two pieces with and without Higgs scalar. Thus, the dimension 6 operators become a dimension 5 FCNC operators. The $O^{(1,ij)}_{\phi q}$, $O^{(3,ij)}_{\phi q}$ and $O^{ij}_{\phi u}$ operators just contribute to the $t \to qZ$ decay due to the cancellation of the photon term after SSB in these terms. Therefore, there is no γ^μ term in $tq\gamma$ Lagrangian [26].

The most general effective Lagrangian describing the top quark FCNC interaction with an up-type quark (u or c quark) and a gauge boson can be written as [2].

$$\begin{aligned} -\mathcal{L}_{eff} &= \frac{g}{2cos\theta_w}\bar{q}\,\gamma^\mu[X^L_{qt}P_L + X^R_{qt}P_R]t\;Z_\mu + \frac{g}{2cos\theta_w}\kappa_{qZ}\bar{q}\frac{i\sigma^{\mu\nu}q_\nu}{\Lambda}[z_L P_L + z_R P_R]tZ_\mu \\ &+ e\kappa_{q\gamma}\bar{q}\frac{i\sigma^{\mu\nu}q_\nu}{\Lambda}[\gamma_L P_L + \gamma_R P_R]tA_\mu \\ &+ g_s\kappa_{qg}\bar{q}\frac{i\sigma^{\mu\nu}q_\nu}{\Lambda}[g_L P_L + g_R P_R]T^a tG_{a\mu} + h.c. \end{aligned} \tag{2.22}$$

where e is the electron electric charge, g is the weak coupling constant, g_s is strong coupling constant, θ_w is the Weinberg angle, $P_{L,R} = \frac{1}{2}(1 \mp \gamma^5)$, $\sigma^{\mu\nu} = \frac{1}{2}[\gamma^\mu, \gamma^\nu]$ and the symbols $\bar{q}$ and t represent the up (or charm) and top quark spinor fields. The parameters X_{qt}, κ_{qZ}, $\kappa_{q\gamma}$ and κ_{qg} define the strength of the real and positive anomalous couplings for the current with photon, Z boson and gluon, respectively. The relative contribution of the left and right currents are determined by $X_{L,R}$, $z_{L,R}$, $\gamma_{L,R}$, $g_{L,R}$ and $h_{L,R}$ which are normalized as $|X_L|^2 + |X_R|^2 = 1$, $|z_L|^2 + |z_R|^2 = 1$, etc. In the Lagrangian, q is the momentum of the gauge boson and Λ is the new physics cutoff which by convention, is set to the top quark mass.

The partial widths for FCNC decays are given by [2]

$$\begin{aligned}
\Gamma(t \to qZ)_\gamma &= \frac{\alpha}{32\, s_W^2 c_W^2} |X_{qt}|^2 \frac{m_t^3}{M_Z^2} \left[1 - \frac{M_Z^2}{m_t^2}\right]^2 \left[1 + 2\frac{M_Z^2}{m_t^2}\right], \\
\Gamma(t \to qZ)_\sigma &= \frac{\alpha}{32 s_W^2 c_W^2} m_t^3 \frac{|\kappa_{qZ}|^2}{\Lambda^2} \left[1 - \frac{m_Z^2}{m_t^2}\right]^2 \left[2 + \frac{m_Z^2}{m_t^2}\right] \\
\Gamma(t \to q\gamma) &= \frac{\alpha}{4} m_t^3 \frac{|\kappa_{q\gamma}|^2}{\Lambda^2} \\
\Gamma(t \to qg) &= \frac{\alpha_s}{3} m_t^3 \frac{|\kappa_{qg}|^2}{\Lambda^2}
\end{aligned} \tag{2.23}$$

2.4 FCNC top quark decays in the standard model

In the 1950s, the universality of the weak coupling constant was exhibited after describing the pion, muon and neutron decays by a "vector minus axial vector" (V-A) type of interaction. In that sense, it was expected that all particles which decay through the weak interactions should have had the same life time. Experiments showed that the life time of the particles containing the strange quark did not follow the expectation and the strangeness non- conserving weak decays are relatively suppressed comparing to the strangeness conserving weak decays. For example, the life time of the $K^+ \to \pi^+\pi^0$ was measured to be 20 times longer than $\pi^+ \to \mu^+\nu$. The universality of weak interactions was contradicted by this observation. The universality of the weak interaction was resurrected by Cabibbo in 1963 [27] by introducing the Cabibbo angle which rotates the strangeness-conserving and strangeness-changing processes, keeping the total weak hadronic current unchanged

$$J_\mu^h = cos\theta_c J_\mu^0 + sin\theta_c J_\mu^0 \tag{2.24}$$

Experimentally, it could explain all strangeness-changing processes consistently with $sin\theta_c \simeq 0.26$. Therefore, weak interactions were again universal [28].

A further step was considering the neutral weak interaction. Generically, one would also expect charge currents and neutral currents of similar strength, in particular flavour-changing neutral currents. A strong suppression was observed in kaon FCNC decay mode quite early which was

$$\frac{\Gamma(K^+ \to \pi^+ \nu\bar{\nu})}{\Gamma(K^+ \to \pi^0 e^+ \bar{\nu}} < 10^{-5} \ll 1 \tag{2.25}$$

The weak processes were understood as transitions between different quark flavours when the quark substructure of hadrons had been noticed. In 1960s, one quark doublet was known and the hadronic current was written as

$$J^h_\mu = \bar{u}\gamma_\mu(1-\gamma^5)[d\cos\theta + s\sin\theta] \tag{2.26}$$

in which the combination of down and strange quark fields participates to the weak interaction. Given this point of view, the neutral current can be written in the form of

$$J^h_\mu = \bar{u}Mu + [\bar{d}\cos\theta + \bar{s}\sin\theta]M'[d\cos\theta + s\sin\theta] \tag{2.27}$$

where M and M' are some Dirac matrices. Clearly, the neutral currents contain some terms which lead to the strangeness-changing processes. This strangeness-changing neutral current predict the the ratio of 2.25 of order unity, in contradiction with observations.

In 1970, Glashow, Iliopuolos and Maiani proposed a new mechanism to solve this problem and is called the GIM mechanism [1]. Their idea had a surprising consequence that another quark has to exist with the quantum numbers of the up quark which is now called charm quark. The charm quark, couples to the orthogonal combination of the down and the strange quark $[s\cos\theta - d\sin\theta]$. The charged current becomes

$$J^{CC}_\mu = \bar{u}\gamma_\mu(1-\gamma^5)[d\cos\theta + s\sin\theta] + \bar{c}\gamma_\mu(1-\gamma^5)[s\cos\theta - d\sin\theta] \tag{2.28}$$

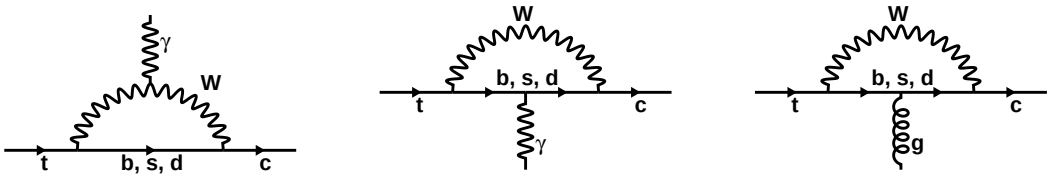

Figure 2.5: Flavour-changing neutral-current loops for $t \to c\gamma$. The third diagram contributes through its mixing.

and the neutral currents becomes

$$\begin{aligned} J_\mu^{NC} &= \bar{u}Mu + [\bar{d}\cos\theta + \bar{s}\sin\theta]M'[d\cos\theta + s\sin\theta] \\ &+ \bar{c}Mc + [\bar{s}\cos\theta - \bar{d}\sin\theta]M'[s\cos\theta - d\sin\theta] \\ &= \bar{u}Mu + \bar{c}Mc + \bar{d}M'd + \bar{s}M's \end{aligned} \tag{2.29}$$

From equation 2.29, we find that the neutral current is flavor diagonal and there is no FCNC at all at tree level. The GIM mechanism can be extended to the 3 generation of the quarks while the mixing is given by CKM matrix. Due to the unitarity of the CKM matrix the FCNC processes are forbidden at tree level. The FCNC processes can take place at loop level with the help of the flavour-changing vertices. An example of loop diagrams leading effectively to FCNC for the process $t \to c\gamma$ are depicted in figure 2.5. One should sum over all flavours of the intermediate quarks to obtain the $t \to c\gamma$ FCNC amplitude. The amplitude can be written as

$$\mathcal{A} = f(\frac{m_d^2}{m_W^2})\mathbf{V}_{td}^*\mathbf{V}_{cd} + f(\frac{m_s^2}{m_W^2})\mathbf{V}_{ts}^*\mathbf{V}_{cs} + f(\frac{m_b^2}{m_W^2})\mathbf{V}_{tb}^*\mathbf{V}_{cb} \tag{2.30}$$

where $f(\frac{m^2}{m_W^2})$ depends on the quark mass of the intermediate down-type quark. If the down-type quark masses were degenerate, exact cancellation occurs and the amplitude would vanish owing to CKM unitarity equation which was written in equation 2.16.

$$\mathcal{A} = f(\frac{m_d^2}{m_W^2})[\mathbf{V}_{td}^*\mathbf{V}_{cd} + \mathbf{V}_{ts}^*\mathbf{V}_{cs} + \mathbf{V}_{tb}^*\mathbf{V}_{cb}] = 0 \tag{2.31}$$

Due to the fact that the quark masses are not degenerated, the $t \to c\gamma$ FCNC amplitude is proportional to the mass splitting of the down type quarks. Similar arguments hold for the $b \to s\gamma$ FCNC decay, while the intermediate quarks are

up-type quarks. The mass differences between the up-type quarks are much larger than down-type quarks due to the large mass of the top quark. Therefore, top quark FCNC more strongly suppressed than bottom quark FCNC, for example $Br(b \to s\gamma) \sim 10^{-4}$ vs $Br(t \to c\gamma) \sim 10^{-13}$.

In order to see the suppression reason clearly, one can write the order of the top quark FCNC decay width as [29]

$$\Gamma(t \to \gamma\, c) \sim |V_{tb}^* V_{bc}|^2 \alpha\, G_F^2\, m_t\, m_b^4 \sim |V_{bc}|^2 \alpha_{em}^2 \alpha\, m_t \left(\frac{m_b}{M_W}\right)^4 \tag{2.32}$$

in which it is assumed that the loop amplitudes are controlled by the bottom quark. The fourth power of the mass ratio $\left(\frac{m_b}{M_W}\right)$ is responsible for the ultra large suppression of the FCNC decay width. The SM prediction of the top quark FCNC branching ratios are summarised in table 2.2.

	$Br(t \to q\gamma)$	$Br(t \to qZ)$	$Br(t \to qg)$
$q = u$	3.7×10^{-16}	8×10^{-17}	3.7×10^{-14}
$q = c$	4.6×10^{-14}	1×10^{-14}	4.6×10^{-12}

Table 2.2: Branching ratios for the top quark FCNC decays in the SM.

2.5 FCNC top quark decays in beyond standard models

The SM is a mathematically consistent, renormalisable quantum field theory which is consistent with all experimental facts and no significant hint of any physics beyond this model has been found. On the other hand, a lot of questions are left unanswered, Some problems and open questions of this kind related to the flavor physics are

- The neutrinos are massless in the SM contradicting experimental evidence for neutrino masses from neutrino oscillations.
- It does not have enough sources of CP violation to explain the observed ratio of the matter and antimatter.
- Why do we observe the fermions in three generations?

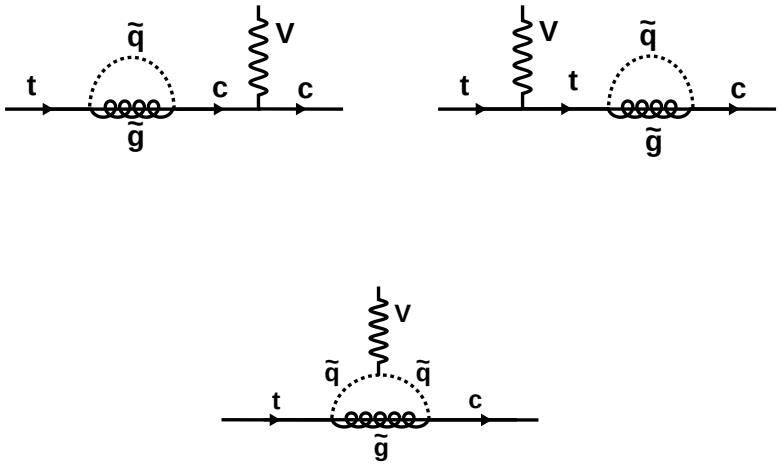

Figure 2.6: Feynman diagrams representing the top quark FCNC decays induced by supersymmetric QCD loops.

- Why are the off-diagonal elements of the CKM matrix so small?
- The quark masses are so small (except for the top quark) comparing to the electroweak vacuum expectation value.
- Does the top quark with mass near to the electroweak vacuum expectation value play a more fundamental role in the electroweak symmetry breaking mechanism?

There is an enormous range of new physics scenarios attempting to resolve the standard model problems. We will focus on the models that predict an enhancement on the top quark FCNC branching ratios.

The decays $t \to Vc$ ($V = \gamma$, Z, g) induced through loop process in minimal supersymmetric model were calculated for the first time in [30]. Suppersymmetric QCD violates flavor symmetry and there are flavour changing interactions between gluinos ($\tilde{g}$), squarks ($\tilde{q}$) and quarks (q) [31]. These QCD flavor changing interactions can contribute to the top quark FCNC decay through the loops. The diagrams for $t \to Vc$ through the suppersymmetric QCD loops are shown in figure 2.6. It is shown that the top quark FCNC decay width depends strongly to the gluino and squark masses. For example for $m_{\tilde{g}}, m_{\tilde{q}} < 120$ GeV, the new contributions can enhance the branching ratio of $t \to Vc$ as much as 3-4 order of magnitudes compared to the SM prediction.

In addition to the suppersymmetric QCD loop effects, the FCNC can be induced

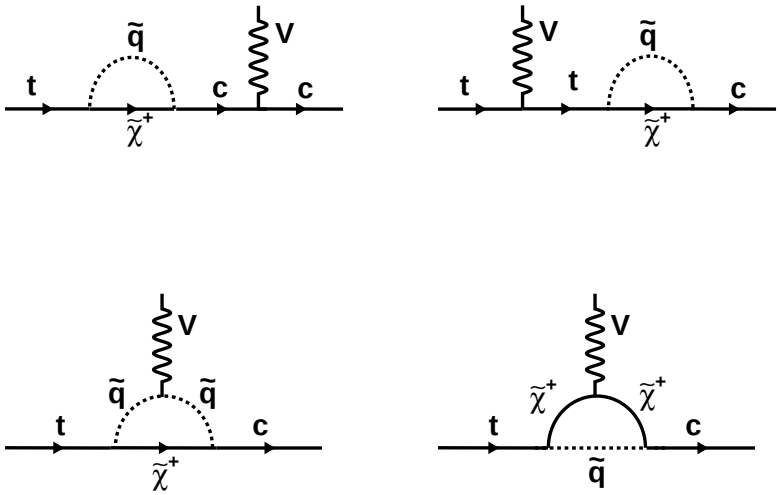

Figure 2.7: Feynman diagrams representing the top quark FCNC decays induced by supersymmetric chargino loops.

through the chargino loop. In reference [32], it is shown that the generation mixing can exist through the chargino ($\tilde{\chi}^+$), squark ($\tilde{q}$) and quark (q) interaction. Therefore, the FCNC top quark decay is possible through the chargino loop as is shown in figure 2.7. The contribution of the chargino loop to top quark FCNC decays also depends on the chargino and squark masses and other parameters of the minimal suppersymmetry model. The combined contribution of the QCD and chargino are roughly 10^{-6}, 10^{-9}, 10^{-8} for $t \to gc$, $t \to Zc$ and $t \to \gamma c$ respectively at the maximum level.

Several extensions of the SM involve an extended Higgs sector, with more than one Higgs doublet, such as supersymmetry, models with spontaneous CP violation and some grand unification theories [33]. The existence of two Higgs doublets leads to five physical states: the CP even neutral Higgs bosons h and H , the CP odd pseudoscalar A and two charged Higgs bosons $H^{\pm}$. Such a model has six free parameters: four Higgs masses (m_h, m_H, , m_A, $m_{H^{\pm}}$), the ratio of the two vacuum expectation values ($\tan\beta$) and a mixing angle (α) [30]. Charged Higgs bosons can contribute to the $t \to Vc$ processes through the loop and enhance the branching ratio. The branching ratio of the $t \to Vc$ decays depends on the charged Higgs mass and the value of the $\tan\beta$. The resulting branching ratios can be up to 10^{-4}, 10^{-7}, 10^{-6} for $t \to gc$, $t \to Zc$ and $t \to \gamma c$, respectively [34].

In many different new-physics scenarios the FCNC interactions can be induced through the loops in which new heavy particles or new interactions contribute. In

table 2.3, the predicted branching ratios of the top quark FCNC processes for some new physics models are summarised. More information can be found in the following references [6, 35–38].

	SM	QS	2HDM	FC 2HDM	MSSM	$\not{R}$ SUSY
$t \to uZ$	8×10^{-17}	1.1×10^{-4}	–	–	2×10^{-6}	3×10^{-5}
$t \to u\gamma$	3.7×10^{-16}	7.5×10^{-9}	–	–	2×10^{-6}	1×10^{-6}
$t \to ug$	3.7×10^{-14}	1.5×10^{-7}	–	–	8×10^{-5}	2×10^{-4}
$t \to cZ$	1×10^{-14}	1.1×10^{-4}	$\sim 10^{-7}$	$\sim 10^{-10}$	2×10^{-6}	3×10^{-5}
$t \to c\gamma$	4.6×10^{-14}	7.5×10^{-9}	$\sim 10^{-6}$	$\sim 10^{-9}$	2×10^{-6}	1×10^{-6}
$t \to cg$	4.6×10^{-12}	1.5×10^{-7}	$\sim 10^{-4}$	$\sim 10^{-8}$	8×10^{-5}	2×10^{-4}

Table 2.3: Branching ratios for top FCN decays in the SM, models with $Q = 2/3$ quark singlets (QS), a general 2HDM, a flavour-conserving (FC) 2HDM, in the MSSM and with R parity violating SUSY.

As was discussed in previous section, the FCNC decays of the top quark within the context of the SM are known to be extremely rare. This extremely tiny rate is far below the experimental reach of any present conceivable high luminosity machine. On the other hand, some of the new physics models may enhanced the top quark FCNC decays up to a detectable limit for some regions in their parameter space. Therefore, detection of any signal corresponds to the top quark FCNC processes would be a clear evidence for violations of the SM prediction and indicate the existence of the new physics beyond the SM.

2.6 Anomalous top quark production and decay at the LHC

The proton-proton Large Hadron Collider (LHC) is a top factory. The production of 56 million top pairs and 27 million single top events in 25 fb^{-1} of data at 7 and 8 TeV center of mass energy per LHC experiment, allows to study the top quark properties very precisely, and to search for its role in new physics in a comprehensive way.

The top quark FCNC processes as a window to new physics can be explored at the LHC in different ways. In order to be independent of the underlying new physics model which is responsible for the FCNC process, the effective Lagrangian approach

is chosen to search for the new physics signal as was discussed in section 2.3. The effective Lagrangian contributes to both production and decay of top quarks.

If the top quark FCNC anomalous couplings to the gauge bosons exist, its decay properties would be affected. One of the most prominent signatures of FCNC processes at the LHC, would be the direct observation of a top quark decaying into an up-type quark together with a photon, gluon or Z boson [39]. In order to have enough statistics, it is appropriate to search for top quark FCNC decays in $t\bar{t}$ events while one top decays to Wb as expected from the SM and the other decays anomalously to an up-type quark together with a neutral gauge boson as is shown in figure 2.8. Different decay modes has different signatures and search strategy that will be discussed in the next section.

FCNC interaction of top quarks can be probed through the anomalous production of top quark. Some interesting production processes where the effect of the FCNC coupling could be significant are:

- **Direct top quark production ($(2 \rightarrow 1)$ process):** The presence of tqg anomalous couplings lead to the production of a top quark ($u(c) + g \rightarrow t$) without any additional particle in proton-proton collision through the diagram in figure 2.9 (a) [40]. The signature of this process is different from the SM single top production where the top quark is always accompanied by other particles. The top quark is produced singly with transverse momentum arising only from initial state QCD radiation. Therefore, its decay products tend to be back to back in azimuth plane. Due to the larger parton distribution function PDF) of u quark in proton compared to the gluon and other sea quarks, the top quark is produced boostedly and its decay product will have smaller opening angle. The difference between PDF of u and $\bar{u}$ leads also to the production of top quark more than anti-top quark.

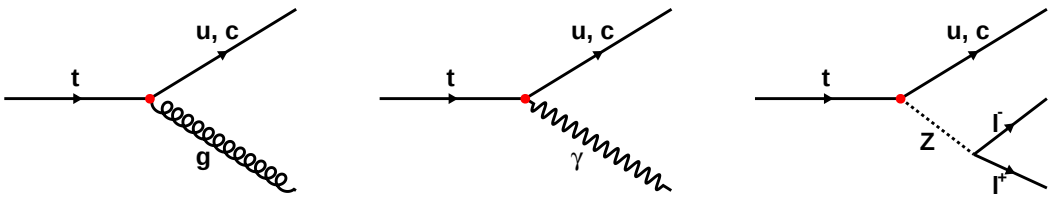

Figure 2.8: Feynman digrams for top quark FCNC decays to an up-type quark and a photon, gluon or Z boson.

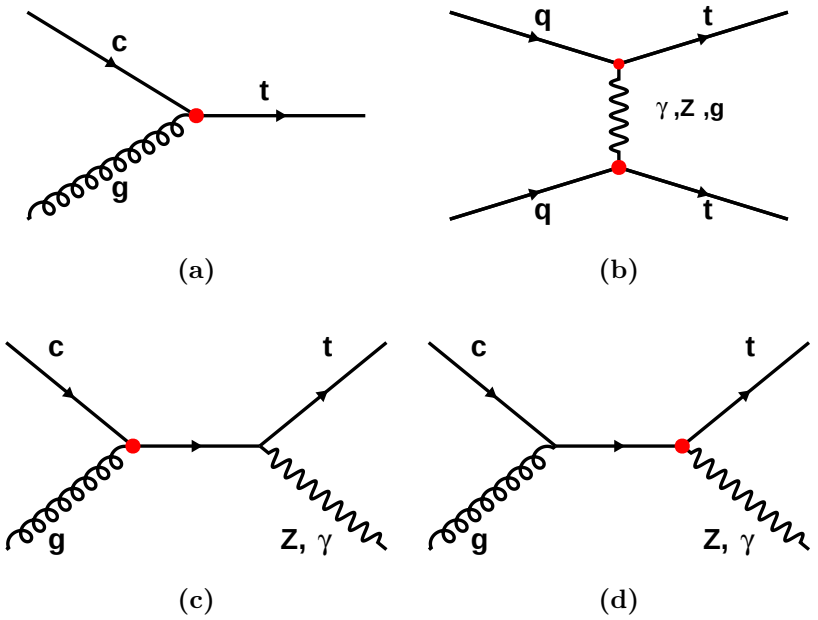

Figure 2.9: Feynman diagrams for (a) direct top production ($c\,g \to t$), (b) same-sign top production ($q\,q \to t\,t$) and associate production of a top quark and photon or Z boson ($g\,q \to t\,\gamma\,()Z\,$) via tqg (c) and $tq\gamma$-tqZ (d) anomalous interactions.

- **Single top quark production with one associated jet ($(2 \to 2)$ process):** There are four different sub-processes which lead to one top quark in the final state together with one associated jet [41]. Although this final state can be sensitive to tqZ and $tq\gamma$ anomalous coupling the tqg effects are more significant. The final state contains a top quark and a light quark or gluon, a topology similar to SM t-channel single top quark production. Related Feynman diagrams are shown in figure 2.10.

$$q\bar{q} \to t\bar{c}, \quad gg \to t\bar{c}, \quad cq(\bar{q}) \to tq(\bar{q}), \quad cg \to tg.$$

- **tZ and $t\gamma$ associated production:** All the anomalous couplings may contribute to anomalous tZ and $t\gamma$ associated production [42]. The (c) digram in figure 2.9 corresponds to the $\gamma(Z)tq$ anomalous coupling and (d) digram shows the tqg anomalous coupling. These signal channels are more sensitive to the $\gamma(Z)tq$ anomalous interactions but can be used as a cross check of other channels for tqg anomalous coupling.

- **Same-sign top quark production:** The FCNC interactions can result in

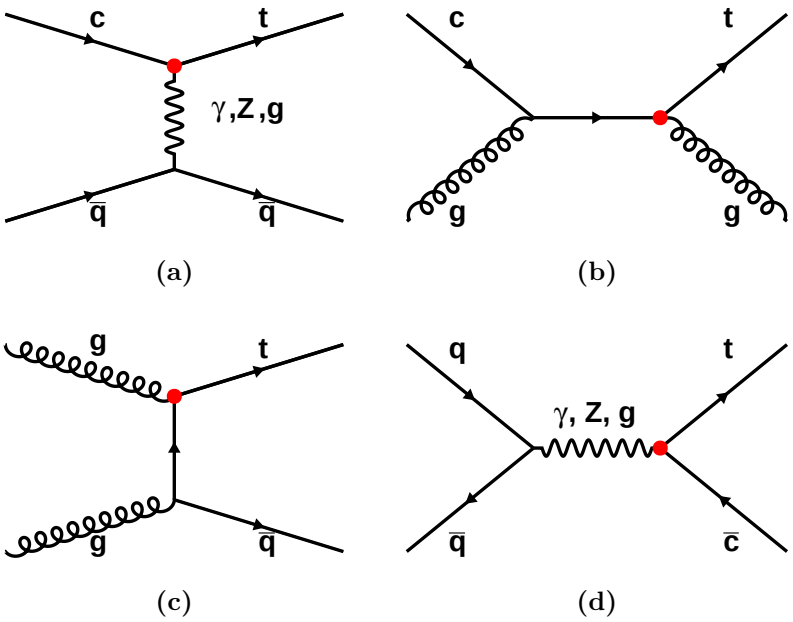

Figure 2.10: Feynman diagrams for (a) $cq(\bar{q}) \to tq(\bar{q})$ (b) $cg \to tg$ (c) $gg \to t\bar{c}$ (d) $q\bar{q} \to t\bar{c}$ anomalous single top quark production in association with a light jet.

appearance of the same-sign top quark in hadron colliders [43, 44]. Figure 2.9 (b) displays the representative diagram describing the anomalous same-sign top quark production. Same-sign top production followed by the leptonic decay of W boson from top decays give rise to final state with the same-sign leptons and b-jets. Despite the small cross section of the signal channels due to the presence of two anomalous vertices for tt production, this final state has proven to have very little SM backgrounds and is sensitive to new physics effects. Therefore, same-sign dilepton final state would provide a new window for searching for FCNC interactions [45].

In the effective Lagrangian approach, the cross section of the anomalous top production and the anomalous decay width would be a function of the anomalous coupling which should be determined from the experiments. It is nearly impossible to discriminate between the tcV and tuV anomalous interactions through the anomalous top quark decay experimentally. While different parton distribution function for the valence quarks and sea quarks provide a great opportunity to discriminate between the tcV and tuV anomalous interactions [40, 46]

2.7 Experimental results and searches for top quark FCNC interactions

Over the years, different experiments have searched for FCNC processes in the anomalous decays of top quark in $t\bar{t}$ events or anomalous productions of single top events. In this section we will review previous experimental results obtained in different experiments on the top quark FCNC interactions [8]. In the literature, there are many alternatives for normalizing the coupling constants in $\mathcal{L}_{\text{eff}}$. Therefore, limits on top-quark branching ratios are more easily comparable among different experimental results. It is worth mentioning that the limits on the anomalous couplings, are given with the notation in their corresponding publications.

2.7.1 Search for top quark FCNC processes at TEVATRON

The top quark was discovered in a $p\bar{p}$ collider TEVATRON, with a center-of-mass energy of $\sqrt{s} = 1.8$ TeV at 1995. After the top discovery, the TEVATRON experiments CDF and D0 collected more data at the center-of-mass energy of $\sqrt{s} = 1.96$ leading to precise measurement of the top quark properties and good limit on the new physics parameters involved with top quark.

CDF has performed a search for the FCNC top quark decay $t \to qZ$ and $t \to q\gamma$ using 110 pb^{-1} of data at $\sqrt{s} = 1.8$ [47]. The $t\bar{t}$ events as the dominant source of the top quark production are used in which one top decays anomalously. No excess over the SM prediction was observed and upper limits are set at 95% C.L. on the top quark FCNC decays which are

$$BR(t \to u\gamma) + BR(t \to c\gamma) < 3.2\%, \quad BR(t \to uZ) + BR(t \to cZ) < 33\% \quad (2.33)$$

The analysis was updated using 1.9 fb $^{-1}$ of data at $\sqrt{s} = 1.96$ for the $t \to qZ$ channel by CDF Collaboration and an upper limit of $BR(t \to qZ) < 3.7\%$ obtained at 95% C.L. [48]. Similar search was performed using 4.1 fb $^{-1}$ of data at $\sqrt{s} = 1.96$ by D0 Collaboration and an upper limit of $BR(t \to qZ) < 3.2\%$ obtained at 95% C.L. [49].

Among FCNC top quark decays, $t \to qg$ is very difficult to distinguish from generic multijets production via quantum chromodynamics (QCD) at a hadron col-

lider. It has therefore been suggested to search for FCNC couplings in anomalous single top-quark production. The first limits on tqg FCNC couplings to the top quark were obtained in a D0 analysis based on 0.23 fb^{-1} of the integrated luminosity [50]. The $2 \to 2$ processes were chosen (see figure 2.10) as the signal and the limits on the anomalous tcg and tug coupling are set to be 0.15 TeV^{-1} and 0.037 TeV^{-1}, respectively. The analysis was updated by D0 Collaboration using 2.3 fb^{-1} of data and limits on the anomalous tcg and tug coupling found to be 0.057 TeV^{-1} and 0.013 TeV^{-1}. The CDF Collaboration used the direct top production $2 \to 1$ for the first time to search for anomalous tqg interactions (see figure 2.9 (a)) [51]. The analysis was based on the 2.2 fb^{-1} of data and upper limits on the anomalous tcg and tug coupling are set to be 0.069 TeV^{-1} and 0.018 TeV^{-1}, respectively.

2.7.2 Search for top quark FCNC processes at HERA

In ep collision at HERA Collider at DESY, top quark can only be produced singly through the charged current (CC) reaction ($ep \to \nu t\bar{b}X$). The SM single top production cross section at HERA is less than 1 fb and is sensitive to the contribution of new physics [52]. The anomalous $tq\gamma$ and tqZ FCNC interaction would induce the neutral current interaction ($ep \to etX$) which could lead to a sizeable top quark production cross section. Due to the large mass of the Z boson single top production is dominated by the t-channel exchange of a photon. In order to produce a top quark in final state large momentum fraction of proton is needed in which the u-quark parton distribution function is dominant. Thus, this process is sensitive to $tu\gamma$ anomalous couplings.

H1 and ZEUS have both searched for the single top quark production in ep collisions at HERA [53–56]. As no clear evidence for anomalous single top production was observed upper limit on the anomalous $tu\gamma$ is set to be 0.16 and 0.12 at 95% C.L. by H1 and ZEUS experiment, respectively.

2.7.3 Search for top quark FCNC processes at LEP

In e^-e^+ collision at LEP Collider at CERN, top quark may only be singly produced through the $e^-e^+ \to e^-\bar{\nu}t\bar{b}$ process due to the large mass of top quark and its center-of-mass energy. The cross section of single top quark production is around 10^{-4} fb at LEP2 center-of-mass energy which provided a good opportunity for observation of

the FCNC interaction through the $e^-e^+ \to t\bar{c}$, s-channel process. Single top quark production through the FCNC interaction is sensitive to the tqZ and $tq\gamma$ anomalous couplings simultaneously. Therefore, the observed upper limit will exclude a region in the $BR(t \to q\gamma)$-$BR(t \to qZ)$ plane. The LEP experiments ALEPH, DELPHI, L3 and OPAL have searched for anomalous single top quark production via tqZ and $tq\gamma$ anomalous interactions [57–60]. No evidence for FCNC single top quark production is observed and upper limits are set on the anomalous couplings for different top quark mass which are summarised in table 2.4 [61].

	κ_γ			κ_Z		
Experiment	$m_t = 169$	$m_t = 174$	$m_t = 179$	$m_t = 169$	$m_t = 174$	$m_t = 179$
ALEPH	0.44	0.49	0.56	0.37	0.42	0.50
OPAL	0.39	0.48	0.60	0.34	0.41	0.52
	$m_t = 170$	$m_t = 175$	$m_t = 180$	$m_t = 170$	$m_t = 175$	$m_t = 180$
DELPHI	0.40	0.49	0.61	0.34	0.41	0.53
L3	0.43	0.43	0.49	0.38	0.37	0.43

Table 2.4: 95% CL upper limits on the anomalous $tq\gamma$ and tqZ anomalous coupling obtained at LEP experiments for different top masses.

2.7.4 Search for top quark FCNC processes at the LHC

In pp collision at the LHC Collider at CERN, all anomalous FCNC interactions can be probed and it was shown that the upper limits on the branching ratio of the rare top quark decays will be improved significantly [62, 63]. The ATLAS and CMS experiments have searched for the anomalous FCNC production or decay of top quark.

ATLAS and CMS searched for $t \to qZ$ in events produced from the decay chain $t\bar{t} \to Zq{+}Wb$ [64, 65]. In addition to the anomalous decay modes, CMS has searched for anomalous production of a single top quark in association with a Z boson which is sensitive to tqZ and tqg FCNC couplings simultaneously (see figure 2.9 (c) and (d)) [66]. The results are summarised in table 2.5.

As was discussed, the anomalous tqg interactions can induce various rare processes at hadron colliders. ATLAS collaborations have chosen the production of a single top quark without any additional particle (see figure 2.9 (a)) [69]. The CMS experiments searched for FCNC production of single top quark and a light quark or gluon (see figure 2.10) [68]. The single top quark final state without extra jets that

EXP	$\sqrt{s}$	$\mathcal{L}$	Br($t \to uZ$)%	Br($t \to cZ$)%	Ref
CMS	7 TeV	4.9 fb^{-1}	0.51	11.40	[66]
ATLAS	7 TeV	20.3 fb^{-1}	0.07		[64]
CMS	7&8 TeV	24.7 fb^{-1}	0.05		[65]
			Br($t \to u\gamma$)%	Br($t \to c\gamma$)%	
CMS	8 TeV	19.1 fb^{-1}	0.0161	0.182	[67]
			Br($t \to ug$)%	Br($t \to cg$)%	
CMS	7 TeV	4.9 fb^{-1}	0.56	7.12	[66]
CMS	7 TeV	4.9 fb^{-1}	0.035	0.34	[68]
ATLAS	8 TeV	14.2 fb^{-1}	0.0031	0.016	[69]

Table 2.5: The most stringent experimental upper bounds on the top quark FCNC branching ratios at 95% CL obtained in ATLAS and CMS from different channels.

was explored by the ATLAS Collaboration is not considered in CMS search due to its different final state topology and significantly smaller signal event yield. The results are summarised in table 2.5.

The anomalous $t\gamma$ FCNC interaction was searched for the first time at LHC in production of a single top quark in association with a photon by the CMS collaboration [67]. No excess over the SM prediction was observed and upper limits on the anomalous couplings and branching ratio were set which can be found in table 2.5. We will present that analysis in more detail in this thesis.

Chapter 3

Experimental setup

Essentially, the Ratherford α-particle scattering experiment is repeated over and over with the energy far larger than the binding energy of a system to probe the substructure of that system. Although the scientific method is the same, the energies and techniques have changed. Nowadays, accelerator machines are able to accelerate particles to extraordinary energies in the multi-TeV range.

There are two possibilities to collide a beam of accelerated particles. First, with another beam and second with a fixed target. In both cases one can study the sub-structure of the colliding particles. By using a fixed target, one can furthermore produce a beam of secondary particles. These particles may be stable, unstable, charged or neutral and the problem of accelerating unstable or neutral particles can be solved. On the other hand, the center-of-mass energy of the fixed target experiments increases with the square root of the beam energy while it increases linearly with the beam energy in beam-beam collisions. Therefore, in order to reach higher energies, it is much more efficient to use two beams in opposite directions.

Since the law of physics at sub-atomic distance scales is governed by quantum mechanics, the outcome of each collision cannot be known ahead of time and the theory can do predict the probabilities of various possible outcomes. Thus, the probability of a specific outcome of a collision connect experiments to theory and vice-versa. On the theory side, there is a well-developed formalism for predicting cross sections based on quantum field theory for a given model. On the experimental side, the performance of an accelerator is characterised by luminosity. The machine luminosity depends only on the beam parameters and can be written for a Gaussian

beam distribution as [70]

$$L = \frac{N_b^2 n_b f_{rev} \gamma_r}{4\pi\epsilon_n \beta^*} F \tag{3.1}$$

where N_b is the number of particles per bunch, n_b the number of bunches per beam, f_{rev} the revolution frequency, γ_r the relativistic gamma factor, ϵ_n the normalized transverse beam emittance, β^* the beta function at the collision point, and F the reduction factor due to the crossing angle at the interaction point (IP):

$$F = \left(1 + \left(\frac{\theta_c \sigma_z}{2\sigma^\star}\right)^2\right)^{-\frac{1}{2}} \tag{3.2}$$

θ_c is the full crossing angle at the IP, σ_z is the RMS bunch length, and $\sigma^\star$ is the transverse RMS beam size at the IP. The above expression assumes round beams, with $\sigma_z \ll \beta$, and with equal beam parameters for both beams. Finally, the expected number of events of a particular kind recorded per second can be found from multiplying the experimental measured luminosity to the theoretical calculated cross section

$$N^{events} = \sigma_{tot}\, L \tag{3.3}$$

The luminosity can be increased by reducing the transverse beam emittance, by increasing the number of particles in the beam or by increasing the revolution frequency. The integral of the delivered luminosity with respect to time is called integrated luminosity and is a measure of the collected data size. All collider experiments aim to maximize their integrated luminosities, as the higher the integrated luminosity the more data is available to analyze.

The LHC has performed since early 2010 initiating high-energy pp collisions at $\sqrt{s} = 7$ TeV and the energy was raised to a new record of 4 TeV per beam in 2012. The CMS detector was able to recording 27 fb^{-1} of high-quality pp data with efficiency in excess of 90%. The integrated luminosity delivered to CMS during stable beams in years 2010 to 2012 and for *pp* collisions is shown in figure 3.1. In addition, CMS has collected 150 μb^{-1} of lead-lead and 31 nb^{-1} of proton-lead collisions.

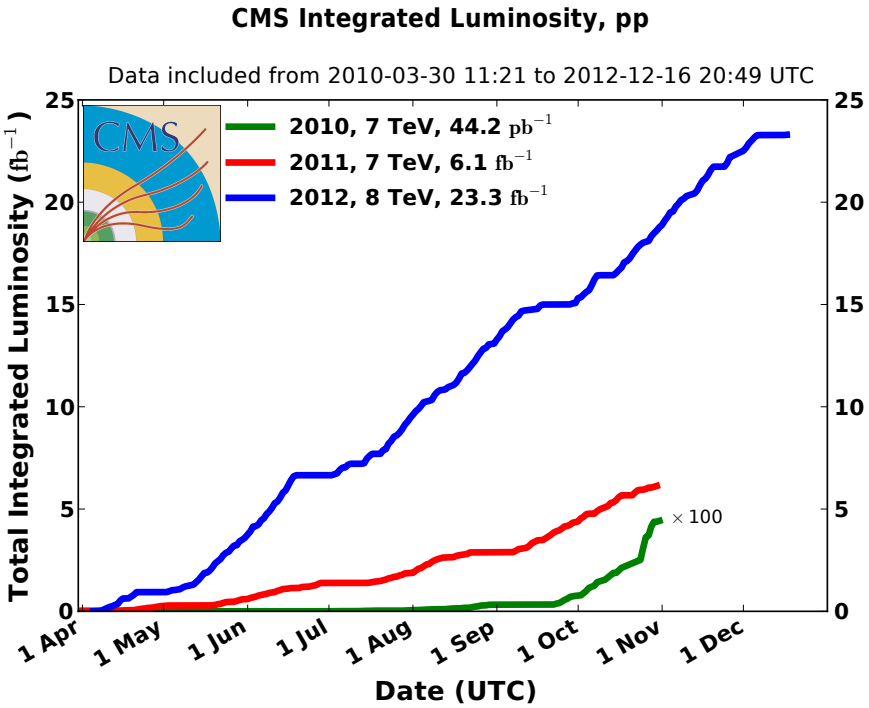

Figure 3.1: Cumulative luminosity versus day delivered to CMS during stable beams and for p-p collisions. This is shown for 2010 (green), 2011 (red) and 2012 (blue) data-taking [71].

3.1 The Large Hadron Collider

The Large Hadron Collider (LHC) is a collider located at CERN[1] near Geneva (Switzerland) [70]. It is the largest particle accelerator ever built by mankind. The LHC is a two-ring-superconducting-hadron accelerator and collider installed in the existing 26.7 km tunnel at 100 m underground that was constructed between 1984 and 1989 for the LEP machine. The LHC has been designed to collide two proton (ion) beams of 7 TeV (2.75 TeV per nucleon) each, with a design luminosity of 10^{34} cm^{-2} s^{-1} (10^{27} cm^{-2} s^{-1}). For most of the ring, the beams travel in two separate vacuum pipes, but at four points they collide in the hearts of the main experiments, known by their acronyms: ALICE, ATLAS, CMS, and LHCb. These experiments play complementary roles in the overall LHC missions and are designed for different kind of discoveries

- ATLAS: A Toroidal LHC ApparatuS [72]

  A general purpose detector which can be used to search for a rich variety of phenomena including searching for the Higgs boson and physics beyond the

[1] European Council for Nuclear Research

SM.

- CMS: Compact Muon Solenoid [73]

  CMS is the other general-purpose detector. Its mission is to study physics similar to ATLAS.

- ALICE: A Large Ion Collider Experiment [74]

  ALICE is an experiment that involves the collision of lead ions rather than protons. When heavy ions collide a new state of matter called quark-gluon-plasma will be created which can bring good information from the very early universe.

- LHCb: Large Hadron Collider beauty [75]

  The focus of the LHCb experiment is to study the phenomena which can be manifested in b-physics. B-particles (particles containing a bottom quark) are extremely massive and would likely have a rich variety of decay modes that could possibly be a window to new phenomena beyond the SM. In particular, the LHCb researchers will be looking for evidence of CP violation. in B-meson decays

  The four largest experiments are shown in the figure 3.2.

In addition to the four main detectors, two other petite detectors operate near the ATLAS and CMS detectors.

- LHCf: Large Hadron Collider forward experiment [77]

  The LHCf is the smallest detector at the LHC which stands about 460 feet in front of the ATLAS collision point. It is intended to measure the properties of forward-moving particles produced when protons crash together. The goal is to test the capability of cosmic ray measuring devices.

- TOTEM: TOTal Elastic and diffractive cross section Measurement [78]

  TOTEM is a long, thin detector connected to the LHC beam pipe, located about 650 feet away from the CMS detector. This experiment studies forward particles toward ultra high-precision measurements of the cross-sections (effective sizes) of protons.

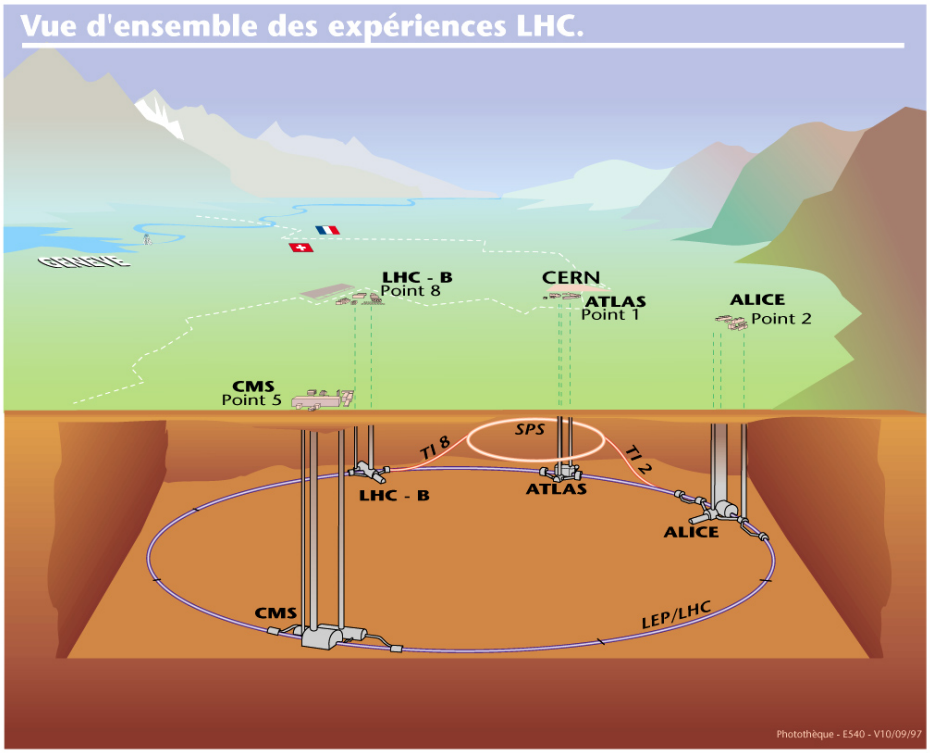

Figure 3.2: The four LHC experiments and the accelerator tunnel underground [76].

3.2 The Compact Muon Solenoid

CMS is a general purpose detector installed about 100 meters underground at the LHC interaction point 5 (P5) close to the french village of Cessy, between Lake Geneva and the Jura mountains. The CMS research program includes most of the physics from the SM measurement to search for new physics in many different phenomena.

The CMS detector is a large cylindrical solid-angle magnetic spectrometer with a superconducting solenoid which generates an internal magnetic field of 3.8 Tesla. The CMS detector, With a length of 21.5 m and a overall diameter of 15.0 m, is called compact compared to the ATLAS detector with 46.0 m long and 25.0 m in diameter. On the other hand, the CMS detector, with mass of 12500 tons is much heavier than ATLAS with mass of 7000 tons.

CMS, as is shown in figure 3.3, has cylindrical symmetry with respect to the beam axis. It is constituted by several layers of detectors centered on the interaction point to accurately reconstruct trajectories, momenta, and energies of all SM particles. The first layers are pixel detector for accurate measurement of the vertex.

Then the silicon strip tracker is located which is used for accurate track reconstruction of the charged particles. The tracker system is covered by the Electromagnetic Calorimeter (ECAL) for accurate measurement of the electron and photon energy. It also contributes to measure the electromagnetic fraction of jets energy. The last layer inside the solenoid is the Hadronic Calorimeter (HCAL) which is crucial for energy measurements of jets and missing energy. The large muon chambers are placed outside of the solenoid allow for a clean muon identification.

A sector of the CMS detector is schematically illustrated in figure 3.3. The behaviors of all basic particles including muon, electron, photon, charged and neutral hadron are shown as they passed through the detector. Different particles have different responses when they interact with different layers of CMS detector.

- A photon leaves no trace in the tracking system, and deposits all its energy in the electromagnetic calorimeter.
- An electron bends in the magnetic field and leaves trajectories in the tracking system. It deposits all its energy in the electromagnetic calorimeter.
- A muon bends in the magnetic field and leaves trajectories in the tracking system and pass through the ECAL, HCAL and the super-conducting coil. Then it penetrates to the layers of the muon chamber and bends to the opposite side due to the magnetic field outside supper-conducting solenoid and leaves trajectories in all muon chambers and leaves the detector volume.
- A charged hadron (like pion, kaon and proton) bends in the magnetic field and leaves trajectories in the tracking system. It will pass through the electromagnetic calorimeter and deposit most of its energy in the hadronic calorimeter.
- A neutral hadron (like k_L^0 or neutron) leaves no trace in the tracking system, and after passing through the electromagnetic calorimeter, deposit most of its energy in the hadronic calorimeter.

For more detailed information, please refer to the Technical Design Report of CMS [79].

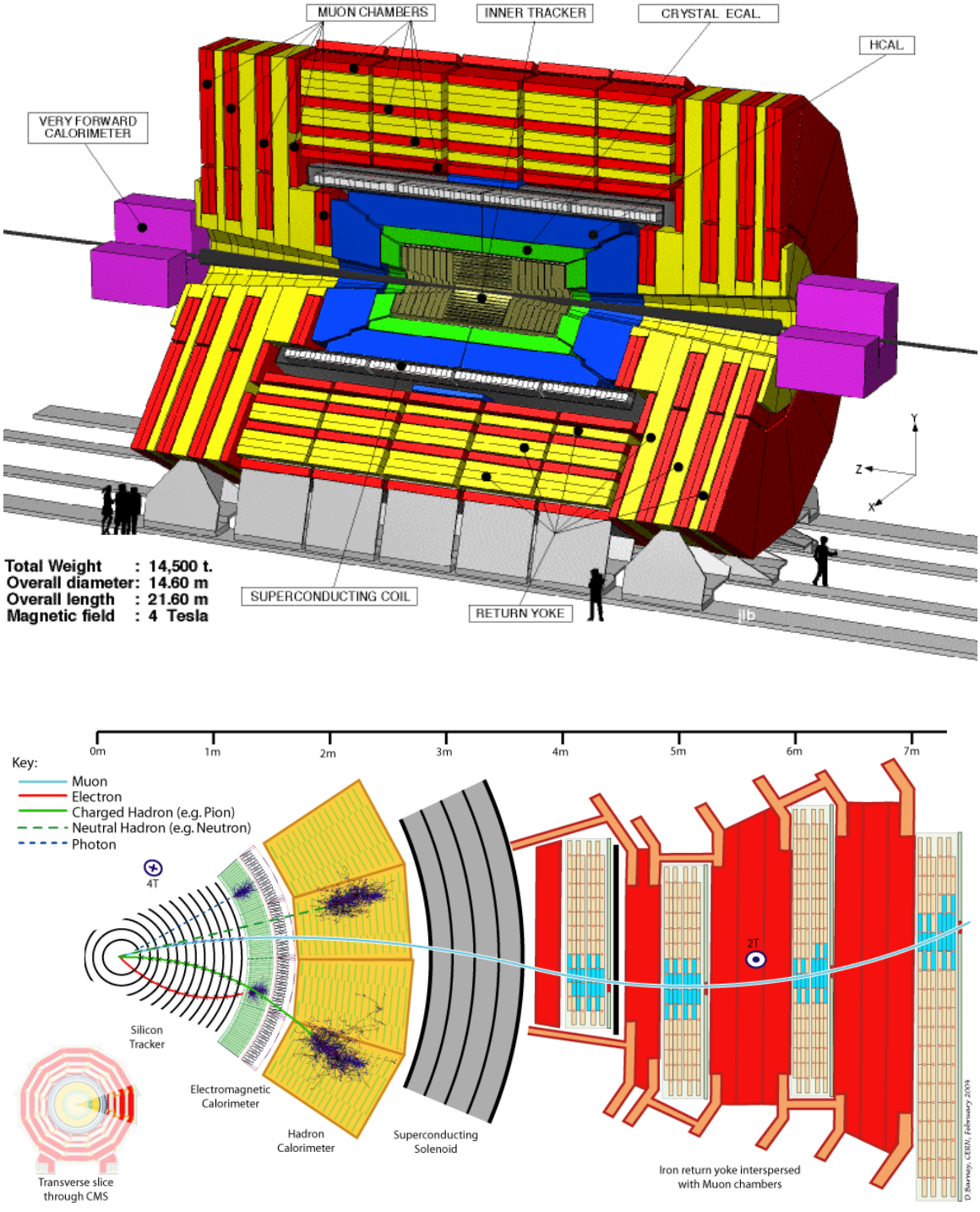

Figure 3.3: The CMS detector [73].

3.3 Coordinate conventions

The CMS coordinate system is oriented such that at the origin centered at the nominal collision point the x-axis points south to the center of the LHC ring, the y-axis points vertically upward and the z-axis is in the direction of the beam toward the Jura mountains from LHC P5. The azimuthal angle ϕ is measured from the x-axis in the $x-y$ plane and the radial coordinate in this plane is denoted by r. The polar angle θ is defined in the $r-z$ plane and is measured from the positive z-axis. The polar angle is often transformed into pseudorapidity, defined as $\eta = -\ln(\, tan(\theta/2))$. The plane transverse to the beam direction is called transverse plane ($r-\phi$ plane). The component of momentum in the transverse plane is denoted by P_T and the transverse energy is defined as $E_T = E\sin(\theta)$.

3.4 Tracker

The inner tracker system of the CMS detector is responsible for a precise measurement of the trajectories of charged particles as well as a precise reconstruction of secondary vertices produced at LHC collisions. A precise measurement of secondary vertices is necessary in many of the interesting physics channels, especially those related to b-jets and τ physics.

The CMS inner tracker system surrounds the interaction point with a radius of 115 cm, over a length of 270 cm on each side of the interaction point. At the LHC design luminosity of $10^{34} cm^{-2} s^{-1}$, there will be more than 20 overlapping proton-proton interactions and around 750 particles with each bunch crossing, which produce few thousand hits in the tracker. In order to perform a precise track reconstruction in such a dense environment, a tracker system with high granularity and high hit resolution is required. In addition, the time between each bunch crossing would be 25 ns which requires a fast response tracker system which does not allow the use of gas detectors due to its slow response. The intense particle flux will cause severe radiation damage to the tracking system and was the main challenge in the design of the tracking system. These requirements on granularity, speed and radiation hardness are satisfied by using the silicon detectors.

The CMS silicon tracker consists of two tracking devices, the inner pixel and the outer strip detectors. It consists of a central part (barrel) with three pixel layers

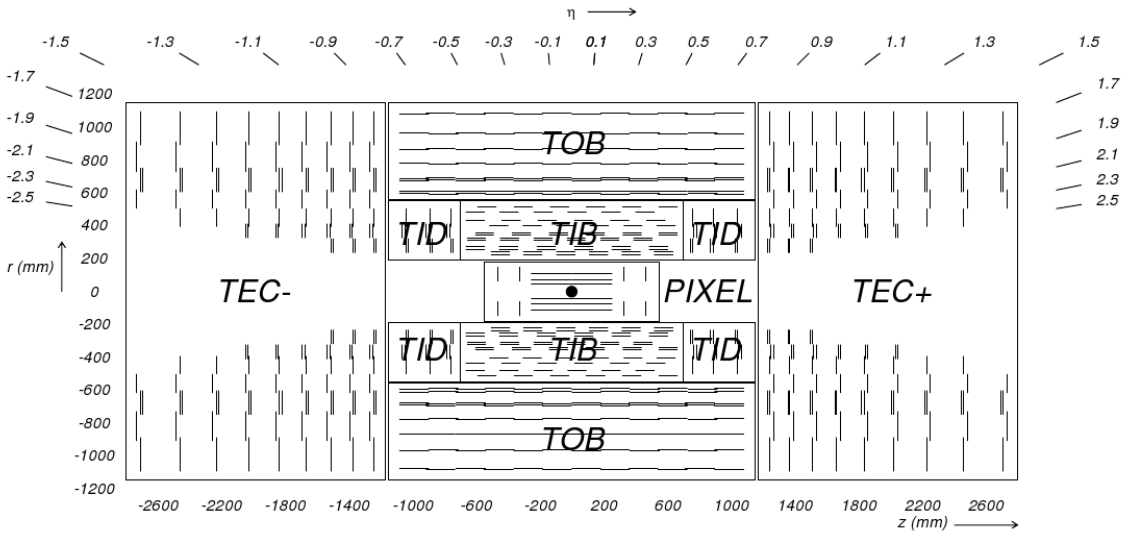

Figure 3.4: Schematic cross section through the CMS tracker. The components are: Pixel Detector (PIXEL), Tracker Inner barrel (TIB), Tracker Outer barrel (TOB), Tracker Inner Disk (TID), Tracker endcap (TEC). Each line represents a detector module. Double lines indicate back-to-back modules which deliver stereo hits [73].

at radii between 4.4 cm and 10.2 cm and ten strip layers extending outwards to a radius of 1.1 m. Each system is completed by endcap sections with two pixel cover radii 6 cm to 15 cm and tree plus nine strip layers extending the acceptance of the tracker up to a pseudo-rapidity of $|\eta| < 2.5$. A schematic drawing of the CMS tracker is shown in figure 3.4. The pixel detector is the inner-most part of the CMS Tracker. The silicon detector composed of three different subsystems. The Tracker Inner Barrel and Disks (TIB/TID) which are composed of 4 barrel layers and 3 disks at each endcap, Tracker Outer Barrel (TOB) which consists of 6 barrel layers and Tracker EndCaps (TEC+ and TEC- where the sign indicates the location along the z axis) which are composed of 9 disks.

The high resolution pixel detector is closest to the interaction region. It contributes to an unambiguous hit recognition and precise vertex reconstruction. It is also responsible for a small impact parameter resolution to distinguish secondary vertices arise from the decay of short lived particles after having traveled only a few hundred micrometers from the original collision point. In addition to the reconstruction of secondary vertices, the pixel detector is used to form seed tracks for the outer track reconstruction and high level triggering.

Pixel detector composed of pixel devices which provide a fine granularity in

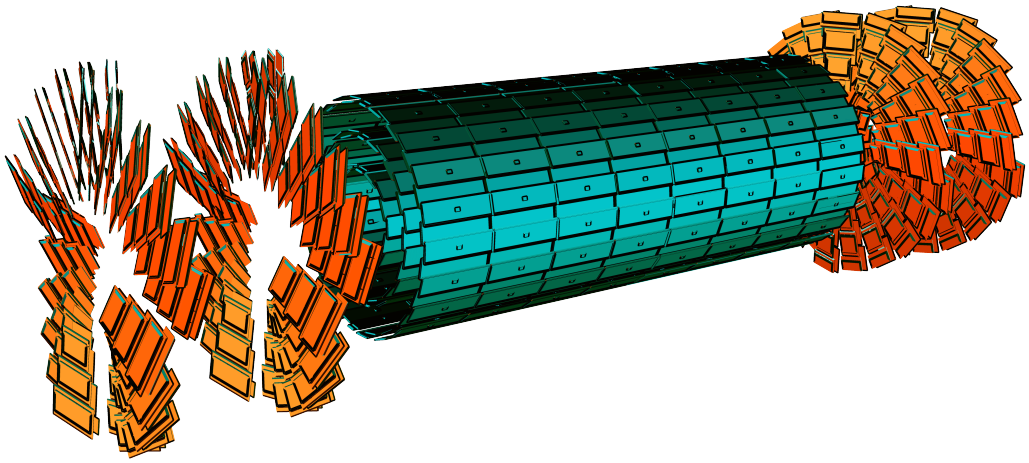

Figure 3.5: Layout of the current CMS pixel detector [80].

three-dimensional space information for vertexing. It consists of three barrel layers (BPix) at mean radii of 4.4, 7.3 and 10.2 cm and two endcap disks (FPix) placed at $\approx$ 6 to 15 cm in radius and $z = \pm 34.5$ and $z = \pm 46.5$ cm extending the total acceptance up to $|\eta| < 2.5$. BPix (FPix) contain 48 million (18 million) pixels covering a total area of 0.78 (0.28) m^2. A layout of the current CMS pixel detector is shown in figure 3.5.

When a charged particle passes through the silicon detector, gives enough energy for electrons to be ejected from the silicon atoms, creating thousands or tens of thousands of electron-hole pairs. Each pixel uses an electric current to collect these charges on the surface as a small electric signal. A particle's trajectory can be deduced by knowing which pixels have been touched. Since the detector is made of two dimensional tiles, rather than strips, and has a number of layers, we can create a three-dimensional picture. Silicon pixels size (100×150 μm^2 in $r - \phi$ and z) allows to reach the desired resolution on impact parameter.

The Silicon Strip Tracker (SST) of the CMS experiment covers an area of 198 m^2 with more than 9.3 million strips and 15000 silicon modules. It is composed of TIB / TID / TOB / TEC+ / TEC- parts. TIB/TID uses 320 μm thick silicon micro-strip sensors parallel to the beam axis in the barrel and radial on the disks. TIB and TID deliver up to 4 $(r - \phi)$ measurements on a trajectory which leads to single point resolution of 23 μm and 35 μm strip bitches. TOB uses 500 μm thick micro-strip sensors and provides another 6 $(r - \phi)$ measurements with single point

resolution of 53 μm and 35 μm for different strip bitches. TEC is composed of 9 disks, provide up to 9 $(z - \phi)$ measurements per trajectory.

The silicon detectors work in much the same way as the pixels: as a charged particle crosses the material it knocks electron from atoms and within the applied electric field these move giving a very small pulse of current lasting a few nanoseconds. This small amount of charge is then amplified, giving us hits when a particle passes, allowing us to reconstruct its path.

The CMS tracker has been operated successfully during Run 1 of the LHC ended in February 2013. As was mentioned in previous sections the LHC has delivered about 6.1 fb^{-1} integrated luminosity of data at 7 TeV and about 23.3 fb^{-1} at 8 TeV and CMS has recorded overall 93% of these data. During this time, less than 3% of the detector became inactive and less than 5% of the delivered luminosity was lost due to the tracker. By the time of the shutdown in 2013, about 2.3% (7.2%) of the barrel (endcap) modules of the pixel detector and 2.5% of the strip detector were inactive. The hit reconstruction efficiencies exceed 99% and 99.5% in the strip and pixel detector, respectively (with the exception of the innermost layer of the pixels) [81].

3.5 Electromagnetic calorimeter

The Electromagnetic Calorimeter (ECAL) is responsible for identifying, measuring the energies, and the location of electrons and photons precisely. One of the driving criteria in the CMS ECAL design was the requirement on energy resolution, in order to be sensitive to the decay of a Higgs boson into two photons. This capability is enhanced by the good energy resolution provided by a homogeneous crystal calorimeter. Crystal calorimeters have the potential to provide fast response, radiation tolerance and excellent performance for energy resolution.

The CMS ECAL is a hermetic homogeneous calorimeter made of lead tungstate ($PbWO_4$) crystals which have high density (8.28 g/cm^3) and a short radiation length (0.89 cm) allowing for a fine granularity and a very compact calorimeter system. The scintillation decay time of these crystals is of the same order of magnitude as the LHC bunch crossing time and about 80% of the light is emitted in 25 ns. The light output is relatively low and depends on the temperature. It is about 4.5

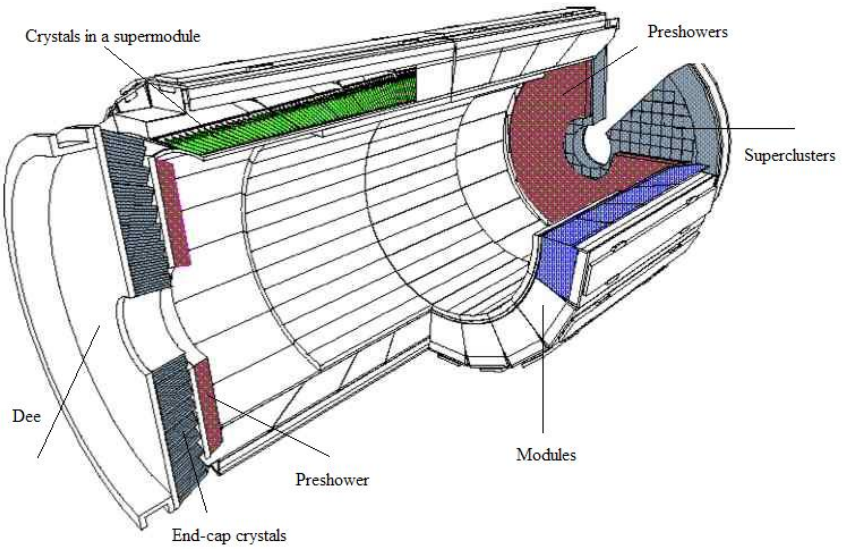

Figure 3.6: Schematic of CMS electromagnetic calorimeter, showing the arrangement of crystal modules, supermodules and endcaps, with the preshower in front.

photoelectrons per MeV at 18°C.

The ECAL is split into two subsystems: the ECAL barrel (EB) with 61200 crystals and ECAL endcap (EE) with 7324 crystals to surround the collision point of the interacting protons. The EB crystals have a tapered shape and cover the pseudo-rapidity range $|\eta| < 1.479$. The crystal cross-section corresponds to 0.0174×0.0174 in $\eta - \phi$ or $22 \times 22\, mm^2$ ($26 \times 26\, mm^2$) at the front (rare) face of crystal. The total crystal length is 230 mm which is correspond to 25.8 X_0. The EE are placed 315.4 cm far from the interaction point in each side and cover the pseudo-rapidity range $1.479 < |\eta| < 3$. The EE crystals are grouped in mechanical units of 5×5 crystals. Each endcap is divided into 2 halves, or Dees which each holds 3662 crystals. The crystals have a front (rare) face cross section $28.62 \times 28.62\, mm^2$ ($30 \times 30\, mm^2$) and a length of 220 mm which is correspond to 24.7 X_0.

A preshower detector is placed in front of the endcap to provide $\pi^0 - \gamma$ separation. As was mentioned detecting the photons from the Higgs decay is one of the ECAL's main jobs. Neutral pions decay to two photons immediately after they are produced in collisions. These two low energy photon can inadvertently mimic high-energy photons when they are close together that the ECAL picks up together. A preshower detector sits in front of the ECAL within a fiducial region $1.653 < |\eta| < 2.6$ to identify neutral pions. The preshower has a much finer granularity than the ECAL

which can see each of the pion-produced particles as a separate photon, and can also help the identification of electrons against minimum ionizing particles, and improves the position determination of electrons and photons.

The CMS preshower consists of two lead radiators, about 2 and 1 radiation lengths thick respectively, each followed by a layer of silicon micro strip detectors to measure the deposited energy and the transverse shower profiles. The two layers of detectors have their strips orthogonal to each other to measure the vertical and horizontal position of particles. Figure 3.7 shows the arrangement of crystal modules, supermodules and endcaps, with the preshower in front in a schematic picture.

In general the ECAL energy resolution can be parametrized according to the following form:

$$\left(\frac{\sigma}{E}\right)^2 = \left(\frac{S}{\sqrt{E}}\right)^2 + \left(\frac{N}{E}\right)^2 + C^2 \tag{3.4}$$

where S is the stochastic term , N is the noise term, and C is the constant term. The energy resolution of the CMS ECAL for electrons in beam tests with energies ranging between 20 and 250 GeV has been measured to be [82],

$$\left(\frac{\sigma}{E}\right)^2 = \left(\frac{2.8\%}{\sqrt{E}}\right)^2 + \left(\frac{0.12\,GeV}{E}\right)^2 + (0.3\%)^2 \tag{3.5}$$

where E is measured in GeV. The resolution has been measured in data and simulation using 2010 and 2011 LHC data. The resolution for $E_T \approx 45$ GeV electrons from Z boson decays is better than 2% in the EB , and is between 2% and 5% elsewhere. The resulting energy resolution for photons with $E_T \approx 60$ GeV from 125 GeV Higgs boson decays varies across the EB from 1.1% to 2.6% and from 2.2% to 5% in the EE [83].

3.6 Hadronic calorimeter

The primary purpose of the Hadronic CALorimeter (HCAL) is to measure the hadron jets energy. In addition, the HCAL is also able to perform a precise time measurement for each energy deposit. Precise time measurements can be used for excluding calorimeter noise and energy deposits from beam halo and cosmic ray muons. Time information can also be valuable for identifying some new physics signals such as long-lived particle decays and slow high-mass charged particles [84].

The HCAL is a sampling calorimeter meaning that it finds the position, energy and arrival time of the incident particles using alternating layers of 'absorber' and fluorescent 'scintillator' materials. It has thin layers of scintillators interleaved between brass absorber plates. To maximize the absorber thickness in the small available space (about 1 m radially) inside the solenoid, the brass plates are relatively thick (5.5 cm) and the scintillator is relatively thin (3.8 mm). This structure of the detector produces a rapid light pulse. The light pulses are shifted in the visible region via wavelength shifting fiber and feed into readout boxes to be amplified by photodetectors. When the amount of light in a given region is summed up over many layers of tiles in depth, called a 'tower', this total amount of light is a measure of a particles energy.

The HCAL sits behind the tracker and the electromagnetic calorimeter as seen from the interaction point. Figure 3.7 shows the longitudinal view of the CMS detector. The CMS HCAL consists of four regions. The barrel (HB), endcap (HE), forward (HF) and outer (HO) calorimeters. The resolution of the calorimeter system, combining the ECAL and the HCAL, for a charged pion is a function of energy $\sigma/E \approx 100\%/\sqrt{E(\mathrm{GeV})} \oplus 5\%$ [73].

The HB is a sampling calorimeter located in the central detector $|\eta| < 1.3$. The plastic scintillator is divided into 16 η sectors, resulting in a segmentation $(\Delta\eta, \Delta\phi) = (0.087, 0.087)$. The absorber consists of a 40 mm thick front steel plate, followed by fourteen brass plates with 50.5 and 56.5 mm thick, and a 75 mm thick steel back plate. The total absorber thickness at $|\eta| = 0$ is 5.82 interaction lengths (λ_I). The HB effective thickness increases with polar angle, resulting in 10.6 λ_I at $|\eta| = 1.3$. The electromagnetic crystal calorimeter in front of HB adds about 1.1 λ_I of material. The energy resolution for a pion in HB is $\sigma/E \approx 90\%/\sqrt{E(\mathrm{GeV})}$.

The HE cover a substantial portion of the rapidity range, $1.3 < |\eta| < 3$. It consists of 19 layers of scintillator tiles sandwiched between 70 mm brass absorbers. The total length of the calorimeter, including electromagnetic crystals, is about 10 interaction lengths (λ_I). The energy resolution for a pion in HE is $\sigma/E \approx 100\%/\sqrt{E(\mathrm{GeV})}$.

In the central region, HB is not thick enough to contain hadronic shower fully, particularly those fluctuated showers which develop deep inside the HCAL. The effect of shower leakage has a direct consequence on the measurement of missing

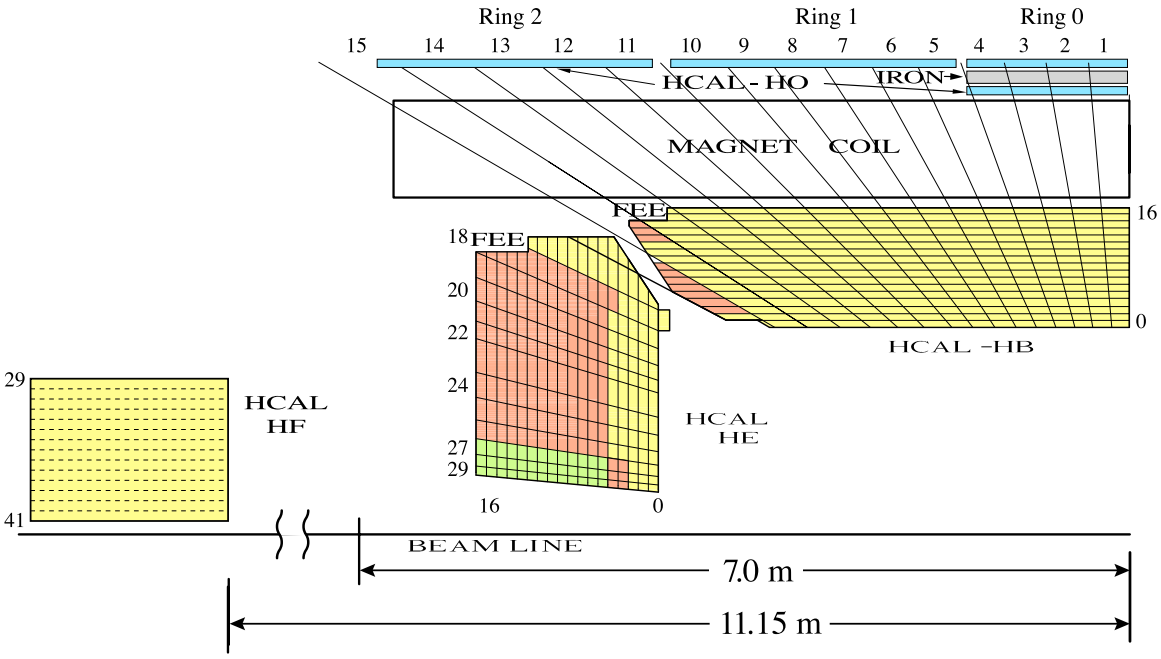

Figure 3.7: Longitudinal view of the CMS detector showing the locations of the hadron barrel (HB), endcap (HE), outer (HO) and forward (HF) calorimeters [85].

transverse energy. Need to extend HCAL outside the solenoid magnet and make additional sampling of the shower. This part outside the magnet coil is referred as Outer Hadron Calorimeter (HO). Therefore, the HO is useful to decrease the leakage and improve the resolution of the missing transverse energy measurement. The HO covers the central rapidity region ($|\eta| < 1.26$). The HO is constrained by the geometry of the muon system and occupied by the five Muon Rings (numbered as $-2, -1, 0, 1, 2$). For ring 0, there will be two HO layers (Layer 0 and 1) on either side of the 18 cm thick tail catcher iron at R=3.82 m and 4.07 m. For Rings -2,-1,1 and 2, there will be a single HO layer (Layer 1) at R= 4.07 m. The HO utilises the solenoid coil as an additional absorber equal to $1.4/\sin\theta$ interaction lengths and is used to identify late starting showers and to measure the shower energy deposited after HB. The energy resolution for a pion in HO is $\sigma/E \approx 120\%/\sqrt{E(\mathrm{GeV})}$ [73].

The very forward calorimeter, HF, is located in the forward region outside of the magnetic field volume, covers a large pseudo-rapidity range $3 < |\eta| < 5$. The HF significantly improves jet detection and the missing transverse energy resolution which are essential in single top quark production studies, Standard Model Higgs, and all SUSY particle searches [86]. The HF experiences the highest particle fluxes. Around 760 GeV per proton-proton interaction is deposited into the two forward

calorimeters on average, compared to only 100 GeV for the rest of the detector. This high fluxes of particles presents a unique challenge to calorimetry and its design. Quartz fibers were chosen to satisfy the requirement of surviving in this harsh conditions providing about 10 λ_I. Iron absorbers, embedded quartz fibers, parallel to the beam make a fast (10 ns) detector to collect the Cherenkov radiation.

3.7 Solenoid

One of the most important features of the CMS apparatus is the presence of a high solenoidal magnetic field. It is the largest superconducting magnet ever built. The superconducting magnet for CMS has been designed to reach a uniform magnetic induction of 3.8 T in a long superconducting solenoid of 12.5 m length and 6 m diameter with a stored energy of 2.6 GJ at full current.

The configuration and parameters of the magnetic field lead to the measurement of muon momenta with good resolution, without making stringent demands on the spatial resolution of muon chambers. A magnetic field of 3.8 T brings substantial benefits not only for the muon tracking and inner tracking but also for electromagnetic calorimetry by preparing higher momentum resolution obtained in tracker.

The geometry of CMS magnet is shown in figure 3.8 (a and b). The inner coil accommodates the inner tracker and the full calorimetry. Within the tracker region, the field has a high strength and is relatively homogeneous. The magnetic flux is returned via a 1.5 m thick nearly saturated iron yoke instrumented with four stations of muon chambers. Therefore, the CMS magnet is the backbone of the CMS experiment as all sub-detectors are supported from it. In figure (3.8, c), map of the B field and field lines predicted for a longitudinal section of the CMS detector is shown.

The coil contains four-layer superconducting thin solenoid built in five modules. It is indirectly cooled by saturated helium at 4.5° K temperature. In the core, a 3.8 T magnetic field is provided. The thick saturated iron yoke returns the magnetic flux generated by coils and provide a 2 T reversed magnetic fields to measure muon momentum. The yoke is composed of 11 elements, five three-layered barrel wheels , and three endcap disks in each side. The innermost yoke layer in the barrel region is 295 mm thick and each of the two outermost ones are thicker with 630 mm thick.

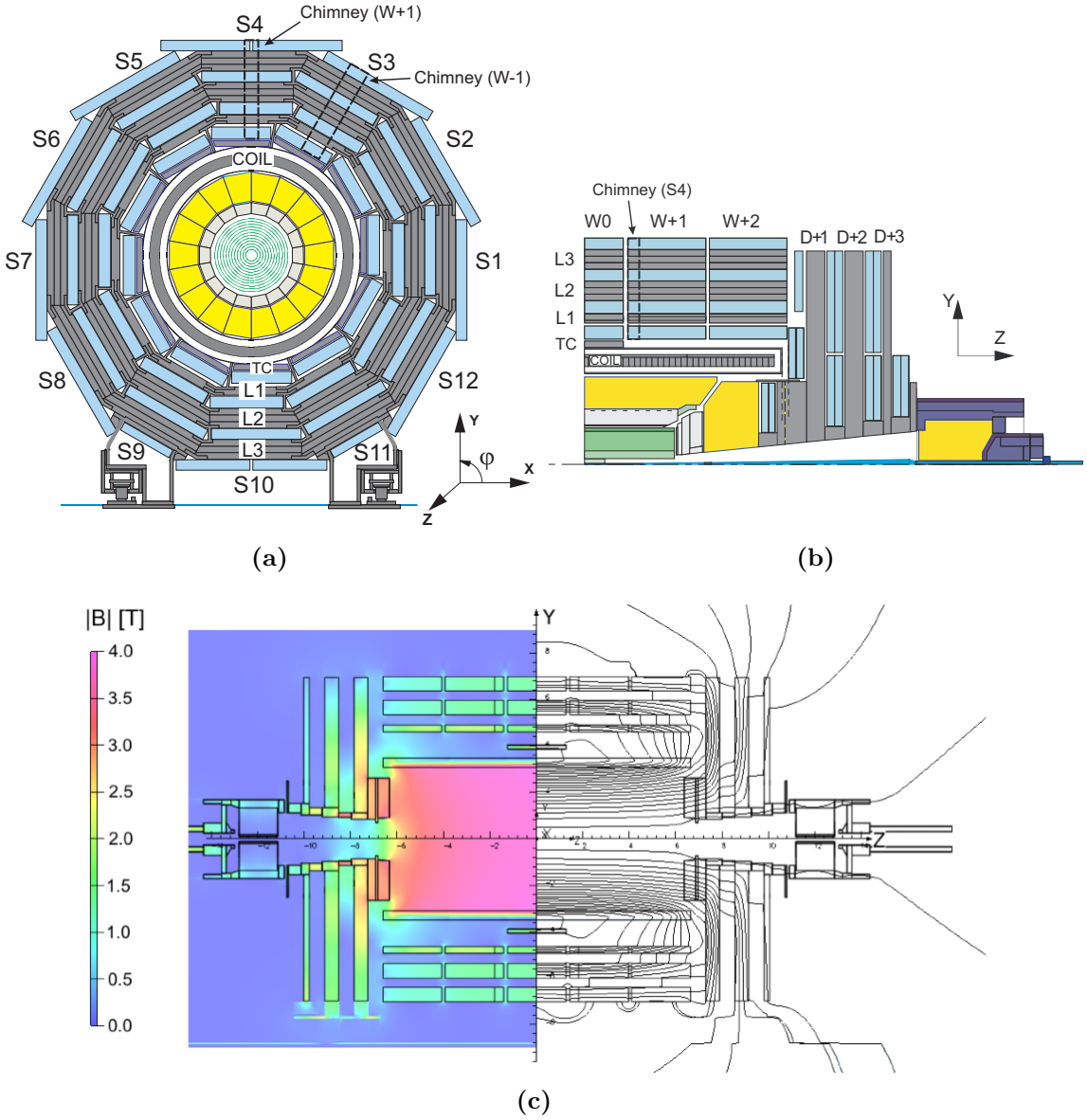

Figure 3.8: Top: Schematic views of the CMS detector, with the numbering convention for azimuthal sectors (S), wheels (W), barrel yoke layers (L) and end-cap disks (D) [87]. Bottom: Map of the B field and field lines predicted for a longitudinal section of the CMS detector by a magnetic field model at a central magnetic flux density of 3.8 T [88].

The barrel rings are approximately 2.5 m long. The central barrel ring, centred on the interaction point, supports the superconducting coil. The main role of the yokes is to increase the field homogeneity in the tracker volume and to reduce the stray field by returning the magnetic flux of the solenoid. In addition, the steel plates play the role of absorber for the four interleaved layers (stations) of muon chambers that will be explained in the next section.

3.8 Muon system

As is implied by the experiment's name, 'Compact Muon Solenoid', detecting muons is one of the CMS most important tasks. Muon detection provides a clean signal to detect over the very high background rate at the LHC. For example, the Higgs decay to four muons through the $H \rightarrow ZZ^{\star} \rightarrow \mu^{+}\mu^{-}\mu^{+}\mu^{-}$ decay chain, called 'gold plated channel', provides the best 4-particle mass resolution and has led to the discovery of the Higgs boson recently. In addition, many new physics scenarios need a clean muon detection to be observed at the LHC.

The CMS muon system is designed to identify and reconstruct muons over the entire kinematic range of the LHC. Muons can penetrate several meters of iron without interacting, unlike most particles, they pass through all layers of the detector. Therefore, the muon system is placed at the very edge of the experiment to detect muons. In order to cover the solenoid magnet, the muon system was designed to have a cylindrical barrel section and 2 planar endcap regions.

The CMS muon system uses three different gas-ionization particle detector to detect and measure the muons; Drift Tubes (DT), Cathode Strip Chambers (CSC), and Resistive Plate Chambers (RPC). These different type of detectors have been chosen to work in different places of the CMS detector with different background rates and magnetic field. For all the muon system detectors, the basic physical modules are called 'chambers' which are independently-operating units assembled into the overall CMS muon detector system. All the muon chambers are aligned in a way to be roughly perpendicular to the muon trajectories and placed to provide hermetic coverage over the $|\eta|$ range from 0 to 2.4. Chambers are placed at several different values of the radial r distance (z distance) from the interaction point in barrel (endcaps) to detect the track in several points in order to measure the bending

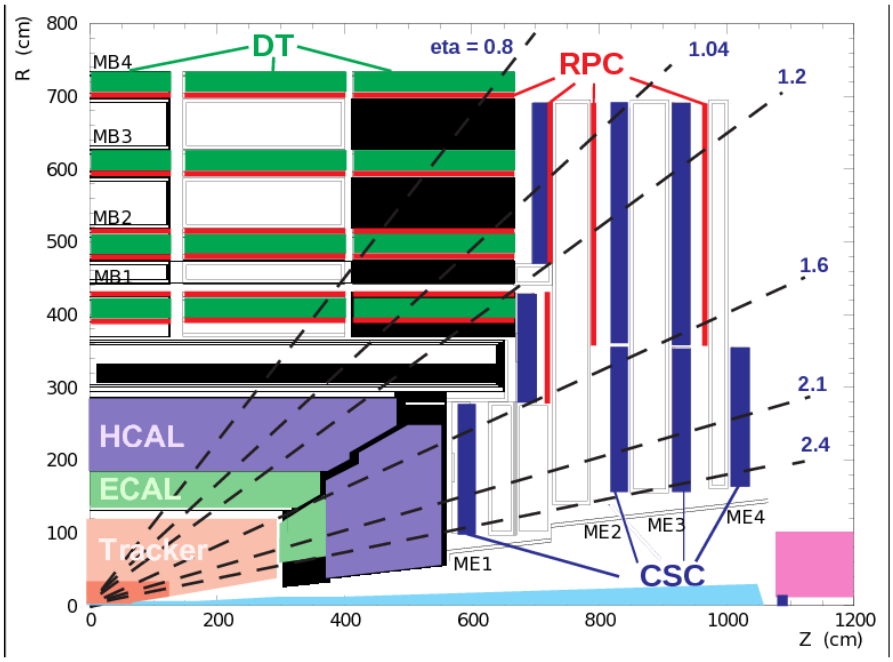

Figure 3.9: Schematic showing the muon systems showing the locations of the drift tubes (DT), cathode strip chambers (CSC) and resistive plate chambers (RPC) [85].

radius of the muon. An assembly of chambers which are placed at a fix value of r (for barrel chambers) or z (for endcap chambers) are called 'station'. It is shown in figure 3.9 that the barrel and endcaps consist of 4 stations labeled MB1-MB4 and ME1-ME4, respectively.

The DT system measures muon positions in the barrel part of the detector. Each 4-cm-wide tube contains a stretched wire within a gas volume. When a muon or any charged particle passes through the volume it knocks electrons off the atoms of the gas. These follow the electric field ending up at the positively-charged wire. A DT chamber is made of 3 (or 2) superlayers in which the wires in the 2 outer superlayers are parallel to the beam line and the wires in the inner superlayers are orthogonal to the beam line. These perpendicular wires provide a track measurement in the magnetic bending plane ($r - \phi$) and the z position along the beam.

The muon barrel system is consists of five wheels placed inside the magnet return yokes of CMS which cover the pseudo-rapidity region $|\eta| < 1.2$. Each wheel is divided in 12 sectors, each sector with a 30° azimuthal angle, covering the full azimuthal dimension around the beam. In the barrel region, the magnetic field between the yoke segments is mostly uniform with strength below 0.4 T. One DC

detectors are used in each station, except in the uppermost (lowermost) sector (see figure 3.8), named sector 4 (sector 10), where the station MB4 is physically made of two DT chambers.

In the endcap region where the magnetic field is more intense and the background (signal) rate is higher than in the barrel, CSC are used. CSCs are multiwire proportional chambers consists of 6 anode wire planes interleaved to 7 cathode panels perpendicularly and the strips are milled on them. Because the strips and the wires are perpendicular, we get two position coordinates for each passing particle. The CSC detectors with fast response time, radiation resistance and fine segmentation (1 mm measurement of position in $(r - \phi)$ plane) identify muons in $0.9 < |\eta| < 2.4$ range.

DTs and CSCs in the barrel and endcaps provide excellent position and time resolution. In order to assign the muon to the right bunch crossing when the LHC reaches full luminosity a complementary, dedicated trigger system consisting of resistive plate chambers (RPC) was added in both the barrel and endcap regions. The RPC system provides excellent timing with somewhat poorer spatial resolution over a large portion of the rapidity range of the muon system ($|\eta| < 2.1$). In addition to serving as dedicated triggers, the RPC system plays role in the muon reconstruction procedure. A higher trigger efficiency and greater rate capability will be obtained by processing the signals coming from the DT, CSC, and the RPCs in parallel.

The CMS RPC consists of two gaps with common read-out strips in between. Six layers of RPC chambers are embedded in the barrel iron yokes. The two innermost DT layers are sandwiched between RPC layers and the third and fourth DT layers are complemented with a single RPC layer as is shown in figure 3.9. In the endcap region, there is a plane of RPCs in each of the first 3 stations.

3.9 Trigger

The LHC will operate at 14 TeV center-of-mass energy and a high luminosity ($10^{34} cm^{-2} s^{-1}$), at which about 22 inelastic interactions are expected to occur per bunch crossing. About one billion proton-proton interactions will take place every second inside the detector which is impossible to store and process this large amount of data. Since experiments are typically searching for 'interesting' events (such as

decays of rare particles) that occur at a relatively low rate, trigger systems are used to identify the events that should be recorded for later analysis. Therefore, the CMS trigger system has the formidable task of reducing the input data rate to a rate of O(100) Hz which will be written to permanent storage. The CMS trigger system is based on two steps called Level 1 (L1) Trigger and High-Level Trigger (HLT).

The CMS L1 trigger, is a hardware-based system, uses coarse local data from the calorimeter and muon systems to make electron/photon, jet and energy sum, and muon triggers. The L1 trigger has three components called local, regional and global. The local triggers component, also called Trigger Primitive Generators (TPG) is based on the information coming from the local calorimeter trigger and local muon trigger. The local calorimeter trigger looks for energy deposit in ECAL crystals or HCAL towers and the muon trigger search for signals from DT, CSC and RPC system. The regional calorimeter trigger uses all available information to form the e/γ candidates, calculate the transverse energy sums per calorimeter region and also prepare the isolation information for the e/γ and muon candidates. The calorimeter and muon candidates are ranked according to their transverse energy and momentum and the four first candidates are passed to the Global Muon Trigger (GMT) and Global Calorimeter Trigger (GCT). The GCT determines jets, number of jets, the scalar transverse energy sum of all jets above a programmable threshold, the total transverse energy and the missing transverse energy. The global muon trigger determines more information about the selected muon using the complementarity and redundancy of the three muon systems. Finally, data from the GCT and GMT are transmitted to GT where the L1 accept decision is made. An architecture picture of the L1 trigger is depicted in figure 3.10. The Level 1 trigger provides a reduction in the event rate to about 100 kHz.

The HLT trigger is a software-based system, to further reduce the event rate to about 100 Hz on average. The HLT uses full granularity detector data for performing the reconstruction and filtering algorithms on a large computing clusters. Only data accepted by the HLT are recorded for offline physics analysis. The starting selection of the HLT is based on the L1 candidates, and then improves the reconstruction and filtering process by using also the tracker information. The tracking is very important at the HLT level due to its role at the reconstruction. For example, improving the momentum resolution of the muon can reduce the muon trigger rate; by

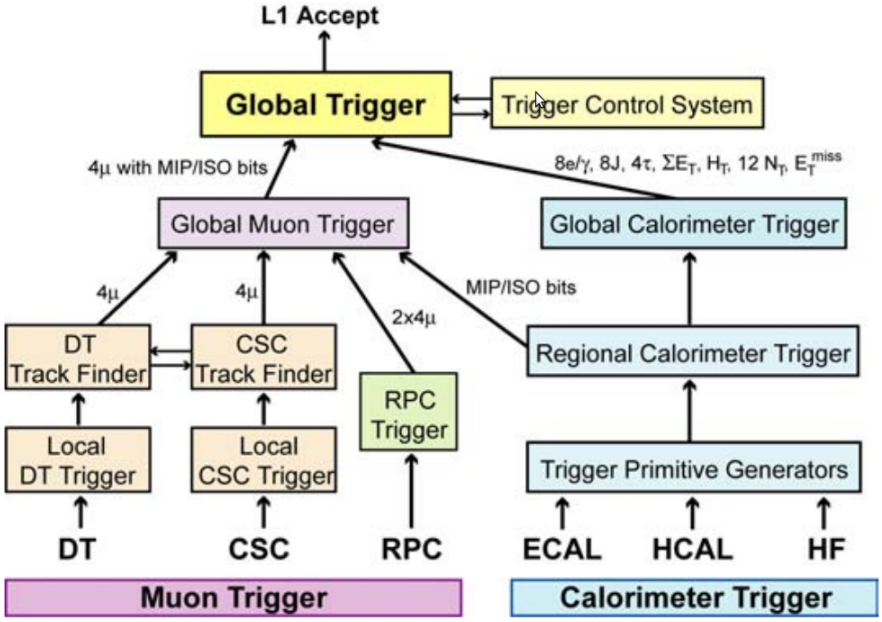

Figure 3.10: Architecture of the Level-1 Trigger [73].

assigning a track to the calorimeter cluster, better electron identification is obtained; by finding the transverse impact parameter coming from the secondary vertex, it is possible to trigger on jets produced by b-quarks; it prepares good information for tagging the tau lepton decays hadronically.

Chapter 4

Event Reconstruction

In this chapter, we will review the procedure in which particles are produced in proton-proton collisions and are identified with the CMS detector.

4.1 Collider physics

In quantum field theory, one calculates the cross section of processes as one or two incoming fundamental particles interacting to form a final state. This could be easily used to find the expected number of events when the incoming particles are fundamental and without internal sub-structure like e^-e^+ collisions. When the incoming fundamental particles are confined in a composite particle, like quarks and gluons inside the proton, the hard collision of interest only occurs when partons with the right quantum numbers happen to have the right center-of-mass energy to make the desired final state. Thus, a precise knowledge of the probability $f_i(x, Q^2)$ that

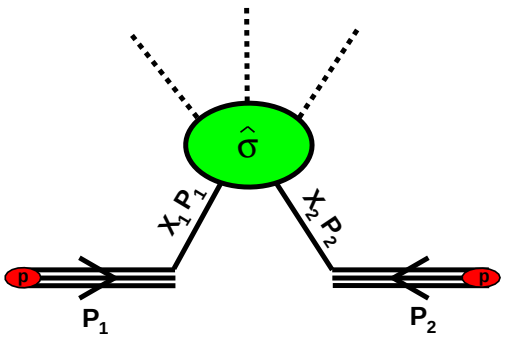

Figure 4.1: figure shows how the partons of hadrons contribute to an interaction for some hard process in hadron-hadron collisions.

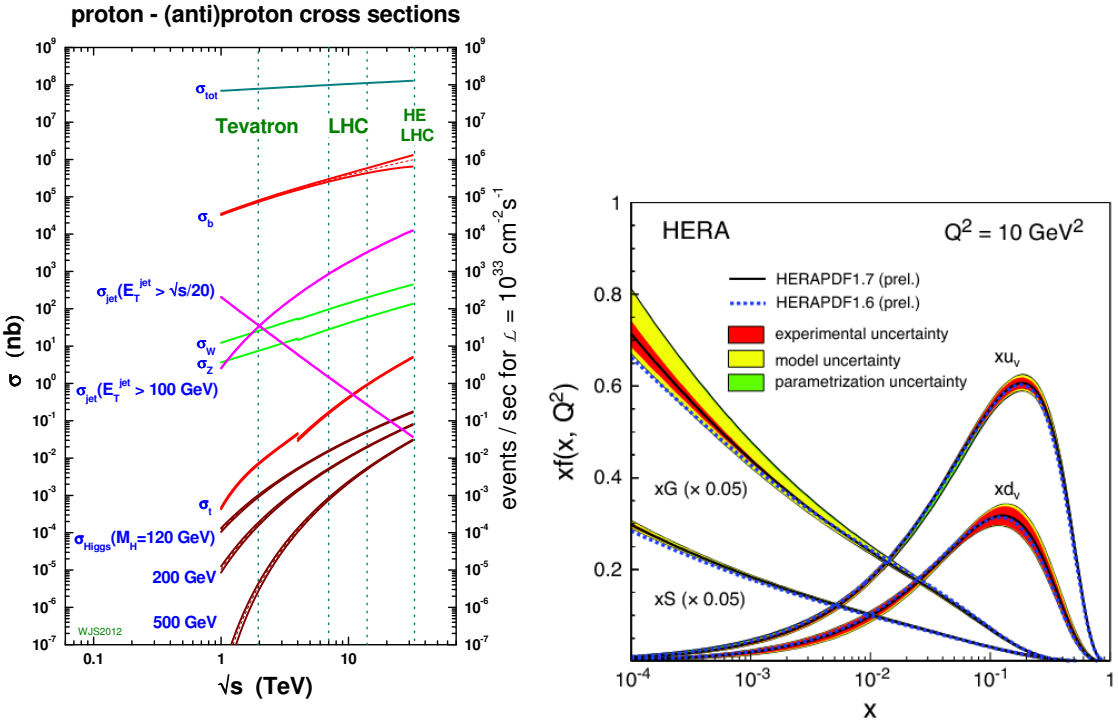

Figure 4.2: Right the parton distribution functions from HERAPDF at $Q^2 = 10$ GeV^2. The gluon and sea quarks distributions are scaled down by a factor of 20. The experimental, model and parametrisation uncertainties are shown separately [89]. Left plot shows scattering cross sections versus c.m. energy for the SM processes in pp collisioins. [90].

a parton carries a fraction x of the proton momentum for a given energy scale is essential in order to make predictions for the SM and beyond the SM processes at hadron colliders.

The $f_i(x, Q^2)$ is called Parton Distribution Function (PDF) which cannot be extracted from the theory and are determined from experimental observables in various processes. In figure 4.2 right, the parton distribution functions obtained from a fit to the data recorded by HERA is shown. The shape of the sea quarks and gluon distributions changes quickly at very low x values and is dominated by gluon distributions. At large x values, the valence quarks are the dominant distributions.

Cross sections (σ) are calculated by convoluting the parton level cross section $\hat{\sigma}$ with the PDFs. Total cross section can be written as

$$\sigma = \int dx_1 f(x_1, \mu_F) \int dx_2 f(x_2, \mu_F) \hat{\sigma}(x_1 p_1, x_2 p_2, \mu_F, \mu_r), \quad \hat{s} = x_1 x_2 s \tag{4.1}$$

where $\hat{\sigma}$ depends on the renormalization (μ_r) and factorization scale (μ_F). It can

be calculated perturbatively in QCD for hard scattering with energy scale much larger than $\Lambda^2_{QCD} \approx (200\text{MeV})^2$. For an arbitrary hard process the effects of the EW and QCD next-to-leading (NLO) corrections can vary the parton level cross section. Therefore, the calculation of the higher order effects is very important to estimate the contribution of different processes more accurately and to make sure that the cross-sections are under control for precision measurements.

In figure 4.1 left, the cross sections for various typical SM hard processes versus center-of-mass energy are shown for a p-p hadron collider in units of mb. The total p-p cross section (top curve) increases with the c.m. energy as a power of $ln\,(s)$ due to the larger parton densities at higher energies. All SM processes have similar behavior versus energy. The inclusive jet cross section decreases due to the cut on the transverse momentum of the jets.

4.2 Event Generation

In order to study a signal from SM processes or extract a signal of new physics from the SM backgrounds, one needs to generate and simulate the signal events similar to what is expected in real data. At high energy colliders like LHC, different issues make this procedure challenging. In each hard interactions hundreds of SM or BSM particles can be produced with momenta range over many orders of magnitude. The calculation of matrix element is too laborious at higher orders of perturbation theory. At low energies, all soft hadronic phenomena (like hadronization and the underlying event) must rely upon QCD inspired models and cannot be computed from first principles. Many divergences and near divergences issues should be addressed after calculation of matrix element. Finally, the matrix elements must be integrated over a final-state phase space with huge dimensions in order to obtain predictions of experimental observables [91].

A wide range of the interesting processes at the LHC can be simulated using Monte Carlo techniques. Different MC generators are employed to accurately simulate what happens in an interaction from the hard short-distance phenomena to the long wavelengths of hadronization and hadron decays. MC generators split events into different stages and simulate each step independently. In this picture, the steps are ordered descending in invariant momentum transfer. A hard interaction, is fol-

lowed by multiple initial and final state Bremsstrahlung emissions and, eventually, by the hadronization process.

There is a very broad spectrum of event generators from general purpose ones to matrix element generators. The general purpose MC event generators such as HERWIG [92], Pythia [93] and Sherpa [94] provide a comprehensive list of LO matrix elements of the SM and some BSM processes. In addition to the LO matrix elements, multi purpose MC generators contain theory and models for a number of physics aspects, such as hard and soft interactions, parton distributions, initial and final state parton showers, multiple interactions, fragmentation and decay. In order to compute the hard process matrix element at higher order and cope with arbitrary final state, matrix element generators have therefore been constructed. Parton level events generated by the matrix element generators are processed by general purpose event generators to do the remained steps. The most widely used matrix element generators in CMS are ALPGEN [95], POWHEG [96] and MADGRAPH [97].

4.2.1 Renormalization and factorization scales

As can be seen in equation 4.1, the cross section for hadronic collisions can be expressed as the convolution of hard processes (short distance, calculable in perturbation theory) and soft processes (long distance, e.g. PDFs). The factorization scale separates the short-distance physics of the hard-scattering cross section from the long-distance hadronic physic [98].

The hard and soft processes have expansions in powers of strong coupling constant (α_s) while the coefficients of this expansion are known to a certain order of α_s. Therefore, the series should be truncated at a defined order while uncalculated higher order terms are remained in the perturbation series. Due to missing higher order corrections in the calculations, there are theoretical uncertainties on the cross sections. They are traditionally estimated by varying the scale $\mu = \mu_F = \mu_r$ between $Q/2$ and $2Q$ where Q is set to the natural scale, the typical mass of the process.

It is worth noting that the inherent uncertainty derives from the cross section dependency on the unphysical renormalization and factorization scales is often large in a lowest order calculations. This dependency reduces by calculating the cross section at higher orders.

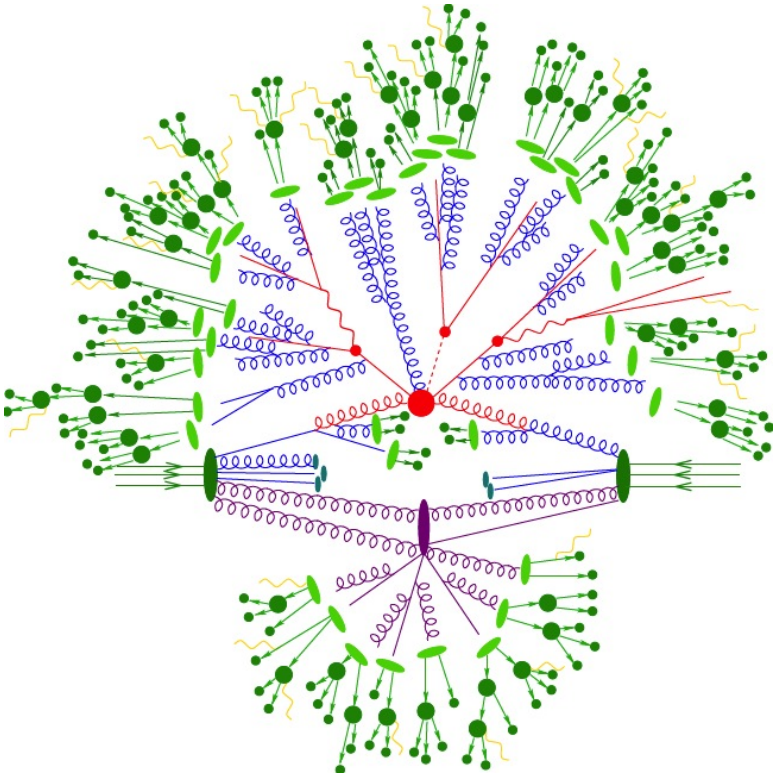

Figure 4.3: P-p collision simulation. Matrix element generators simulate 'hard' part of scattering (shown in red). Parton showers produce Bremsstrahlung (blue). Multiple interaction models simulate 'secondary' interactions (purple). Fragmentation models 'hadronize' QCD partons (green). Hadron decay packages simulate unstable hadron decay (dark green). Generators produce QED Bremsstrahlung (yellow). Figure shows how the partons of hadrons contribute to an interaction for some hard process in hadron-hadron collisions.

4.2.2 Parton showers

The momenta of the outgoing partons in a hard process can be calculated using matrix elements at leading, or in a few cases at next-to-leading in α_s order. The effect of higher orders can also be simulated through a parton shower algorithm. It is typically formulated as a chain of momentum transfer from the high scales to the low scales in which the partons are confined into hadrons ($\approx$ 1 GeV).

The high momenta coloured partons emit QCD radiation in the form of gluon as photons are radiated from the accelerated charged particles. Unlike the uncharged photons, the gluons carry colour charges and can split into gluons and cause further radiation, leading to parton showers. The cross section of a parton i splitting to j and k partons, for example $q \rightarrow q + g$ has two infra-red divergences, soft and collinear. The soft divergence occurs when the radiated gluon energy tends to zero and the collinear divergence occurs when the j and k partons are collinear. There-

fore, enhanced higher order terms are associated with emitting a soft or collinear gluon for which the relevant QCD matrix elements are large.

The formulation of the parton branching is formalized in terms of the Sudakov form factor which is given by [99]

$$\Delta_i(q_1^2, q_2^2) = exp\left\{ -\int_{q_2^2}^{q_1^2} \frac{dq^2}{q^2} \frac{\alpha_s}{2\pi} \int_{\frac{Q_0^2}{q^2}}^{1-\frac{Q_0^2}{q^2}} dz \int_0^{2\pi} d\phi P_{ji}(z,\phi) \right\} \tag{4.2}$$

where Q_0 is the scale at which the shower is terminated, α_s is the strong coupling constant, z is the energy fraction of i carried by j and P_{ji} is the splitting function in which several types of splitting are included. The Sudakov form factor is the probability of evolving from q_1^2 to q_2^2 without branching.

The MC production of the parton showering follows the following structure. Starting from the scale q_1^2, the q_2^2 is found using the ratio of Sudakov factors at these two scales in a way that no further splitting occurs in between.

4.2.3 Parton distribution functions

The cross section defined by equation 4.1 will be influenced by the choice of PDF set. On the other hand, the event shape can be varied for different PDF sets considering the PDF role in parton showers and multiple parton interactions. As was discussed, the $f(x_i, \mu_F)$ can not be extracted from the first QCD principle. Nevertheless the perturbative QCD can predict the scale dependent evolution of the PDFs through the DGLAP equations.

Over the years, different ansatz are made and developed by different groups using relative data, e.g. from Deeply Inelastic Scattering (DIS).

4.2.4 Hadronization

Due to asymptomatic freedom of QCD, coloured quarks and gluons can be regarded as free particles during a hard interactions. After the particle shower has terminated, we enter the low-momentum-transfer and long distance in which color confinement will organize the partons into colorless hadrons. This is called hadronization or fragmentation. Fragmentation is governed by non-pertabutive QCD that can not be calculated from scratch.

Different models are developed and parametrised to describe the transition between partonic final state and hadronic final state, including the Lund string model and cluster model [100]. The color-connected pairs of partons produces a jet of hadrons.

4.3 Tracks and vertices

The CMS tracker was designed to reach good space resolution during the high luminosity LHC run. In such a dense environment, efficient track-finding algorithms are also needed to deliver the desired performance.

At the the first step of the reconstruction process, the signals above specified thresholds in pixel and strip channels are clusters into the hits. Then the position of the hits are determined using specefic algorithm. The average hit efficiency which is the probability to find a cluster in a given sensor that has been traversed by a charged particle is more than 99% and 99.8% for pixel and silicon detector, respectively [101]. At the second step, the hits are used to reconstruct the tracks of the charged particles. The Combinatorial Track Finder (CTF) algorithm is used to produce a collection of reconstructed tracks. CTF produces the collection of reconstructed tracks using iterative algorithm. First, the easiest tracks to find (e.g large P_T track) are searched for and the related hits are removed from the hit collections. Then the search is repeated for more difficult and challenging tracks while the number of hits are reduced.

Each iteration proceeds in 4 steps:

- A seed is generated using few hits to provide initial track candidates.
- The seed trajectories along the expected flight path of a charged particle is extrapolated to find additional hits that can be assigned to the track candidate.
- The parameters of the tracks are obtained by the best fit.
- The tracks are selected by applying some criteria.

The magnetic field causes helical paths of charged particles and therefore five parameters are needed to define a trajectory. The parameters can be extracted using three 3-dimensional points or two 3-dimensional points in addition to the assumption

of the origin of the track near to the interaction point. The high granularity of the pixel detector reduces the fraction of channels that are hit compared to the outer strip layer. For example, around 0.002-0.02% of channels in the pixel detector and 0.1-0.8% in the strip detector were occupied during the data taking with a 'zero-bias' trigger, with about nine p-p interactions per bunch crossing. In addition, pixel detector produces 3-dimensional spatial measurements, which is essential for the estimation of the trajectory parameters. Therefore, track finding begins with trajectory seeds created in the inner region of the tracker. This also leads to the reconstruction of low-momentum tracks that are deflected before reaching the outer part of the tracker by the strong magnetic field.

In seed generation procedure the position of the center of the reconstructed beam spot and the locations of primary vertices in the event (including those from pileup events) is needed. A very fast track and vertex reconstruction algorithm is performed on the hits from the pixel detector to provide the initial information for the seed generation. The tracks and primary vertices found at this level are known as pixel tracks and pixel vertices, respectively.

A series of six iterations of the track reconstruction algorithm is applied for the full track reconstruction at the CMS. Iteration 0 is designed for prompt tracks near the interaction point with $P_T > 0.8$ GeV and three pixel hits. The seeds at this iteration step are produced from three pixel hits (pixel triplets). Therefore, high quality seeds and well-measured starting trajectories is provided by the three precise 3-dimensional space points. Iteration 1 is used to recover prompt tracks that have only two pixel hits. The seeds are produced using two hits and a third space-point given by the location of a pixel vertex which is usually more than one because of pile up (Mixed pairs with vertex). Iteration 2 is responsible for finding low-P_T prompt tracks. The seeds are produced from a combination of pixel and matched strip hits (Pixel triplets). Iterations 3-5 are intended to find tracks that are produced outside of the pixel detector volume or tracks that do not leave hits in the pixel detector. Iteration 3 and 4 use the two inner TIB layers and rings 12 of the TID/TEC and iteration 5 use two inner TOB layers and ring 5 of the TEC for seeds. Table 4.1 shows the seeding requirements and the minimum P_T and the maximum transverse (d_0) and longitudinal (z_0) impact parameters relative to the center of the beam spot for each of the six tracking iterations .

Table 4.1: The configuration of the track seeding for each of the six iterative tracking steps. Shown are the layers used to seed the tracks, as well as the requirements on the minimum pt and the maximum transverse (d_0) and longitudinal (z_0) impact parameters relative to the centre of the beam spot. The Gaussian standard deviation corresponding to the length of the beam spot along the z-direction is σ [101].

Iteration	Seeding layers	pt (GeV)	d_0 (cm)	z_0
0	Pixel triplets	>0.8	<0.2	$<3\sigma$
1	Mixed pairs with vertex	>0.6	<0.2	$<0.2cm^*$
2	Pixel triplets	>0.075	<0.2	$<3.3\sigma$
3	Mixed triplets	>0.35	<1.2	<10cm
4	TIB 1+2 & TID/TEC ring 1+2	>0.5	<2.0	<10cm
5	TOB 1+2 & TEC ring 5	>0.6	<5.0	<30cm

After the track finding procedure, tracks are selected in a way to reduce the tracks which are not associated with a charged particle (fake track). Tracks with an acceptable fit (using χ^2/number of degree of freedom (ndf)) which are originated from a primary interaction vertex (using tracks impact parameters which are the distance from the centre of the beam spot in the plane transverse to the beam-line and the distance along the beam-line from the closest pixel vertex) are selected.

The z coordinates at the point of closest approach to the beam line is used to cluster selected tracks. The clustering algorithm must balance between resolving all vertices including pileup and not splitting a single vertex. Track clustering is performed using a deterministic annealing (DA) algorithm [102] in which a global minimum is found for a problem with many degrees of freedom. In this method the z-coordinates of the points of closest approach of the tracks to the center of the beam spot and their associated uncertainties are used to build a function that its minimum leads to the most probable vertex positions.

The tracking algorithm provides a good track reconstruction for charged particle with $P_T > 0.1$ GeV over the full pseudo-rapidity range of the tracker $|\eta| < 2.5$. The average track-reconstruction efficiency for charged particle with $P_T > 0.9$ GeV is 94% (85%) in barrel (endcap) using $t\bar{t}$ simulated events under typical 2011 LHC pileup conditions . The achieved vertex position resolution for vertices with many tracks is 10-12 μm in each of the three spatial dimensions.

4.4 Particle Flow

The CMS experiment uses the particle-flow event reconstruction technique for reconstructing and identifying all stable particles in the event (i.e., electrons, photons, muons, charged hadrons and neutral hadrons). In this technique the direction, energy and type of particles are determine through a combination of all CMS sub-detectors informations [103]. Then the list of the particles are used for building the jets, determining the missing transverse energy, reconstructing the decay products and etc.

As was discussed in section 4.3, the iterative-tracking strategy was adopted in tracker to achieve both high efficiency and low fake rate. Tracker is the cornerstone of the particle-flow event reconstruction considering good momentum resolution and precise measurement of the charged-particle direction at the production vertex. On the other hand, stable neutral particles such as photons and neutral hadrons are not reconstructed by the tracker. The information from the calorimeters are used to find the energy and direction of the neutral particles. A specific clustering algorithm is developed for the particle-flow event reconstruction and is performed separately in each sub-detector (ECAL barrel and endcap, HCAL barrel and endcap, PS first and second layer) except HF.

The particle flow elements, tracks and colorimeter clusters, are connected to each other by a link algorithm. In this algorithm, the last hit of the track is extrapolated to the PS layers, ECAL and HCAL and is linked to any given cluster if the extrapolated position is within the cluster boundaries. Similarly, a link between two calorimeter clusters, or between an ECAL and a PS cluster can be connected. Some 'blocks' containing two or three elements as the base of particle reconstruction and identification are produced. When a block is classified as a certain type of particle, it is removed from the unclassified blocks list.

The particle-flow algorithm is able to reconstruct more than 90% of the jet energy fractions which are carried by charged particles, photons and neutral hadrons with good precision. In figure 4.4, the particle flow reconstructed jet is compared to jet made from the sole calorimeter information (calo jet). The difference between the transverse momentum of the reconstructed jet and generated jet is scaled to the generated jet Pt to find the resolution of the jet reconstruction procedure. The particle flow jets has the efficiency near to 100% independent of the P_T while the

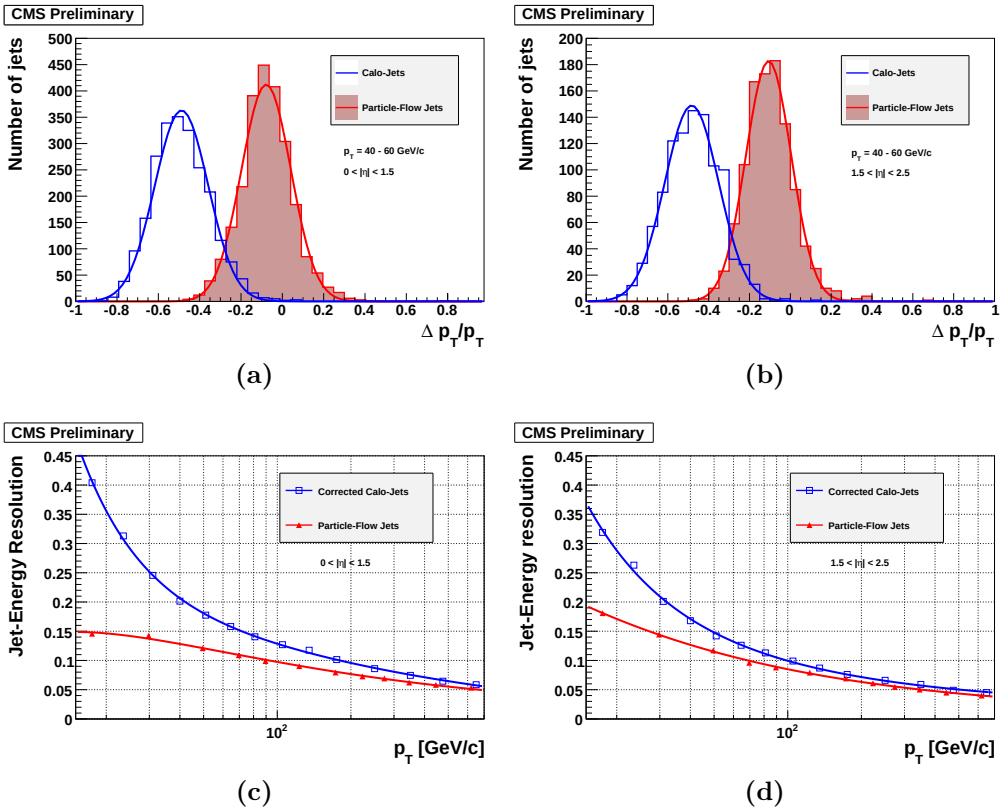

Figure 4.4: Distributions of (P_T^{rec} - P_T^{gen})/P_T^{gen} for P_T between 40 and 60 GeV/c, as obtained from calo-jets (open histogram) and from particle-flow jets (solid histogram) pointing to the barrel (a) and to the end-caps (b). A Gaussian is fit to all distributions, to determine the response and the resolution. Jet-energy resolutions as a function of P_T for corrected calo-jets (open squares) and for particle-flow jets (upwards triangles) in the barrel (c) and in the end-caps(d) [103].

calo jets have low efficiency at low P_T. The jet energy resolution is also shown in figure 4.4.

4.5 Photon

Photons are reconstructed based on the clusters from the crystals within the ECAL. Collections of clusters built from reconstructed hits or RecHits form superclusters and these superclusters are sorted into photons and electrons. Due to the different geometric layouts of the EB and EE, different clustering algorithms must be defined. A hybrid algorithm is performed to form superclusters in both barrel and endcaps.

In Hybrid algorithm a fixed bar of 3 or 5 crystals in η are fixed while searching dynamically for energy in ϕ direction. A crystal which contains a signal corresponding to a E_T greater than those of all its immediate neighbors and above a predefined threshold (1 GeV) is chosen as a seed crystal. In the barrel, where crystals are in a grid of $\eta \times \phi$, the clusters have a fixed width in the η direction. A 5×1 (in $\eta \times \phi$) group of crystals centred on the seed crystal is the first domino of the cluster. In the direction, adjacent strips of five crystals are added if their summed energy is above another predefined threshold (0.1 GeV). An example of the result of the Hybrid algorithm is depicted in figure 4.5. In the endcaps, where crystals are arranged in an $x \times y$ grid, fixed matrices of 5×5 crystals are used [104].

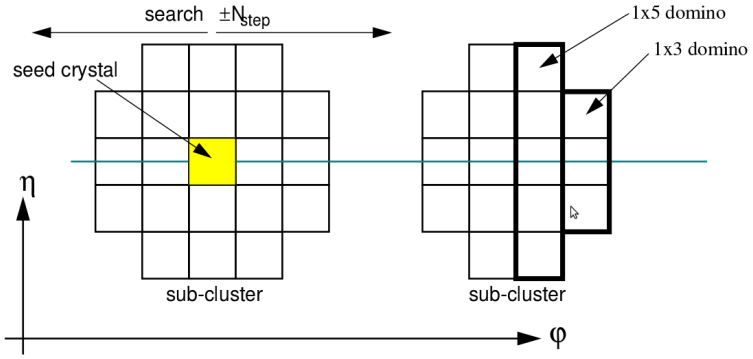

Figure 4.5: Domino construction step of Hybrid algorithm [105].

Photon identification is based on the shower-shape and isolation variables. In the following some of the most commonly used variables are itemized:

- The weighted cluster RMS along η inside 5×5 region of supercluster ($\sigma_{i\eta i\eta} = \sqrt{\sum_i^{5\times5} \omega_i(\eta_i - \bar{\eta}_{5\times5})^2 / \sum_i^{5\times5} \omega_i}$ where the index i runs over the 5×5 surround-

ing the seed crystal of the supercluster, η_i is the pseudo-rapidity of the i^{th} crystal, $\bar{\eta}_{5\times5}$ is the energy weighted mean of the 5×5 crystals pseudo-rapidity and $\omega_i = 4.7 + ln(E_i/E_{5\times5})$).

- the ratio of HCAL tower energy just behind the electromagnetic seed cluster in a cone of radius $\Delta R = 0.15$ over the energy of electromagnetic supercluster (H/E).

- the scalar sum of energy of the hadronic particle flow candidates reconstructed in a cone of $\Delta R < 0.3$ around the photon candidate (PF charged hadron isolation). This variable quantifies the amount of hadronic activity in the vicinity of a photon candidate. The PF charged hadron isolation is able to distinguish photon candidates originating from jet misidentification because they are more likely to be reconstructed close to charged hadronic particles than isolated prompt photons are.

- the sum of energy of neutral hadrons in a cone of $\Delta R < 0.3$ (PF neutral hadron isolation).

- the sum of energy of photons in a cone of $\Delta R < 0.3$ (PF photon isolation).

PF photon isolations should be corrected due to pile-up energy contribution as:

$$PFIso^{\rho-corrected} = max(PFIso - \rho_{event} \times A_{eff}, 0) \tag{4.3}$$

where the energy density ρ_{event}, computed using FastJet package [106], is the median background density per unit area and a measure of the pile-up activity in the event [107]. The effective area A_{eff} is the area of the isolation region weighted by a factor that takes into account the dependence of the pileup transverse energy density on η. When the extra contribution due to pileup is subtracted from the photon, charged and neutral hadron sums, their dependence on the number of vertices is removed as shown in the plots of figure 4.6

More than half of photons traversing the CMS tracker convert into electron-positron pairs before the last three layers of the tracker due to the large amount of tracker material in front of the ECAL. PF reconstruction algorithm uses the fully reconstructed conversions in which the tracks of electron pairs are associated with energy deposits in the ECAL. This approach avoids misidentifying electron-positron

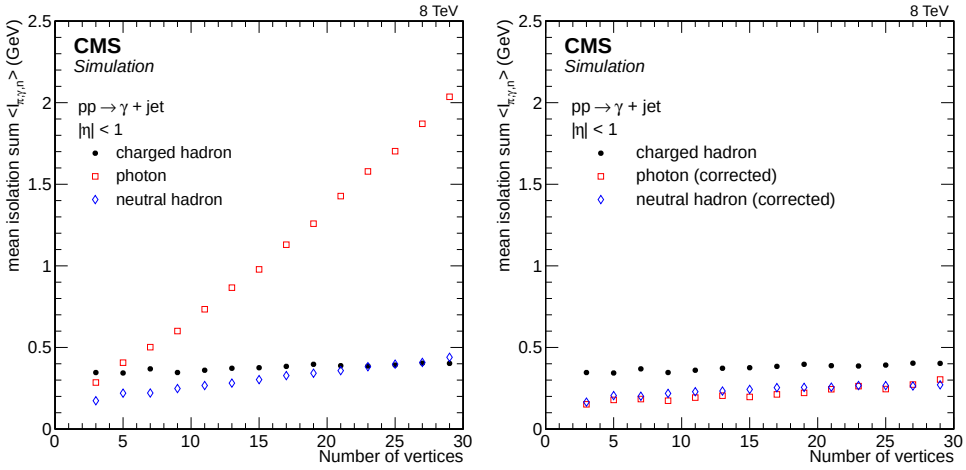

Figure 4.6: Mean value of the isolation variables for photons with $P_T > 50$ GeV in γ + jet events, as a function of the number of reconstructed primary vertices, for events (left) before and (right) after being corrected for pileup using the ρ variable [104].

pairs as charged hadrons and improve the photon isolation. On the other hand, the showers of converted photons have wider transverse profiles. This information can be used to distinguish converted photon from unconverted photon.

In order to reject electron, it is required that there be no charged-particle track with a hit in the inner layer of the pixel detector not matched to a reconstructed conversion vertex, pointing to the photon cluster in the ECAL. This criteria is called 'conversion-safe electron veto'. The efficiency for photons and electrons to pass the conversion-safe electron veto in barrel (endcap) is 99.1% (97.8 %) and 5.3 % (19.6%), respectively.

Sequential application of requirements are chosen to select photon candidates for this analysis. A summary of the photon identification requirements are given in table 4.2. In addition to those requirements, photon candidates are selected with $P_T > 50$ GeV and $|\eta| < 1.44$ and $1.56 < |\eta| < 2.5$.

Table 4.2: Photon selection criteria.

	Barrel	Endcap
H/E	5%	5%
$\sigma_{i\eta i\eta}$	0.011	0.031
PF charged hadron isolation	0.7 GeV	0.5 GeV
PF neutral hadron isolation	0.4 GeV + 0.04 × P_T	1.5 GeV + 0.04 × P_T
PF photon isolation	0.5 GeV + 0.005 × P_T	1.0 GeV + 0.005 × P_T
Conversion safe electron veto	Yes	Yes

4.6 Electrons

The CMS detector benefits from a high resolution silicon tracker and electromagnetic calorimeter. However, the identification and reconstruction of electrons is a challenging task. The significance bremsstrahlung photon emission induced by the tracker materials and the helical flight paths of electrons induced by 3.8 T axial magnetic field cause wide energy deposit along the azimuthal direction.

Two complementary algorithms are used to reconstruct the electrons called 'tracker-driven' and 'ECAL-driven'. The tracker-driven algorithm uses PF algorithm to reconstruct electrons. This algorithm is more suitable for low-P_T electrons as well as electrons inside jets [108]. The ECAL-driven strategy, which is well suited for high-P_T electrons, uses an approach distinct from the PF framework. A 'supercluster' is built from all ECAL energy deposits located within a window of about 0.09 and 0.3 rad in η and ϕ direction respectively. The 'Hybrid algorithm' is used to collect the crystals for the super cluster candidates in barrel and endcap ECAL as was discussed in section 4.5. An alternative algorithm, called 'Island algorithm' is also used for clustering. In Island algorithm, the position of a crystal with an energy above a threshold is found as initial seed and adjacent crystals are added to the cluster through scanning first in ϕ and then in η. The resulting supercluster are matched with track seeds with a dedicated fitting procedure to reconstruct the electrons. The electron candidates which are reconstructed with both algorithm are found to avoid double counting.

Different variables can be used to describe and select the electrons. These variables can be categorized into three groups: identification, isolation and conversion rejection variables. A series of cuts can be applied to select the electrons which will lead to different electron selection efficiency. In the following, the most important electron identification variables which are used in 2012 CMS analysis are listed.

- η difference between supercluster and the associated inner track extrapolated from interaction vertex at ECAL surface ($|\Delta\eta_{in}|$).
- *phi* difference between supercluster and the associated inner track extrapolated from interaction vertex at ECAL surface ($|\Delta\phi_{in}|$).
- The weighted cluster RMS along η as was introduced in section 4.5.

Table 4.3: The cuts for selecting an electron in barrel or endcaps.

Variable	Cut value	
	Barrel	Endcaps
$\lvert\Delta\eta_{in}\rvert$	0.007	0.01
$\lvert\Delta\phi_{in}\rvert$	0.8	0.7
$\sigma_{i\eta i\eta}$	0.01	0.03
H/E	0.15	-
d_0^{vtx}	0.04	0.04
d_z^{vtx}	0.2	0.2
I_{PF}^e/P_T	0.15	0.15

- The ratio of HCAL tower energy just behind the electromagnetic seed cluster in a cone of radius $\Delta R = 0.15$ over the energy of electromagnetic supercluster (H/E).

- Transverse and longitudinal impact parameter of the associated track compared to the associated vertex (d_0^{vtx} and d_z^{vtx}).

- Difference between the inverse of the supercluster energy the inverse of the track momentum ($|1/E - 1/p|$).

Isolation variable is computed by summing over the transverse momenta of photon, charged hadron and neutral hadron PF candidates within a cone of radius $\Delta R = 0.3$ around the electron candidate. The electron PF isolation is defined as

$$I_{PF}^e = \sum P_T^{ch} + max\left(\sum P_T^{nh} + \sum P_T^{\gamma} - \rho A_{eff}, 0\right) \tag{4.4}$$

where ρ is the median energy and A_{eff} is the effective area. The effective area correction needs to be applied to the isolation sum to remove the effect of pileup. The ratio of I_{PF}^e/P_T is used for applying the isolation cut.

In order to select the electron candidate for the analysis performed in this dissertation, a series of cuts are applied on the described variables. Table 4.3 lists the electron identification and isolation variables and corresponding cut values. In addition, selected electrons are required to have $P_T > 20$ and be in allowed η region ($|\eta| < 1.44$ and $1.56 < |\eta| < 2.5$).

4.7 Muons

The muon reconstruction at the CMS is based on the track reconstruction at the tracker and muon detectors. The matched energy deposits in the calorimeters are also used in the muon reconstruction. The tracks in the silicon tracker and muon spectrometers are reconstructed independently and are called tracker tracks and standalone tracks, respectively. Then, two complementary approaches are used for the muon reconstruction from these tracks.

- **Global Muon reconstruction:** standalone muon track is matched with a tracker track and a global muon track is fitted to the hits. This approach is very efficient for the muons with large transverse momenta ($P_T > 200$ GeV).
- **Tracker Muon reconstruction:** all tracker tracks are extrapolated to the muon system while the expected energy loss is considered. If at least one muon segment at the muon system is matched with the track the tracker track is considered as a tracker muon. This approach is more efficient at low momentum compared to the global muon approach.

The majority of muons are reconstructed either as global or tracker muon. However, if both approaches fail and a standalone track left without any tracker track, third category of muons, called standalone muon only, are saved ($\approx 1\%$). All the muon candidates are merged into a single collection, each one containing information from tracker, standalone and global fits. The candidates which are reconstructed by both approach are merged into a single candidate [109].

As with electron, additional information is associated with the muon candidate which are useful for muon quality identification and selection. Some of the main variables are [110]

- The number of hits both in tracker and muon system as well as number of segments in muon system.
- The distance between the primary vertex and the transverse and longitudinal impact parameters (d_0 and d_z).
- The χ^2 of the fit for both tracker and global muon.

Table 4.4: The cuts for selecting a muon in barrel or endcaps.

Variable	tight	loose
	PF muon	PF muon
	Global muon	Global or tracker muon
d_0	<0.2 cm	-
d_z	<0.5 cm	-
Global track fit χ^2/n_{dof}	<10	-
Global track fit $n_{segment}$	>1	-
number of pixel tracker hits	>0	-
number of silicon tracker hits	>5	-
number of valid muon chamber hits	>1	-
I^{μ}_{rel}	< 0.12	< 0.2

In addition to the identification requirements, a further quality cut on isolation is performed to reduce contamination from muons that originate from hadronic processes. The isolation variable is calculated using PF candidates in a cone of a given size 0.4 around the muon track direction. The energy of the neutral hadrons and photons are corrected for pile-up contamination by using an estimate of the total contribution of PU tracks $\Delta\beta$

$$I^{\mu}_{PF} = \sum P^{ch}_T + max\left(\sum P^{nh}_T + \sum P^{\gamma}_T - \Delta\beta \sum P^{PU}_T, 0\right) \tag{4.5}$$

where $\sum P^{PU}_T$ is the sum of transverse momenta of tracks associated to non-leading vertices.

Frequently, muons originating from the decays of W and Z bosons have higher P_T than those from other sources like hadron decays. Therefore, the separation between muons from different sources is improved by normalizing the isolation energy to the P_T of the muon, giving the relative isolation variable $I^{\mu}_{rel} = I^{\mu}_{PF}/P_T$.

The selection cuts are made on these quantities to minimize the contribution of the muons originating from the cosmic rays, heavy flavor decays and hadronic showers. Two selection working points are used in this analysis called tight and loose collections. Table 4.4 list the various cuts applied to select loose and tight muons. Tight muons are required to have $P_T > 26$ GeV and $|\eta| < 2.1$ to match the HLT criterion used to collect data, as described in section 5.1.2. Less restrictive cuts are applied to select loose muons with $P_T > 10$ GeV and $|\eta| < 2.5$ which will be used to veto events with additional muons.

4.8 Jets

The QCD confinement requires that the original quark or gluon is never seen in its free states and they bind off into colorless hadrons. In a hard scattering processes, a quark or gluon fragments or hadronises immediately after being produced. The produced spray of the hadrons travel more or less in the direction of the final-state parton, collectively called a jet. Over the years, various methods are proposed and used to cluster hadrons and define jets [111]. Jet algorithms are usually involve one or more parameters that indicate how two particles are in a same or separate jet. CMS uses $anti-k_t$ algorithm to define the jets [112].

The $anti-k_t$ is a sequential recombination algorithm which uses the following distances

$$d_{ij} = min\left(\frac{1}{P_{Ti}^2}, \frac{1}{P_{Tj}^2}\right)\frac{\Delta_{ij}^2}{R^2} \tag{4.6}$$

$$d_{iB} = \frac{1}{P_{Ti}^2} \tag{4.7}$$

where $\Delta_{ij} = (y_i - y_j)^2 + (\phi_i - \phi_j)^2$ and P_{Ti}, $y_i = \frac{1}{2} ln \frac{E+p_z}{E-p_z}$ and ϕ_i are the transverse momentum, rapidity and azimuth of particle i. R is radius parameter similar to radius in cone algorithm. The distances in equation 4.6 are used as follows:

step 1: work out all the d_{ij} and d_{iB} for all particles according to equation 4.6.

step 2: find the minimum of the d_{ij} and d_{iB}.

step 3: if the minimum is d_{ij}, recombine particles i and j into a single particle and return to step 1.

step 4: if the minimum is d_{iB} declare i as a jet and remove it from the list of particles. Return to step 1.

step 5: stop the procedure when no particles remain.

The value of d_{ij} is determined by the transverse momentum of particles and separation between particles (Δ_{ij}). If there is a hard particle with high transverse momentum between soft particles, the minimum of d_{ij} occurs when i is hard particle and j is a soft particle close to the hard particle. Therefore a hard particle simply accumulate all the soft particles within a circle of radius R through the $anti-k_t$ algorithm and leads to a perfectly conical jet. If another hard particle is present in $R < \Delta_{12} < 2R$ distance from the first hard particle, there will be two hard jets. If

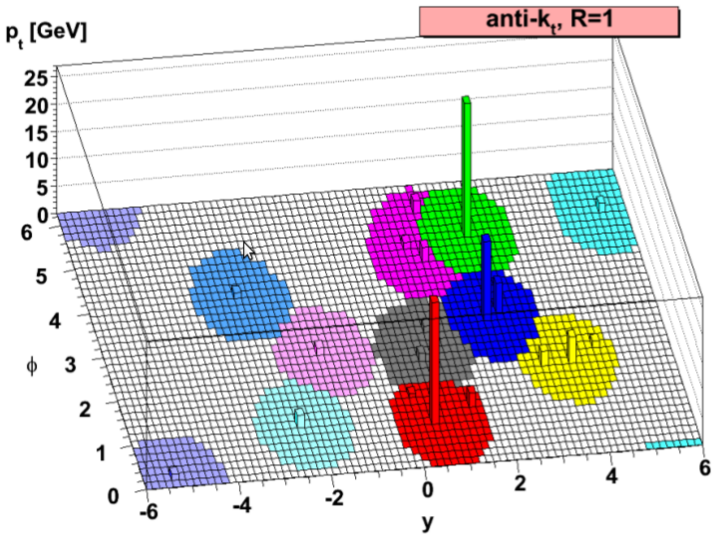

Figure 4.7: A sample parton-level event which is clustered by $anti-k_t$ algorithm [112].

$\Delta_{12} < R$, hard particles will cluster to form a single jet. Figure 4.7 shows a sample parton-level event which is clustered by $anti - k_t$ algorithm. The hard jets are all circular with $R = 1$ and just softer jets have defected shapes. The $anti-k_t$ algorithm is an infra-red and collinear safe algorithm. The jet boundaries are resilience with respect to soft radiation because soft particles tend to cluster with hard ones and not among themselves.

Jets are reconstructed from several types of inputs:

- **gen-jets**: stable simulated particles, except for neutrinos, are clustered after hadronization and before interaction with the detector.
- **PF-jets**: all PF candidates are clustered without distinction of type and any energy threshold.
- **calo-jets**: calorimeter towers in each HCAL cells and underlying ECAL crystals are clustered.

which are depicted in figure 4.8

The four-momentum vectors of PF candidates are used to reconstruct jets by the $anti - k_t$ algorithm with R=0.5 in CMS. PF jets take advantage of the excellent momentum and spatial resolutions for the charged hadrons and photons inside a jet, which together constitute 85% of the jet energy. The PF jet momentum and spatial

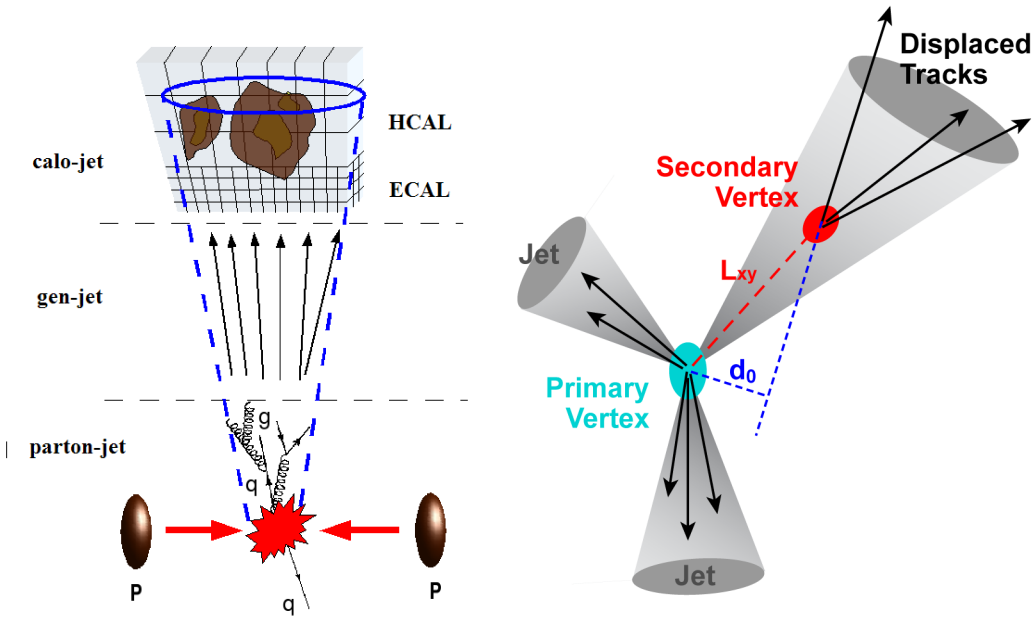

Figure 4.8: Left: schematics of the jet reconstruction from parton level, hadron level and caloremeter level objects. Right: a b-jet with displaced track and secondary vertex.

resolutions are greatly improved with respect to calorimeter jets. Gen-jets are used as a reference to compare the PF-jet performance to the calo-jet performance in [103]. It is shown that the PF-jets are better matched with gen-jets compared to calo-jets and can be used in analysis down to P_T's as small as 5 GeV/c.

Although several correction factors exist to bring the energy scale of calo-jets up to unity PF-jets have an energy scale very close to unity and need only small residual corrections. The default jet-energy correction [113] brings the jet energy measured in the detector to the energy of the final state gen-jet or parton-jet which depends on the jet P_T and η. First, the energy clustered inside a jet due to the underlying event, electronic noise and pileup are measured using the minimum bias events (L1 correction). Then the energy of the reconstructed jet is corrected to be matched with gen-jet and being uniform in P_T and η using dijet, Z+jet and γ+jet Sample (L2 and L3 corrections) [114].

The analysis considers jets within $\eta < 2.5$ whose calibrated transverse energy is greater than 30 GeV and pass a set of quality cuts. PF jets must have more than one constituent, and they must have neutral hadronic, charged electromagnetic, and neutral electromagnetic energy fractions smaller than 99%, and charged hadronic energy fraction and charged particle multiplicity larger than 1%.

4.9 b-tagging

B-tagging or the identification of b-jets is a critical feature for many high energy processes. for example, b-tagging in top physics reduces the overwhelming background processes. The properties of the bottom hadrons can be used to identify a jet originating from b-quark.

Hadrons containing bottom quarks have sufficient lifetimes ($\tau \approx 10^{-12}$) that they travel some distances before decaying ($\approx$ hundreds of micro meters). This travel distance leads to the presence of a secondary vertex originated from the B decay. When the tracks from the secondary vertex are extrapolated to the primary vertex, they will have a rather large impact parameter. The impact parameter is defined as the smallest distance between the track trajectory and the primary vertex (d_0) which is shown in figure 4.8 right. Furthermore, the bottom quark is much more massive than anything it decays into and its decay products tend to have higher momentum component perpendicular to the original direction of the bottom quark. This causes b-jets to be wider, have higher multiplicities and invariant masses, and also to contain low-energy leptons with momentum perpendicular to the jet.

A variety of algorithms has been developed and used by CMS Collaboration to discriminate between bottom and light-parton jets based on variables such as the impact parameters of charged-particle tracks, the presence or absence of a lepton, the properties of reconstructed decay vertices and combination of these properties [115]. Each of these algorithms yields a single discriminator value for each jet in which thresholds on these discriminators define a working point with a given tagging and miss-tagging (the efficiencies to tag non-b jets) efficiencies.

The Combined Secondary Vertex (CSV) algorithm is one of the most powerful and successful of these algorithms. CSV is a complex approach which uses of secondary vertices together with track-based lifetime information. Secondary vertex candidates should pass the following requirements:

- shared tracks between the secondary and primary vertices should be less than 65%.
- secondary vertex candidates which have a radial distance of more than 2.5 cm with respect to the primary vertex and their mass exceeding 6.5 $\frac{\text{GeV}}{c^2}$ are rejected.

- the candidates are rejected if the flight direction of each candidate is outside a cone of $\Delta R < 0.5$ around the jet direction.

The efficiency of the secondary vertex reconstruction is about 65%. In addition to the secondary vertex, CSV uses the variables such as the flight distance significance in the transverse plane, the vertex mass, the number of tracks at the vertex, the ratio of the energy carried by tracks at the vertex with respect to all tracks in the jet, the pseudo-rapidities of the tracks at the vertex with respect to the jet axis and the number of tracks in the jet.

The distributions of most of the variables are significantly different for c-jets and other light-jets. Therefore, two likelihood ratios with different weights for c-jet and light jet backgrounds are built from these variables and are combined into a single discriminating variable. The CSV b-tag discriminator varies between 0 to 1. Three working points are defined in this range called loose (CSV discriminator = 0.244), medium (CSV discriminator = 0.679) and tight (CSV discriminator = 0.898) working points in which the miss-tag rates are 10%, 1% and 0.1%, respectively. For loose selection a b-jet tagging efficiency of $\approx$ 80% and for medium and tight selections a b-jet tagging efficiency of $\approx$ 55 % is achieved. The CSV algorithm do the the best performance of b-tagging for medium and tight working points. In this dissertation, the medium working point is used to select b-tagged jets. In addition to the selection of b-jet, CSV discriminator is a very good variable which will be used to extract signal events that will be discussed in section 5.6.1.

4.10 Missing Transverse Energy

The vector momentum imbalance in the plane perpendicular to the beam direction is known as missing transverse momentum ($\overrightarrow{E}_T^{miss}$) and its magnitude is called missing transverse energy (MET). MET is the transverse momentum that must have been carried by something invisible such as neutrinos. MET is one of the most important variables for reducing the QCD and Drell-Yan backgrounds in the analysis which are involved with the leptonic decays of W bosons such as this analysis.

PF MET is reconstructed as the negative vector sum of the transverse momen-

tum of all PF candidate particles in the event:

$$\overrightarrow{E}_T^{miss} = -\sum_{n=PFcandidates} (E_n \sin\theta_n \cos\phi_n \hat{x} + E_n \sin\theta_n \sin\phi_n \hat{y}) \quad (4.8)$$

The magnitude of the $\overrightarrow{E}_T^{miss}$ can be affected by various sources. The minimum energy thresholds in the calorimeters, minimum P_T threshold in tracker and non-linear response of calorimeters would vary the $\overrightarrow{E}_T^{miss}$. As was discussed in section 4.8, jet energies are corrected due to the particle level jet energies. The effect of this source is reduced significantly by propagating the jet energy corrections into MET calculation. Another source is related to the PF candidates from the pileup interactions. The magnitude of the $\overrightarrow{E}_T^{miss}$ produced from the pileup interactions is small because neutrinos are rarely produced in inelastic pp scattering (minimum bias) interactions. Charge hadron candidates from pileup are well balanced and $\overrightarrow{E}_T^{miss}$ originate from the neutral hadrons. The effects of pile-up is reduced by subtracting charged hadrons and compensating for remaining imbalance from neutral hadrons [116].

Although particles are produced uniformly in ϕ, there is a shift of MET x and y components in both data and simulation which leads to a ϕ-asymmetry in MET. The sources of the asymmetry is from imperfect detector alignment, ϕ dependence of the calibration and a short distance between the center of the detector and the beam-line. The MET ϕ-asymmetry increases linearly with the number of reconstructed vertices. The x and y components of MET are corrected for both data and simulation considering number of reconstructed vertices event by event.

Anomalous $\overrightarrow{E}_T^{miss}$ measurements existed in data from calorimeter noise and beam halo. The beam halo phenomenon are showers of secondary particles produced through the intraction of protons with the beam collimators or the residual gas particles. Some methods are used by CMS collaboration to identify, and sometimes to correct, $\overrightarrow{E}_T^{miss}$ for these effects which is explained in [117].

In the 2012 data, anomalous events with extra high MET from different sources were also observed. A misfire of the HCAL laser calibration system in the HB, HE, or HF regions causes false signal production. These events are identified and removed from the collected data. Another source of fake $\overrightarrow{E}_T^{miss}$ was due to noise in silicon strip tracker. In such events the transverse momenta of the reconstructed

tracks can exceed 100 GeV which can vary the $\overrightarrow{E}_T^{miss}$ significantly. These events are identified by the number of clusters in the silicon strip and pixel detectors and extracted from data samples [116].

Chapter 5

Analysis strategy

In previous chapters all the necessary pieces to search for anomalous top quark FCNC processes have been presented. In the following, they will be used to perform a full analysis to study the anomalous $tq\gamma$ ($q = u, c$) interactions in a production of single top quark production in association with a photon in proton-proton collisions.

5.1 Datasets and simulated samples

5.1.1 Signal modelling and generation

As was discussed in section 2.3.2, model independent approach is followed to search for top quark anomalous FCNC signs by various experiments. This approach is also followed in this analysis. It is worth repeating the Lagrangian related to the anomalous $tq\gamma$ interactions from equation 2.22 with a small modifications as follows

$$-\mathcal{L}_{eff} = eQ_t\kappa_{tu\gamma}\bar{u}\frac{i\sigma^{\mu\nu}q_\nu}{\Lambda}tA_\mu + eQ_t\kappa_{tc\gamma}\bar{c}\frac{i\sigma^{\mu\nu}q_\nu}{\Lambda}tA_\mu + h.c. \tag{5.1}$$

where Q_t is equal to 2/3 which is the top quark electric charge and other parameters are described in section 2.3.2. The Q_t factor makes the Lagrangian in equation 2.22 similar to what is used in previous searches by LEP and HERA as were mentioned in section 2.7. Therefore, the bounds would be comparable with previous bounds. It was discussed in section 2.6 that this Lagrangian leads to the production of top quark in association with a photon.

In order to generate signal events, PROTOS (PROgram for TOp Simulations) event generator is used [118]. PROTOS is a leading order generator for some new

physics processes involving top quark. It has generators for single top and top pair production with anomalous Wtb couplings, as well as single top and top pair production involving FCNC couplings. In this generator, special attention is devoted to providing theoretical values of observables such as angular asymmetries, spin correlations, polarization, etc. PROTOS uses effective Lagrangian introduced in equation 5.1 (without Q_t factor) to produce single top quark with a photon in p-p collisions.

The $tu\gamma$ and $tc\gamma$ FCNC processes do not have any interference in a general scenario therefore the signal sample for each channel is generated independently. $tu\gamma$ signal sample is generated while $\kappa_{tc\gamma}$ is set to zero and $tc\gamma$ signal sample is generated while $\kappa_{tu\gamma}$ is set to zero. Although the cross section of anomalous $t\gamma$ production is a function of the anomalous couplings, kinematic distributions of the final state particles are independent of the anomalous couplings. Therefore, signal samples are generated for an arbitrary value of anomalous couplings ($\kappa_{tu\gamma} = \kappa_{tu\gamma} = 0.1$).

The signal samples have been generated with the $Q-$scale set to the nominal top quark mass 172.5 GeV. Various Monte Carlo signal samples are generated to study the systematic uncertainties due to factorization/renormalization scales and top quark mass. For each variation of the renormalization/factorization scales and top mass one Monte Carlo sample has been generated. The considered variations for $Q-$scale are: $4 \times Q^2$ and $0.25 \times Q^2$. To take into account the systematic uncertainty due to top quark mass, two samples with ± 2 GeV around the nominal top mass are produced.

In order to remove infra-red divergence in cross section due to the soft photon in final state, a minimum threshold on the transverse momentum of photon $P_T > 30$ is applied at the generator level. In the production of signal events, the top quark branching ratio to a bottom quark and a W boson is assumed to be 100%. Then the W boson is free to decay only into a charge lepton (e, μ and τ) and neutrino. One can write the quadratic dependence of the cross section on the anomalous couplings considering the minimum cut on the photon P_T as:

$$\begin{aligned} \sigma(pp \to t\gamma \to l\nu b\ \gamma) &= 29.86\ |\kappa_{tu\gamma}|^2 (pb)\ (\kappa_{tc\gamma} = 0), \\ \sigma(pp \to t\gamma \to l\nu b\ \gamma) &= 3.17\ |\kappa_{tc\gamma}|^2 (pb)\ (\kappa_{tu\gamma} = 0) \end{aligned} \tag{5.2}$$

In this analysis, we will focus on the muonic decay of W boson from top quark

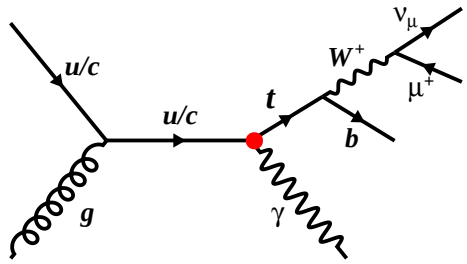

Figure 5.1: Representative Feynman diagram for anomalous single top production in association with a photon due to the anomalous $tu\gamma$ and $tc\gamma$ FCNC interactions in p-p collisions.

decay. Less sensitivity would be obtained in electron channel (when W boson decays to an electron and neutrino) because of the presence of two electromagnetic objects at the final state. In figure 5.1, a representative Feynman diagram of signal channel is shown. In $tu\gamma$ signal channel a valence quark interact with a gluon while in $tc\gamma$ signal channel a sea quark interact with a gluon when top quark is produced in final state. Due to the larger parton distribution of valence quarks, cross section of the $tu\gamma$ signal channel is much larger than $tc\gamma$ signal channel. On the other hand, anti-top quark is produced when a sea quark is involved in both $tu\gamma$ and $tc\gamma$ channel. Therefore, anomalous top is produced more than anti-top in $tu\gamma$ signal channel.

The partial decay width of the top quark with flavour violating interactions are given by

$$\Gamma(t \to q\gamma) = Q_t^2 \frac{\alpha}{2} m_t |\kappa_{tq\gamma}|^2 \tag{5.3}$$

For numerical calculation we set $m_t = 172.5$ GeV, $m_W = 80.419$ GeV, $s_W^2 = 0.234$ and $\alpha = 1/128.92$. The corresponding branching ratio is then has the following form

$$\mathcal{B}R(t \to q\gamma) = 0.2058 \ |\kappa_{tq\gamma}|^2 \tag{5.4}$$

It is remarkable that PROTOS generates signal sample at Leading Order. The full Next to Leading Order QCD corrections to the signal cross section has been calculated in [119]. It is interesting to note that the NLO QCD corrections can enhance the total cross section up to 40% at the LHC. In figure 5.2, the K factors $\frac{\sigma_{NLO}}{\sigma_{LO}}$ as a function of the photon transverse momentum cut is shown. The $K-$factors decrease with the increasing transverse momentum cut. In [119], it has been shown

that the NLO corrections does not depend strongly on the scale dependence which makes the theoretical predictions stable. The K-factors are considered to be 1.375 for both signal channel.

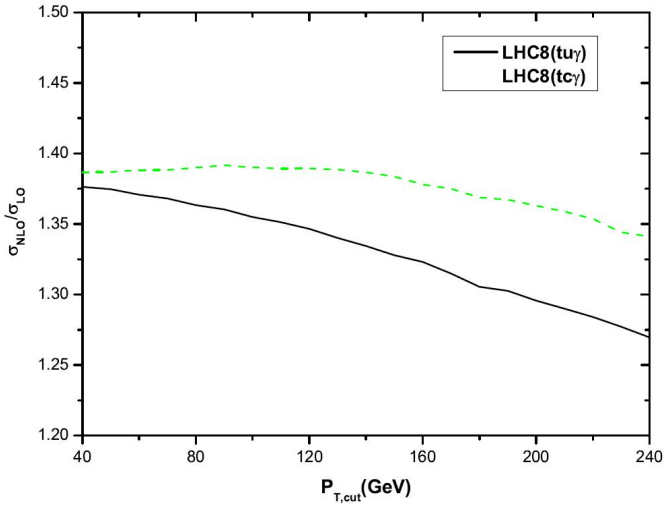

Figure 5.2: $K-$factor for the signal process as a function of photon transverse momentum cut at the LHC with the center-of-mass energy of 8 TeV [119].

5.1.2 CMS data events

In this dissertation the data consists of 19.768 fb^{-1} of integrated luminosity, recorded by CMS experiment at LHC during 2012 at the center-of-mass energy of 8 TeV are analysed. The analysis is restricted to the lumi sections parts of an LHC run validated in the final JSON file (see table 5.1). As was already mentioned, we have concentrated on the muonic decay of the W boson in the top quark, so events are selected from the single muon primary datasets, listed in table 5.1.

Events are selected if they pass the HLT path "$HLT\_IsoMu24\_eta2p1$". This path requires an isolated muon candidate with $p_T > 24$ GeV/c and $|\eta| < 2.1$ in each event during the online event reconstruction [120].

5.1.3 Background simulated samples

The SM background which can mimic the signatures of the signal processes can be grouped into two categories: those with a real prompt photon in the final state and those with a fake photon in the final state. Each category can be divided into processes with and without top quark in the final state.

Table 5.1: The datasets and Json file used for the analysis.

Dataset	Integrated Luminosity pb^{-1}
/SingleMu/Run2012A-22Jan2013-v1/AOD	889
/SingleMu/Run2012B-22Jan2013-v1/AOD	4429
/SingleMu/Run2012C-22Jan2013-v1/AOD	7140
/SingleMu/Run2012D-22Jan2013-v1/AOD	7317
Cert_190456-208686_8TeV_22Jan2013ReReco_Collisions12_JSON.txt	

The background processes containing real photon are

- $W\gamma$-jets and $Z\gamma$-jets: among the various di-boson processes produced in hadron colliders, $W\gamma$ and $Z\gamma$ have the highest rate. These two SM backgrounds contribute to the signal region when $W \to \mu\nu$ and $Z \to \mu^+\mu^-$. The $W\gamma$ and $Z\gamma$ are produced at tree level through three processes: initial state radiation (ISR) where a photon is produced from one of the incoming partons, final state radiation (FSR) where a photon is radiated off one of the charged leptons from the vector boson decay, and finally when a photon is produced in s-channel via triple gauge interactions ($WW\gamma$). These two samples are generated by MadGraph [97].

- $WW\gamma$: the triple gauge boson associated production sample is generated with MadGraph [97].

- γ-jets: this SM background can contribute to the final state when a muon from a jet is misidentified as an isolated tight muon. This background is generated with Pythia [93] in different photon P_T bins.

- $t\bar{t}\gamma$: ISR from quarks and FSR from top, W boson, final leptons and partons in SM $t\bar{t}$ production is an important background in this analysis. The $t\bar{t}\gamma$ sample is generated with MadGraph [97].

- $t\gamma$ and $\bar{t}\gamma$: Single top quark production through the s-channel, t-channel and tW-channel with ISR and FSR is an irreducible background in this analysis which is generated with MadGraph [97].

and the backgrounds with fake photon are

- Dibosons: The Pythia is used to model the diboson processes, including WW, WZ and ZZ production. The cross sections of diboson processes are calculated

at NLO accuracy in [121].

- W-jets and $Z/\gamma(\rightarrow l^+l^-)$-jets: For these two SM processes, inclusive samples including any number of jets are generated. Huge cross section of these processes leads to a considerable contribution in signal region through a fake photon. The cross section of inclusive W-jets and $Z/\gamma(\rightarrow l^+l^-)$-jets processes are calculated at NNLO accuracy in [122].

- $t\bar{t}$ and single top processes: An inclusive sample is generated for $t\bar{t}$ with MADGRAPH in which all decay modes of the two W bosons from the top quark decays are included. Separated samples for single top and anti-top quark production is generated with POWHEG [123]. The cross sections for the $t\bar{t}$ and single top quark production are calculated at next-to-next-to-leading logarithmic (NNLL) accuracy in [124].

A full list of the MC samples and their cross sections used in the analysis described in this dissertation are summarized in table 5.2.

5.1.4 NLO modelling of $W\gamma$-jets and $Z\gamma$-jets

For the theoretical SM cross section, the MADGRAPH event generator is used for the simulation of $W\gamma$-jets and $Z\gamma$-jets processes. The cross sections are calculated at LO, so we need to scale the LO prediction to the NLO.

For $W\gamma$-jets and $Z\gamma$-jets processes, k-factor is defined as function of the transverse photon energy

$$K = \frac{d\sigma_{NLO}/dE_T^{\gamma}}{d\sigma_{LO}/dE_T^{\gamma}} \tag{5.5}$$

Where $d\sigma_{NLO}/dE_T^{\gamma}$ and $d\sigma_{LO}/dE_T^{\gamma}$ are the next-to-leading order and leading order differential cross-sections, respectively.

The $K-$factor for $W\gamma$-jets process is obtained using the Baur NLO generator [125] that calculates the cross section of $W\gamma$-jets including the NLO QCD corrections. The corresponding $K-$factor versus the transverse momentum of the photon is presented in figure 5.3 (left). In order to obtain a functional form of the $K-$factor, the distribution of the photon transverse momentum is fitted to a second order polynomial. The coefficients of the polynomial after the fit are:

Table 5.2: List of all Monte Carlo datasets and their cross sections used in this analysis.

Sample	Cross-section [pb]
TTGJets_8TeV-madgraph	1.444 (LO)
WGToLNuG_TuneZ2star_8TeV-madgraph-tauola	461.6 (LO)
ZGToLLG_8TeV-madgraph	132.6 (LO)
WWGJets_8TeV-madgraph_v2	0.528 (LO)
G_Pt_50to80_TuneZ2star_8TeV_pythia6	3322.309 (LO)
G_Pt_80to120_TuneZ2star_8TeV_pythia6	558.286 (LO)
G_Pt_120to170_TuneZ2star_8TeV_pythia6	108.006 (LO)
G_Pt_170to300_TuneZ2star_8TeV_pythia6	30.122 (LO)
G_Pt_300to470_TuneZ2star_8TeV_pythia6	2.138 (LO)
G_Pt_470to800_TuneZ2star_8TeV_pythia6	0.211 (LO)
TTJets_MassiveBinDECAY_TuneZ2star_8TeV-madgraph-tauola	234 (NLO)
DYJetsToLL_M-50_TuneZ2Star_8TeV-madgraph-tarball	3503.71 (NNLO)
WJetsToLNu_TuneZ2Star_8TeV-madgraph-tarball	36257.2 (NNLO)
WW_TuneZ2star_8TeV_pythia6_tauola	54.838 (LO)
WZ_TuneZ2star_8TeV_pythia6_tauola	32.316 (LO)
ZZ_TuneZ2star_8TeV_pythia6_tauola	8.06 (LO)
T_t-channel_TuneZ2star_8TeV-powheg-tauola	56.4 (NLO)
Tbar_t-channel_TuneZ2star_8TeV-powheg-tauola	30.7 (NLO)
T_s-channel_TuneZ2star_8TeV-powheg-tauola	3.79 (NNLL)
Tbar_s-channel_TuneZ2star_8TeV-powheg-tauola	1.76 (NNLL)
T_tW-channel-DR_TuneZ2star_8TeV-powheg-tauola	11.1 (NNLL)
Tbar_tW-channel-DR_TuneZ2star_8TeV-powheg-tauola	11.1 (NNLL)
tGamma_8TeV_madgraph	0.881 (LO)

$p_0 = 1.46604$, $p_1 = 0.00923692$, $p_2 = -1.48871 \times 10^{-6}$. The variation of the renormalization and factorization scales provide some uncertainty on the $K-$factor. The variation of the factorization and renormalization scales by a factor of two leads to almost 10% variation on the $K-$factor.

We also perform the same way as $W\gamma$-jets process to calculate the $K-$factor of the $Z\gamma$-jets process as a function of the photon E_T. The E_T^{γ} dependent $K-$factor is applied since the shape of photon transverse energy is an important variable in this analysis. Figure 5.3 (right) shows the calculated $K-$factor versus photon E_T for $Z\gamma$-jets process with the Baur NLO program.

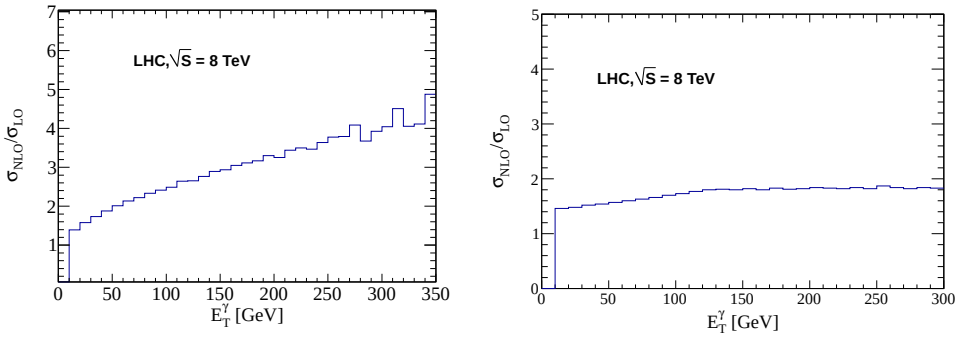

Figure 5.3: The NLO $K-$factors for $W\gamma$ (left) and $Z\gamma$ (right) as a function of transverse energy of photon at the LHC with the center-of-mass energy of 8 TeV.

5.2 Event selections and reconstruction

5.2.1 Preselection

After selection and identification of different physical objects in the final state, which were discussed in chapter 4, a series of cuts are applied to select events. The selection criteria are optimized to reduce the contributions from SM background as much as possible while enhancing the signal. On the other hand, it is tried to find a signal region in which all SM backgrounds could be under control.

In addition to the trigger criteria which guaranties the presence of an isolated muon in the events, exactly one tight muon is demanded. Tight muon is a muon satisfying the tight working point and kinematic criteria described in section 4.7. Tight muons benefit from the more precise lepton identification in the offline event reconstruction. This requirement removes events with multiple leptons. In order to suppress background contaminations with two same flavor charged leptons in the final state such as diboson and Drell-Yan, events containing additional loose muon are discarded. Muons with loose identification and isolation criteria called loose muon defined in section 4.7. Events with one or more electrons satisfying the loose working point and kinematic criteria described in Section 4.6 are vetoed. This requirement removes opposite flavor dilepton events with one electron leg.

One of the main features of the signal channel is the presence of a high energetic photon in the final state. Each event is required to have exactly one tight photon with the criteria discussed in section 4.5. Such a requirement suppresses backgrounds with no prompt photon in the final state as well as diphoton processes. In order to use the signature of neutrino in signal events, missing transverse energy is required

to be greater than 30 GeV. This requirement suppresses the γ-jets, Drell-Yan and $Z\gamma$-jets backgrounds and any background with no W boson in the final state.

Events must contain at least one jet with the condition defined in section 4.8. Another useful information that can be used to reduce the contribution of the backgrounds is the presence of a b-jet in the signal final state. Any event with more than one b-tagged jet in the final state is vetoed. This criteria suppresses the background from the $t\bar{t}$ and $t\bar{t}\gamma$ events.

Finally, it is required that $\Delta R(l,\gamma) > 0.7$ and $\Delta R(b-jet,\gamma) > 0.7$ to have well separated objects and to reject FSR photons from high p_T muon or final states partons.

5.2.2 Top quark reconstruction

Once pre-selection is done, a supposedly signal-enriched sample has been selected from real data. One important feature of the signal is that the selected muon and b-jet are the decay products of the top quark. On the other hand, photon recoils against top quark in signal events. Therefore, it is essential to reconstruct top quark from the physical objects to distinguish signal from SM backgrounds better.

Before the reconstruction of top quark, one needs to reconstruct the W boson from its decay products. It is assumed that the x and y components of the missing momentum are entirely due to the neutrino from W boson decay. In addition, selected muon is assumed to be the decay product of W boson. The W boson mass constraint is used to find the z momentum component of the neutrino as follows [126].

$$M_W^2 = (E_\mu + \sqrt{E_T^{miss^2} + P_{z,\nu}^2})^2 - (\overrightarrow{P}_{T,\mu} + \overrightarrow{E}_T^{miss})^2 - (P_{z,\mu} + P_{z,\nu})^2 \tag{5.6}$$

This equation has in general two solutions:

$$P_{z,\nu} = \frac{aP_{z,\mu}}{P_{T,\mu}^2} \pm \sqrt{\frac{a^2 P_{z,\mu}}{P_{T,\mu}^4} - \frac{E_\mu^2 E_T^{miss^2} - a^2}{P_{T,\mu}^2}} \tag{5.7}$$

with

$$a = \frac{M_W^2}{2} + \overrightarrow{P}_{T,\mu}.\overrightarrow{E}_T^{miss} \tag{5.8}$$

The $P_{z,\nu}$ obtained from the equation 5.7 has an imaginary part if the discrim-

inant becomes negative. This happens due to the finite resolution of the missing transverse energy, lepton momentum resolution and the finite W boson width. In case that there is only imaginary solution we take the real part of the solution in order to keep the events with enough statistics. In case of having two real solutions, the solution with the smallest abstract value is chosen [127].

The W boson four momentum can be reconstructed after finding the $P_{z,\nu}$. Then one should assign a jet to reconstruct the top quark. A jet with the highest value for b-tag discriminator in each event is tagged as b-jet. The four momentum of the W boson and b-jet are used to reconstruct the top quark.

5.2.3 Main selection

The requirement on the number of b-tag jets determines whether the $t\bar{t}$ or $W\gamma$-jets is the most important SM background. In section 5.2.1 $t\bar{t}$ events are reduced by rejecting events with more than one b-jet. Therefore, the signal region defined by the pre-selection cuts is enriched by the SM processes with light jets at the final state.

In figure 5.4, the distribution of reconstructed top quark mass for the SM backgrounds, FCNC signal and real data is shown. It is clear that a huge fraction of the SM background is from the $W\gamma$-jets process. The reconstructed top mass peak of those SM backgrounds which do not contain a top quark, such as $W\gamma$-jets, $Z\gamma$-jets, diboson and etc, is far from the real top mass. On the other hand, events from the SM processes with top quark in the final state and signal are gathered around the top quark mass in top mass plot. Therefore, a top mass window is defined around the measured top quark mass to reduce the contribution of SM backgrounds. Final requirement is discarding events with the reconstructed top mass out of $130 < m_{top} < 220$ GeV.

The phase space defined by the pre-selection and top mass window cuts is called signal region.

5.3 Multivariate analysis

One of the most important challenges to the searches for rare signals in large data sets is to find suitable variable with high discrimination power after the pre-selection.

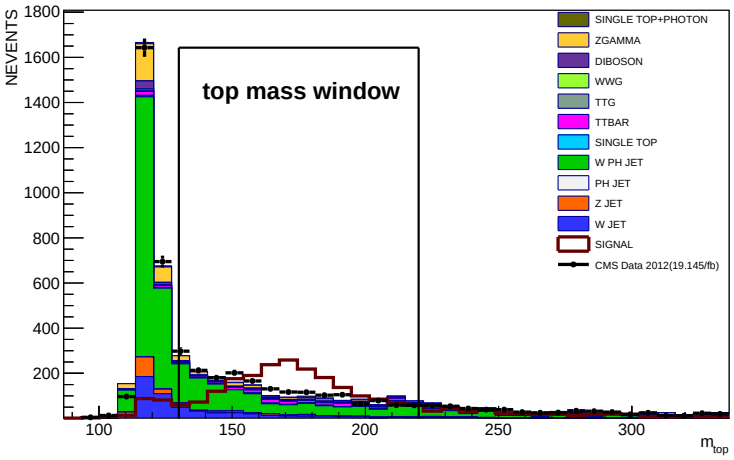

Figure 5.4: The top mass distribution for data, signal, and all backgrounds. All backgrounds except for W+jets are based on simulation.

A variable with very high discrimination power is able to extract a maximum of the available information from the data. In most of the analysis, it is not possible to find a simple kinematic variable with a high discrimination power. On the other hand, there are always some variables which has moderate discrimination power between signal and background events. Furthermore, individual cuts in each observable are not able to exploit possible correlations among the different observables.

In order to combine several discriminating variables into a powerful variable, MultiVariate Analysis (MVA) is most commonly used in high energy physics analysis. The MVA framework has been also used for various disambiguation and identification problems in the official CMS event reconstruction, for example for b-tagging or electron identification.

A large set of advanced multivariate analysis techniques are implemented in the Toolkit for Multivariate Data Analysis (TMVA) package [128]. TMVA provides the ability to map from the N-dimensional phase space of the N-input variables to one dimension. A classifier output derived from the input variables determines if the event is signal or background like.

In order to classify signal and background events, MVA method has to be trained and tested. First, the classifier method is trained using a set of signal and background MC event candidates within the TMVA. In this step, MVA method is used to built the final variable while the parameters of the method are optimized to separate signal-like from background-like events with respect to input variables. Second,

a separated signal and background MC samples are used to test the training procedure. Finally, the training of the classifiers are applied to data, background and signal events.

5.3.1 Boosted decision tree

Decision trees

Decision trees are tree-structured binary classifiers that consist of a sequential cuts on discrimination variables. In this method the D-dimensional space of discrimination variables are split in many rectangular sub-spaces by applying a series of cuts on the input variables. The tree starts from a root node and is split into intermediate nodes and ends up with leafs as is shown in figure 5.5. At each node, one variable and the corresponding cut value that provide the best separation of the data is chosen. The quality of separation is typically measured in terms of the Gini index as

$$\text{Gini index: } p.(1-p) \tag{5.9}$$

where $p = S/(S+B)$ denotes the purity. The variable and cut in each node is chosen by requiring the maximum increase in the Gini index between the initial node and weighted sum of daughter nodes.

The leaves, i.e. the final nodes, determine whether the event is signal or background according to their purity. If the purity of the leaf is less (greater) than 0.5 it is considered as signal (background).

Boosting

Decision trees are fairly sensitive to statistical fluctuations in the training data sample which make it less powerful than other multivariate techniques. However, boosting method can make decision trees more robust and also increase its performance. Boosting methods combine many different sensitive trees into a one strong forest. In this method, all trees are trained by data while the misclassified events are reweighed for new training. Then the classification of a test event is obtained by a weighted average of the responses of each of the individual decision trees in the forest.

Three are different boosting algorithms that employ different prescriptions of

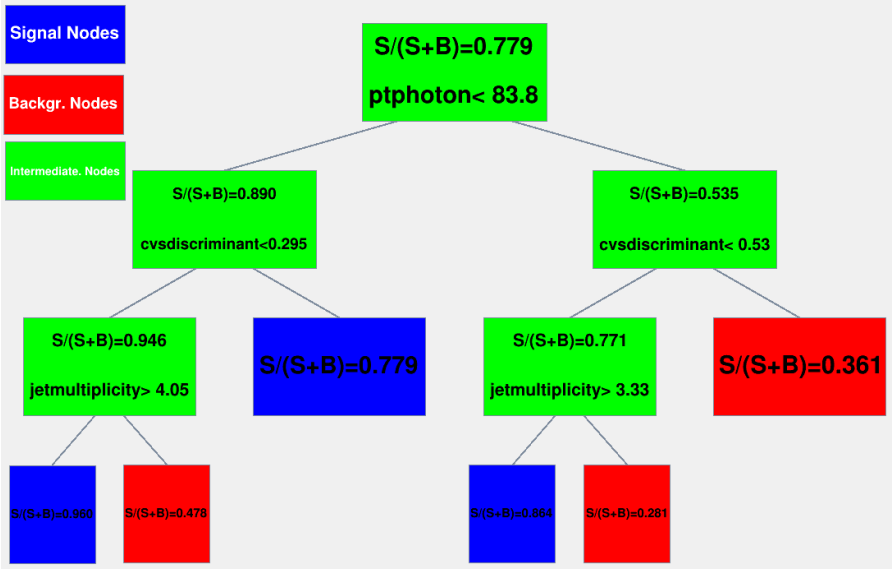

Figure 5.5: Example of a decision tree showing intermediate nodes (green) as well as signal (blue) and background (red) leaves. The variables used stem from the $tc\gamma$ data analysis. The picture was produced by TMVA.

updating event weights at each training step and combine the trees by different methods. One of the most popular boosting algorithm is the so-called AdaBoost (adaptive boost) algorithm [129].

In AdaBoost algorithm first tree is trained with the original event weights. Weights of events are modified for the next tree training and misclassified events are multiplied by a common boost weight exp(α. The factor α is derived from the fraction of misclassified training events (f) in the previous classifier as

$$\alpha = ln(\frac{1-f}{f}) \tag{5.10}$$

Total event weight is renormalized such that the sum of weights remains constant.

For each event the boosted event classification $y_{Boost}(x)$ or boosted decision output (BDT output) is then given by

$$y_{Boost}(x) = \frac{1}{M}\sum_{m}^{M} \alpha_m . b_m(x) \tag{5.11}$$

where x is a vector of the discriminating observables, M is the total number of trained trees, α_m is the boost weight of the classifier m and $b_m(x)$ is the result of an individual classifier which is $+1$ for signal and -1 for background.

5.3.2 Artificial neural networks

Artificial Neural Networks (ANN) are one of the oldest machine learning techniques used wildly in the high-energy physics and many important physics results have been extracted using this method in the last decades. ANN are layered networks of artificial neurons which recieve signal from another artificial neroun and forms an output signal. One can therefore view the neural network as a mapping from a space of input variables to an output variable in case of classification problem. In the following neural networks are briey discussed, while a comprehensive overview can be found in [130]. The ANN is used in background estimation procedure which is describe in section 5 of this thesis.

The typical architecture of a neural network is shown in figure 5.6. The input signals x_i are recieved by the first layer of neurons (processing elements). The output layer is only one neuron which is the results of the neural network. User provides the input neurons and sees the output neuron. Between the input and output layers there are a number of hidden layers which are not directly accesible to the user. Connections are between layers not within the layers and the input signal is propagated from the input layer to the output layer in an architacture called feedforward network [131]. The strength of the connection between the neuron number i and neuron number j is a variable parameter W_{ij}, called weight of the connection. These weight are adjusted to perform a variaty of mapping of input to output signal.

Each neuron performs a weighted sum of the incoming signal

$$y_j = \sum_{i=1}^{n} W_{ji} x_i \tag{5.12}$$

For many problems linear approximation is the most appropriate method which is also used in this analysis. Other linear neural network and nonlinear approximation may lead to low accurancy or lengthy computations. The neural network is trained by the known signal and background points of input variables. W_{ji} are found in a way that for a given inputs x, neural network yields a response close to 1 for signal-like events and 0 for background-like ones.

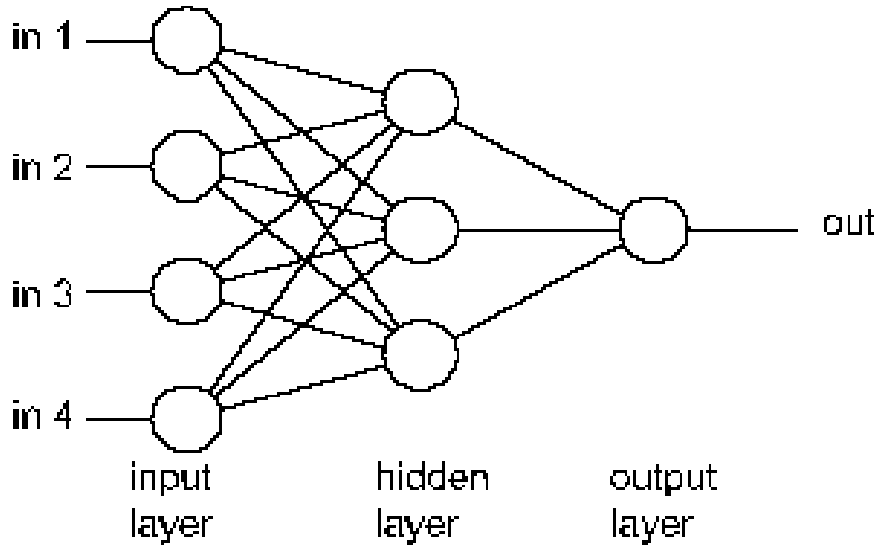

Figure 5.6: Graphical representation of the artitechture of a feed-forward neural network with four input observable, one hidden layer of three nodes and one output node.

5.4 Background estimation

After the full selection is applied, the dominant background comes from the SM $W\gamma$-jets process. It can mimic the signal if W boson decays to muon and neutrino and be associated with the heavy jets. The contribution of $W\gamma$-jets is estimated from data. On the other hand, final states contain photon suffer from non-trivial significant background arising from jet faking as photon, mostly originating from the jets in W-jets events in this analysis. Jets typically can be misidentified as photon, also called fake photon, if they fluctuate to one or two leading π^0's, which decays via $\pi^0 \to \gamma\gamma$ resulting in an electromagnetic object indistinguishable from a highly energetic photon. The probability of jet faking a photon depends on whether the jet is in the ECAL barrel or endcap, and the p_T of that jet. As the jet fragmentation models describe the jet fragmentation are not accurately known at this new energy regime, we extract the contribution of the backgrounds with jet faking photon from the data.

5.4.1 Data-driven estimation of the $W-jets$ shape

Among SM backgrounds which contribute into the defined signal region with fake photon, W-jets process has the largest cross section and is the most signal like background. Therefore, we focus on the estimation of the contribution of this important background from data and trust on the simulated events for other backgrounds in this category. We are aware that the main difference between the signal or the dominant background ($W\gamma$-jets) and W-jets process is mostly due to the origin of the selected photon which has passed our tight selection criteria. We can use this feature to find a very similar region to the signal region which is occupied by events with a photon originated from a jet.

A particular shower shape variable which measures the effective width of the photon super cluster in the η direction, denoted as $\sigma_{i\eta i\eta}$, defined in section 4.5 as

$$\sigma_{i\eta i\eta} = \sqrt{\sum_{i}^{5\times5} \omega_i(\eta_i - \bar{\eta}_{5\times5})^2 / \sum_{i}^{5\times5} \omega_i} \tag{5.13}$$

where the sum runs over the 5×5 crystal matrix around the most energetic crystal in the SC. This variable is used in photon identification to discriminate the prompt photons against photon candidates that arise from the misidentification of jet fragments. Two photons from π^0 decay produced in jet fragments lead to the wider showers in ECAL compared to one isolated prompt photon. Almost uniform distribution of fake photons for this variable is also expected. Therefore, this variable can be used to select fake photons when the cuts on $\sigma_{i\eta i\eta}$, written in table 4.2, are reversed.

In order to estimate the contribution of the W-jets process a control region, called W-jets control region, is defined using $\sigma_{i\eta i\eta}$ variable. The W-jets control region is defined similar to signal region while the photon candidates are selected by requiring the $\sigma_{i\eta i\eta} > 0.011$ and $\sigma_{i\eta i\eta} > 0.031$ in barrel and endcaps, respectively. In order to remove the contribution of $t\bar{t}$ events in W-jets control region, extra condition is applied on the number of b-jets ($N_{b-jets} = 0$).

The distributions of the $\sigma_{i\eta i\eta}$ variable in W-jets control region for data and SM backgrounds are shown in figure 5.7. The W-jets control region is enriched by the W-jets events which are shown in blue color. There are also some contaminations from the $t\bar{t}$ and Drell-Yan processes which will be considered as a source of systematic

uncertainty in the background estimation procedure. The W-jets control region is almost free from signal contribution because signal events contain a prompt photon and a b-jet. It can be seen from figure 5.7 that we can find purer control region by increasing the cut value on the $\sigma_{i\eta i\eta}$ variable. However, the statistics will decrease.

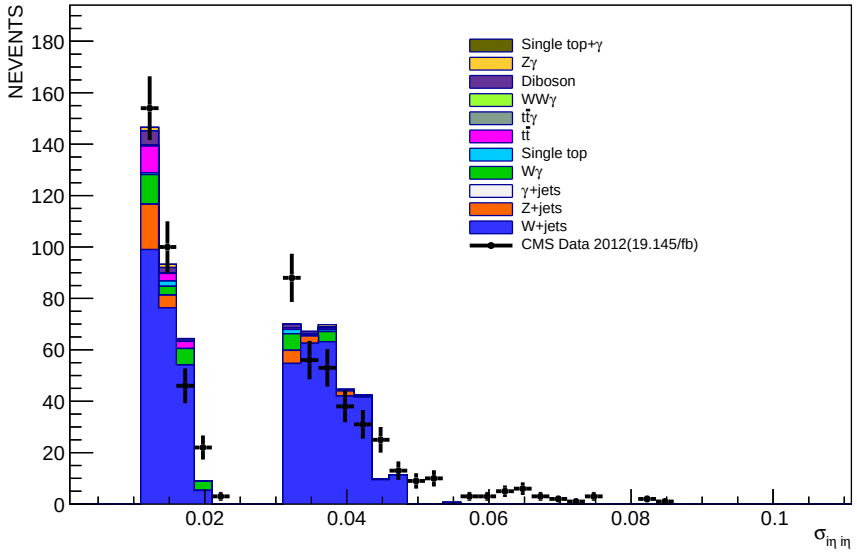

Figure 5.7: The distributions of the $\sigma_{i\eta i\eta}$ variable for SM backgrounds and data in W-jets control region.

One expects not to see different behaviour for W-jets in signal and control region for many kinematic variables because a jet is misidentified as a photon in both regions. From now on, the data events in W-jets control region will be used to estimate the W-jets shape for the distribution of a large number of variables in signal region after checking for the similar behaviour of W-jets sample in signal and control region using W-jets MC sample.

5.4.2 Data-driven estimation of the W-jets and $W\gamma$-jets normalizations

We use a template fit method to estimate the normalizations of W-jets and $W\gamma$-jets in the signal region. The idea is to divide data into three elements: W-jets, $W\gamma$-jets and other backgrounds. Then, a proper variable will be used to find the normalization of the W-jets and $W\gamma$-jets from the fit. So, data can be parametrized

as

$$F(X) = C_{W-j}S_{W-j}(X) + C_{W\gamma-j}S_{W\gamma-j}(X) + bB(X) \tag{5.14}$$

where X is an arbitrary kinematic variable. In equation 5.14, C_{W-j} and $C_{W\gamma-j}$ are the normalization of the W-jets and $W\gamma$-jets samples, respectively. These normalization factors are supposed to be determined from the fit. The total number of predicted SM backgrounds except for W-jets and $W\gamma$-jets are denoted by b which is obtained from the simulated samples normalized to the related cross sections and to an integrated luminosity of 19.76 fb^{-1} of data. The probability distribution function for the W-jets, $W\gamma$-jets and sum of the other backgrounds are given by $S_{W-j}(X)$, $S_{W\gamma-j}(X)$ and $B(X)$, respectively. These functions are obtained from

- The MC simulated sample of $W\gamma$-jets for $S_{W\gamma-j}(X)$.
- The data sample in W-jets control region for $S_{W-j}(X)$.
- The sum of the MC simulated sample of all SM backgrounds except for the W-jets and $W\gamma$-jets for $B(X)$.

In order to perform a reliable and stable template fit to estimate the unknown parameters, a variable which has different template for each element is needed. Various distribution are tried to find best variable which has the power to discriminate between the W-jets and $W\gamma$-jets events. It has been found that the cosine of the angle between two gauge bosons (γ, W) behaves differently for W-jets and $W\gamma$-jets.

Figure 5.8 shows the template of the cosine of the angle between photon and reconstructed W boson for W-jets, $W\gamma$-jets and sum of all other backgrounds in the signal region. The W boson and photon tend to be back to back in $W\gamma$-jets events while this is not the case for the W-jets process. The template of the sum of other backgrounds has an almost uniform behaviour in all range. Therefore, the fit procedure to the data can be controlled by $W\gamma$-jets in left-side and W-jets in right-side of the $\cos(\gamma, W)$ distribution.

Although the $\cos(\gamma, W)$ variable shows a reasonable discrimination power other variables are found to have almost similar power to separate events of these two backgrounds. Therefore, selected variables are combined through neural network multivariate method to reach optimum separation between W-jets, $W\gamma$-jets backgrounds. It is observed that using multivariate classification output decreases the

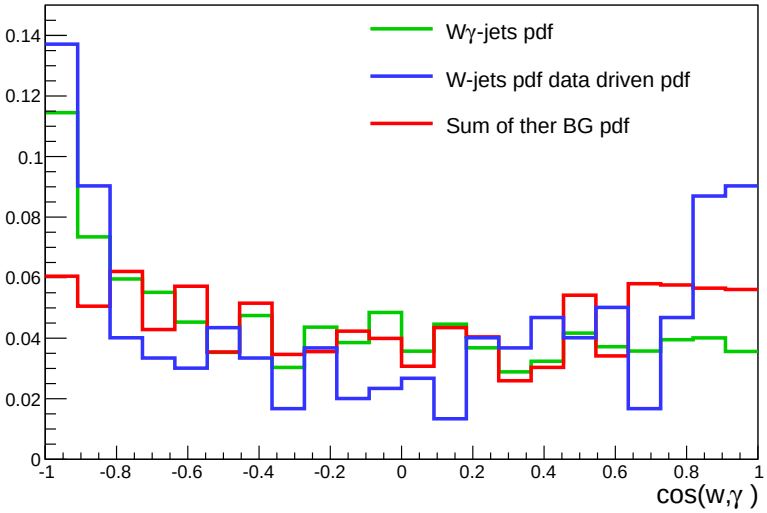

Figure 5.8: The probability distribution function of the $\cos(\gamma, W)$ variable for the W-jets, $W\gamma$-jets and sum of the other backgrounds in the signal region.

fit errors significantly and leads to more stable results with respect to the systematic uncertainty variations compared to $\cos(\gamma, W)$ variable. Neural network input variables are listed below

- $cos(W, \gamma)$: it is expected to see more back to back γ and W boson in $W\gamma$-jets events compared to W-jets events.
- transverse momentum of the selected photon: prompt photon which are generated from the first inelastic interaction are more energetic than a photon which is produced inside a jet from π^0 decay.
- transverse momentum of the selected b-jet.
- $\Delta\phi(\gamma, \text{MET})$: use the balance of the γ and W boson information in transverse plane in $W\gamma$-jets process.
- H/E of the selected photon: although fake photons could pass our tight selections they tend to show their jet characteristics in distribution of H/E variable.

As signal events are containing a prompt photon recoil against top quark, the distributions of the $\cos(\gamma, W)$ and other selected variables are very similar to the shape of the dominating $W\gamma$-jets background. In addition we know from previous experimental results that we will have small number of signal events in signal region

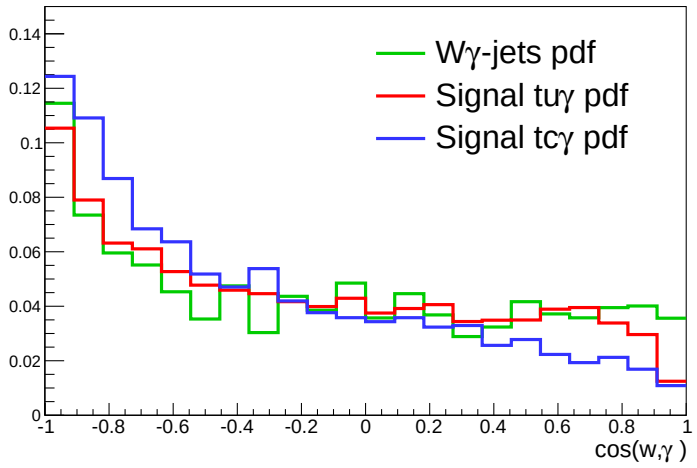

Figure 5.9: The distributions of the $\cos(\gamma, W)$ in signal region for signal and $W\gamma$-jets samples.

compared to SM backgrounds. Thus, there is no problem of contamination of signal into the fit method. The $W\gamma$-jets and signal events are fitted at the same time with the same template. The comparison of the $\cos(\gamma, W)$ distribution for signal and $W\gamma$-jets can be found on figure 5.9. Some slight differences are observed between signal events and $W\gamma$-jets events which is expected to have only a small effect on the analysis. Furthermore, a multivariate technique will be used to separate the signal events from the $W\gamma$-jets events that makes this effect negligible.

The neural network is constructed as described in the section 5.3.2. $W\gamma$-jets and W-jets simulated samples are introduced as signal and background to neural network respectively. In figure 5.10, distribution of the input variables to neural network are shown. Neural Network output for test and trained samples, ROC curve and the correlation matrices are shown in figure 5.11. It can be seen that the train and test distributions are in agreement and it is approved systematically by Kolmogorov-Smirnov test. Selected variables show no significant correlations. Neural network output in low values (neural network output < 0.4) can be used to control the W-jets contribution in data.

Before performing the fit, one should make sure that the W-jets predicts similar shape for neural network output in signal and control region using W-jets MC simulated events. Then the shape of data sample in W-jets control region can be used as $S_{W-j}(X)$ in the fit procedure. Figure 5.12 shows the distribution of neural network output for W-jets in signal region and control region while the cut on

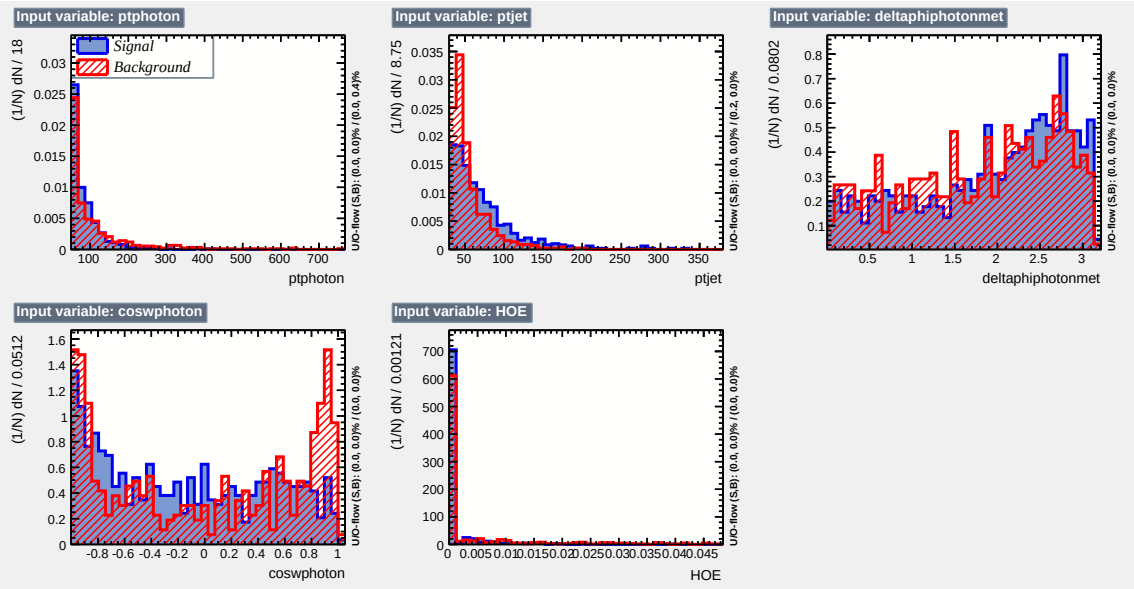

Figure 5.10: Distribution of the Neural Networks input variables for the signal ($W\gamma$-jets) and background (W-jets) simulated samples.

MET is reduced to 10 GeV and the requirement on $\Delta R(l,\gamma)$ and $\Delta R(b-jet,\gamma)$ are removed in control region to have more statistics. The shape in two regions are in good agreement within the uncertainties.

The fit is performed to extract the best values of C_{W-j}, $C_{W\gamma-j}$ using neural network output distribution for data and SM estimated backgrounds. The coefficients C_{W-j}, $C_{W\gamma-j}$ are with flat prior and b can vary 30% around the MC prediction value in the fit. The output of the fit is shown in figure 5.13. In this figure, the distributions of neural network output for data and all backgrounds are shown. The W-jets is fully estimated (both shape and normalization) from data while only the normalization of $W\gamma$-jets is based on data. The rest of backgrounds are taken from simulation. The results of the fit is reported in table 5.3.

Table 5.3: $W\gamma$-jets and W-jets predictions using data-driven (DD) and MC methods.

	DD	MC
W-jets	288.74 ± 47.17	346.38±63.69
$W\gamma$-jets	1027.45±57.48	1397.45± 97.43

Various sources of systematic uncertainties can vary the fit results. In the following we will investigate these effects.

A systematic uncertainty can be raised from the definition of the control region.

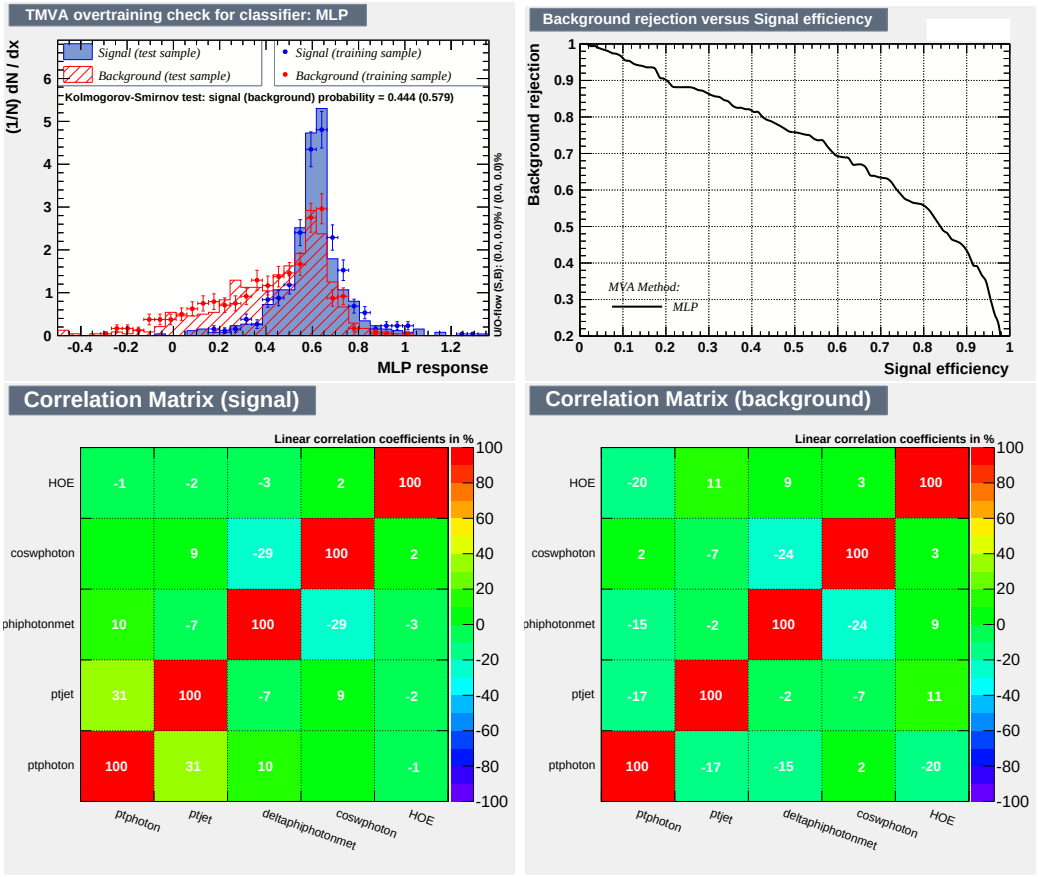

Figure 5.11: Distribution of the Neural Networks output for test and trained sample, correlation matrix and ROC curve.

As was discussed in previous section, the cut on $\sigma_{i\eta i\eta}$ can be varied to define a new control region. In order to estimate the systematic uncertainty due to definition of the control region, we vary the cut on $\sigma_{i\eta i\eta}$ by increasing the cut in two steps of 5% and 10%. It is clear from figure 5.7 that we are not allowed to increase the cut on the $\sigma_{i\eta i\eta}$ to the higher values because the remained data events are not statistically enough to perform the fit. The template fit is redone to find the fit result with the new shape for W-jets sample obtained from the new control region. The results are presented in Table 5.4. The variation of the new fit values from the nominal values, written in table 5.3, will be considered as a source of systematic uncertainties on the estimated normalizations.

The normalization of all other backgrounds except for W-jets and $W\gamma$-jets is based on the theoretically predicted cross sections by SM. In order to take into account the theoretical uncertainties on the cross sections in the background estimation procedure, all cross sections are varied by 30% and the fit is performed again

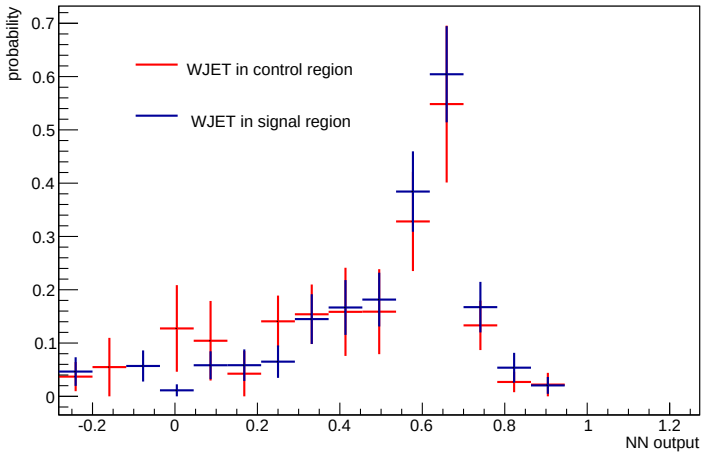

Figure 5.12: The distributions of the neural network output in signal region (blue line) and control region using W-jets MC events.

Table 5.4: W-jets and $W\gamma$-jets Data-driven (DD) predictions while the cut on $\sigma_{i\eta i\eta}$ is shifted by 5% and 10% for defining W-jets control region.

	$\sigma_{i\eta i\eta} > 0.01155(0.03255)$ for Barrel(Endcap)	$\sigma_{i\eta i\eta} > 0.0121(0.0341)$ for Barrel(Endcap)
W-jets	268.95±44.54	273.75±45.56
$W\gamma$-jets	1014.12±58.87	1008.61 ±57.90

to find the related uncertainty on the data-driven background estimation. The uncertainties obtained from the error normalization of other backgrounds on the fit results are shown in table 5.5.

Table 5.5: W-jets and $W\gamma$-jets relative variation of the data driven predictions for a variation of 30% of each background.

	$t\bar{t}$	single top	Dibosons	$Z\gamma$-jets	$Z/\gamma(\rightarrow l^+l^-)$-jets
W-jets	$< 3\%$	$< 2\%$	$< 1\%$	$< 4\%$	$< 1\%$
$W\gamma$-jets	$< 2\%$	$< 1\%$	$< 1\%$	$< 1\%$	$< 4\%$

It was discussed that our control region is enriched by W-jets events but there are few contributions of other backgrounds. In order to estimate this effect, the contribution of other backgrounds are subtracted from data in W-jets control region and the fit is redone. A new shape for W-jets is obtained when the contribution of other backgrounds is subtracted from data in W-jets control region. The effect is less than 7% for both W-jets and $W\gamma$-jets estimated number of events. It is clear that this source of error is not significant and our control region is almost pure.

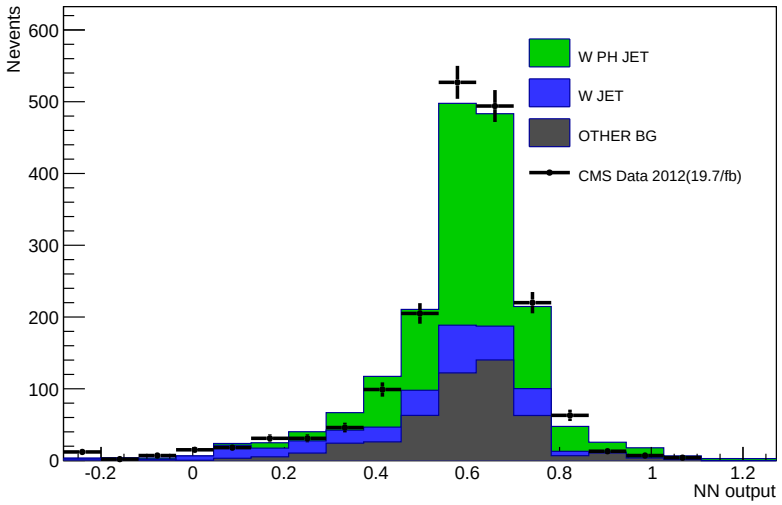

Figure 5.13: The distributions of the neural network output for SM backgrounds and data while the fit results are included.

5.4.3 Data-driven estimation of the $W\gamma$-jets shape

The contribution of the $W\gamma$-jets is estimated from data as was discussed in previous section. In order to distinguish signal events from this important background, we also need to know the shape of that for some variables accurately. Therefore, it is essential to find them directly from data.

In order to estimate the $W\gamma$-jets shape for an arbitrary variable in signal region, we rely on the fact that the kinematics of the $W\gamma$-jets events are independent of the top quark mass. Because the reconstructed W boson and selected b-jet are not the decay products of the top quark in $W\gamma$-jets sample. Therefore, one expects to see similar behaviour inside and outside of top mass window. A side band-region is defined similar to the signal region while the top mass window requirement is changed from inside to outside ($m_{top} > 220$ and $m_{top} < 130$). The side-band region is a control region for $W\gamma$-jets samples.

The distribution of top mass quark is shown in figure 5.4. Although a small fraction of signal events are in side-band region SM processes have huge contribution in this region. In the side-band region, we rely on MC prediction for all backgrounds except for W-jets. In this region, we subtract the contribution of all backgrounds from data for an arbitrary variable to obtain the $W\gamma$-jets shape. To obtain the shape of W-jets from data in the side-band region, we use the data events in side

band while the cut on variable $\sigma_{i\eta i\eta}$ is reversed as well as requiring no b-tagged jet (W-jet control region, see section 5.4.1). The number of W-jets events in the side-band is normalized due to its data driven values in signal region using the following equation:

$$N_{out} = N_{in} \times \frac{\alpha_{out}}{\alpha_{in}} \tag{5.15}$$

where N_{out} is the number of the W-jets events in the side-band and N_{in} is the number of the W-jets events in the top mass window which has been estimated from the template fit. The parameters α_{in} is the fraction of the W-jets events in the top mass window and $\alpha_{out} = 1 - \alpha_{in}$ which are taken from data in W-jets control region.

5.4.4 Other backgrounds

The $W\gamma$-jets and W-jets backgrounds described above are the major backgrounds for the signal processes considered in this dissertation. Some background categories are not included in these data-driven estimations. These backgrounds contribute only a small number of events after the final selections or can be described well by MC simulation. The shape and normalization of all SM backgrounds except for $W\gamma$-jets and W-jets are estimated from simulation.

5.5 Event weights and DATA/MC comparison

In order to achieve a better agreement between the SM prediction from simulated events and measured data, several types of weights need to be applied on the MC events. In this section different event weights that have to be used in this analysis will be presented. Finally, the measured data is compared to the MC prediction.

5.5.1 Cross section

The number of events in a generated sample is independent of the event rate of a certain process in measured data. However, more events are needed for high rate processes to find the behaviour of that process accurately. Therefore, each event in MC sample should be weighted due to the expected rate in the integrated luminosity of the dataset used. The weight is calculated as

$$\omega = \frac{\sigma \times \mathcal{L}}{\text{number of generated events}} \tag{5.16}$$

where σ is the cross section of the related process and $\mathcal{L}$ is the total integrated luminosity.

5.5.2 Pileup reweighting

As already stated in chapter 4, multiple proton interactions happen during one bunch crossing and additional particles are produced that are not related to the one single interaction we want to study. In order to account for the pileup noise, CMS generated MC events with a specific pileup distribution model for 8 TeV simulated samples. Although the CMS pileup condition is modelled appropriately it needs to be corrected due to the real data situation. In figure 5.14, the number of pile-up interactions in data and simulation are compared.

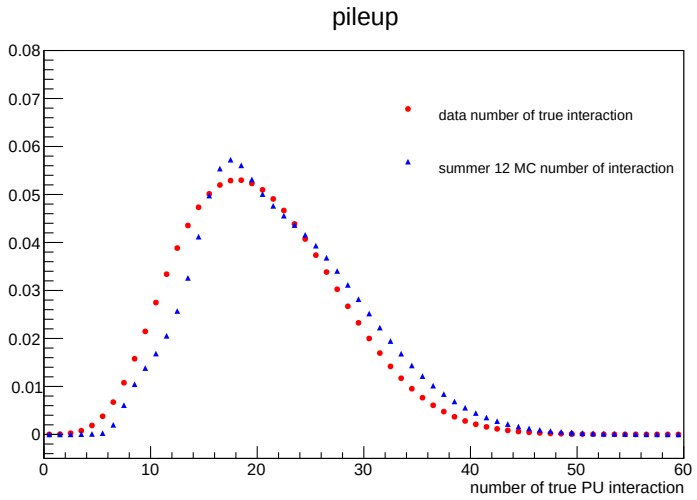

Figure 5.14: he distribution of true pile up interactions for data and MC. (The MC distribution refers to the "PU-S10")

Therefore, the measured pileup distribution in the used data sample is divided to the known MC pileup distribution to find the pileup scale factor as a function of the pileup numbers. Then each event in MC is weighted by this function according to the number of pile-up interactions for that event.

5.5.3 B-tag discriminator reshaping

The correction factors applied to the simulation for b-tagging and mis-tagging efficiencies need to be accounted for. As described in section 4.9, we used the CSV algorithm with the medium working point to tag the b-jets candidates. Events contain more than one b-jets are discarded to suppress multi b-jet background events. It will be seen in the next section that the b-tag discriminator distribution is also an important variable to suppress the zero b-jet background events.

Therefore, we need to correct the CSV discriminant not only for the medium working point but also for the whole range of CSV discriminant. In order to correct the MC CSV discriminant due to the measured data, the CSV discriminant value in MC is found in such a way that the MC efficiency is equal to the efficiency measured in data. The MC efficiency is calculated as

$$\epsilon_{MC}^{ij} = \frac{\text{Number of type i jets with CSV discriminant} > \text{Working point j}}{\text{Total number of type i jets}} \quad (5.17)$$

Where i accounts for different type of the jets (light jet, c-jet and b-jet) and j accounts for three working points (loose, medium and tight).

This procedure is performed to find the ϵ_{MC} for nine points. For each working point, points in neighbourhood are search to find a point which has similar efficiency which is measured in data. these points are are selected as a modified working points in MC. In addition to these points, two extra fix points are considered when CSV discriminant is 0 and 1. In these two fix points, CSV value is assumed to be equal for data and MC. The original and modified points are shown in figure 5.15. The b-tag, c-tag and miss-tag efficiencies in measured data are accompanied with uncertainties which leads to uncertainty bands in modified MC CSV. The uncertainty bands are shown with dash line in figure 5.15.

When the modified values of CSV discriminant is found in MC for three points based on data. Then, one can interpolate to find the correct value of CSV discriminant for any other arbitrary point. The CSV discriminator before and after the correction is presented in Fig.5.16.

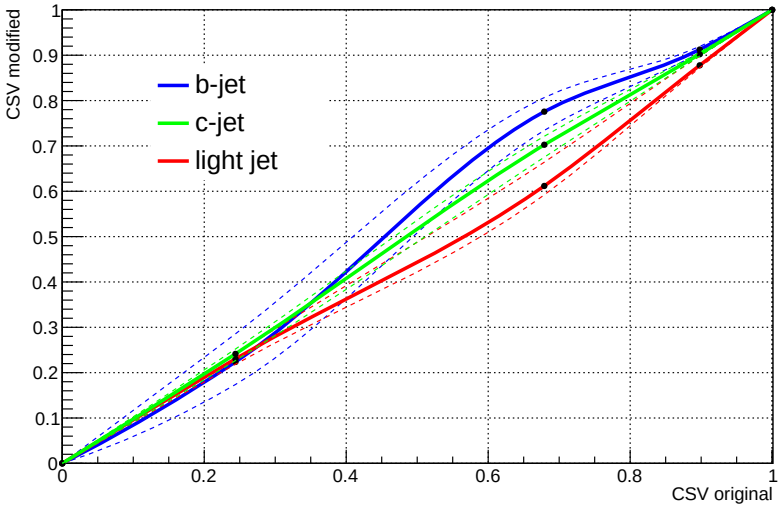

Figure 5.15: the CSV modified points vs the original (uncorrected) points. the dashed lines illustrate the uncertainty bands.

5.5.4 Other weights and correction factors

More scale factors are associated to the selected events in simulation to keep into account further differences between data and MC.

The calculated muon momentum in both data and MC shows different biases originating from residual magnetic fields and misalignment. The muon transverse momentum (curvature) corrections are extracted from $Z \to \mu\mu$. The muon scale factor is applied as function of η and p_T as an weight in each event.

The width and peak position of the Z boson is exploited to measure photon energy resolution and determine the absolute photon energy scale using the data itself. The $Z \to \mu\mu\gamma$ process is a clean source of high energy photons in the hadron collider environment. To estimate the true scale and resolution in the simulation, the energy responses in $Z \to \mu\mu\gamma$ sample is employed. The extracted photon energy scale in data and simulation is applied on simulation as a function of photon transverse energy.

The performance of single lepton trigger is measured using a data driven method called tag and probe [132]. This method is used to measure the lepton efficiency in data and in simulation, and used to determine a scale factor to correct the simulation for any data/MC difference in efficiency. The single muon trigger efficiency is measured using muons from Z-boson decay. The measured trigger scale factor is

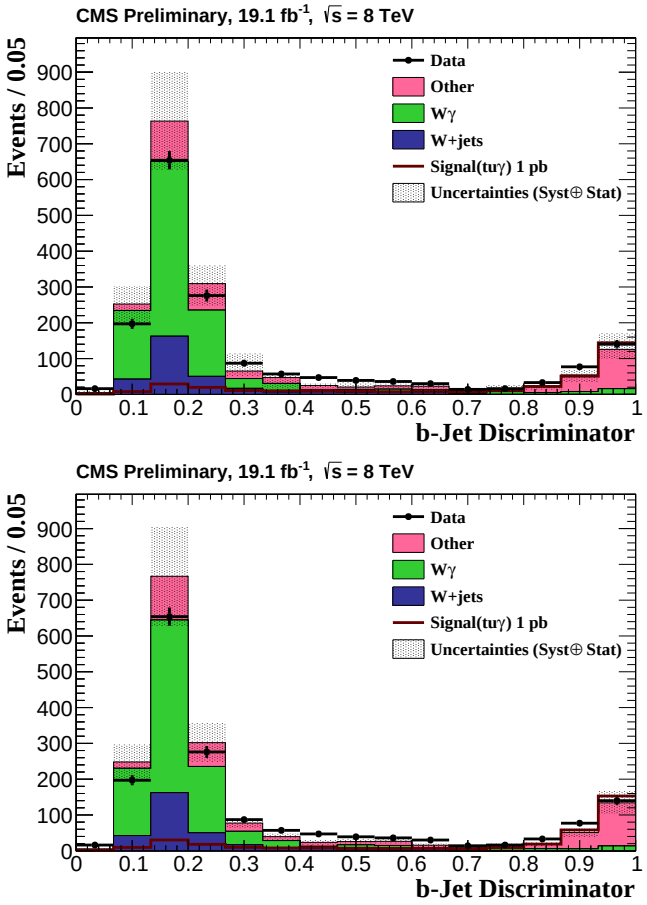

Figure 5.16: The distributions of the CSV discriminator before (top) and after (bottom) b-tag Discriminator Re-shaping. The $W\gamma$-jets and W-jets backgrounds are driven from data and the reshaping effects are just applied to the MC simulated events. The error bands include both systematic and statistical uncertainties.

applied as a function of muon η in this analysis.

5.5.5 DATA/MC comparison

After taking into account all the related scale factors, the event yields can be seen on table 5.6 (uncertainties are statistical only). At the last column which is related to top mass window cut, there is a good agreement between the SM prediction and observed data after doing the fit.

DATA/MC agreement can also be checked in the distribution of different kinematic variables. In figures 5.17 and 5.18 the distribution of the photon, muon and b-jet for p_T and η variables are shown. In all plots there is a good agreement between measured data and MC prediction prediction. The signal distribution is

Table 5.6: Events yield and signal efficiency after the different steps of the event selection. Uncertainty is statistical only.

	lepton and photon selection	MET cut	jet and b-jet multi ΔR cuts	top mass cut (post-fit)
single top	102.06 ± 6.71	81.56 ± 6.03	50.70 ± 4.73	26.26 ± 3.42
single top+γ	81.18 ± 6.11	59.90 ± 4.88	49.85 ± 4.66	30.25 ± 2.65
$t\bar{t}$	733.44 ± 22.26	613.15 ± 20.37	329.35 ± 15.04	152.74 ± 10.28
$t\bar{t}\gamma$	172.08 ± 8.33	144.68 ± 7.58	76.60 ± 5.48	33.48 ± 3.59
$Z/\gamma(\rightarrow l^+l^-)$-jets	1382.92 ± 52.83	382.03 ± 26.88	227.69 ± 21.00	64.77 ± 10.78
W-jets	2219.34 ± 169.12	1681.2 ± 149.29	896.56 ± 106.44	288.74 ± 47.17
γ-jets	39.58 ± 33.35	6.81 ± 6.22	6.81 ± 6.22	0
$Z\gamma$-jets	1979.32 ± 39.97	585.65 ± 21.23	484.79 ± 19.87	137.31 ± 8.68
$W\gamma$-jets	7979.47 ± 216.95	5670.76 ± 192.07	4682.28 ± 174.97	1027.45 ± 57.48
Dibosons	237.78 ± 4.83	169.9 ± 4.13	121.91 ± 3.54	37.46 ± 1.99
$WW\gamma$	37.61 ± 1.22	30.21 ± 1.02	23.83 ± 0.90	6.86 ± 0.48
$\epsilon_{sig}^{t\gamma u}(\%)$	5.03	4.48	4.19	1.86
$\epsilon_{sig}^{t\gamma c}(\%)$	5.96	5.10	4.65	2.42
Total Backgrounds	14964.8 ± 286.09	9425.97 ± 246.86	6950.43 ± 207.68	1805.44 ± 76.56
DATA	11410 ± 106.81	7048 ± 83.95	5315 ± 72.90	1794 ± 42.35

shown with red line in all the histograms. It is clear that the photon p_T is a very good discriminant between SM processes and signal events.

In figures 5.19 and 5.20, distributions of jet multiplicity, b-tag discriminant, $\cos(\gamma, W)$, $\Delta R(\gamma, b-jet)$, $\Delta R(\gamma, \mu)$ and $\cos(top, \gamma)$ are shown. Among these variables, b-tag discriminant shows a very good discriminating power between signal and background events. Figure 5.21 shows the charge distribution of the selected muon in data, SM backgrounds and signal. As was discuses in section 2.6, one of the important features of $tu\gamma$ signal channel is an asymmetry between top and anti-top production rates which can make the anomalous production of top quark more sensitive to find the couplings characteristics compared to anomalous top decays. This feature will be employed to discriminate signal from backgrounds in the following sections.

5.6 Signal extraction

The agreement between the SM prediction and measured data was tested in both number of events and shape of several variables. Although some variables present a reasonable separation between signal and background events better separation power can be achieved by combining these variables. In this section a multivariate technique is employed to find the signal excess clearly.

5.6.1 Training of BDT

In order to perform the MVA in this analysis a Boosted Decision Tree (BDT) is trained using the TMVA framework. The BDT is trained for $tu\gamma$ and $tc\gamma$ signal channels separately using $W\gamma$-jets, $t\bar{t}$ and di-bosons simulated background events. The following variables are chosen as input variables for $tu\gamma$ and $tc\gamma$ BDT training.

- photon transverse momentum,
- b-jet transverse momentum,
- muon transverse momentum (only for $tc\gamma$),
- angular separation between the photon and the muon ($\Delta R(\mu, \gamma)$),
- angular separation between the photon and the b-jet ($\Delta R(b-jet, \gamma)$),

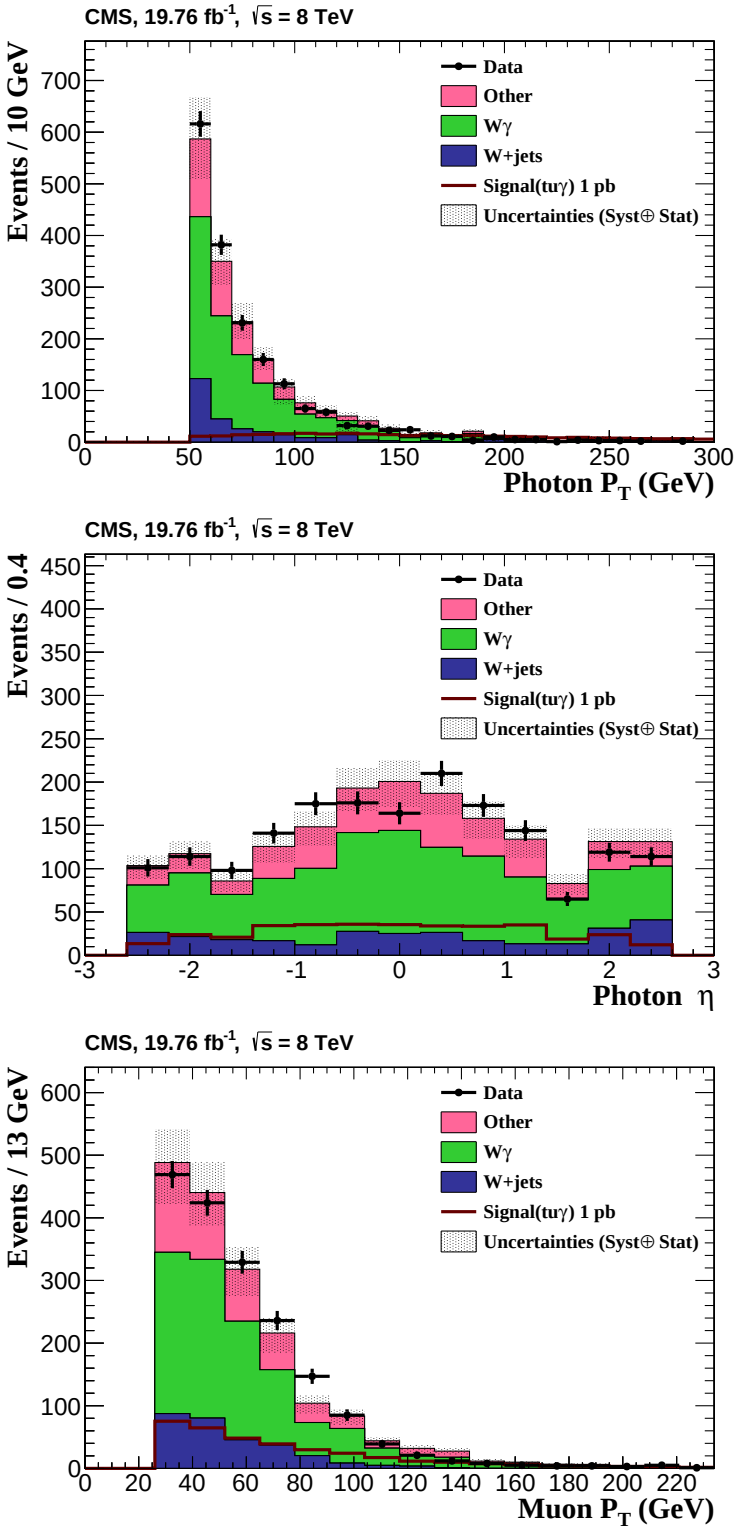

Figure 5.17: Distributions of the transverse momenta of photon (top), pseudorapidity of photon (middle) and transverse momenta of muon (bottom) after the selection cuts for data, backgrounds and signal. The W-jets and $W\gamma$-jets contributions are estimated from data. The $tu\gamma$ signal sample is normalized to a cross section of 1 pb. The error bands contain both systematics and statistical uncertainties.

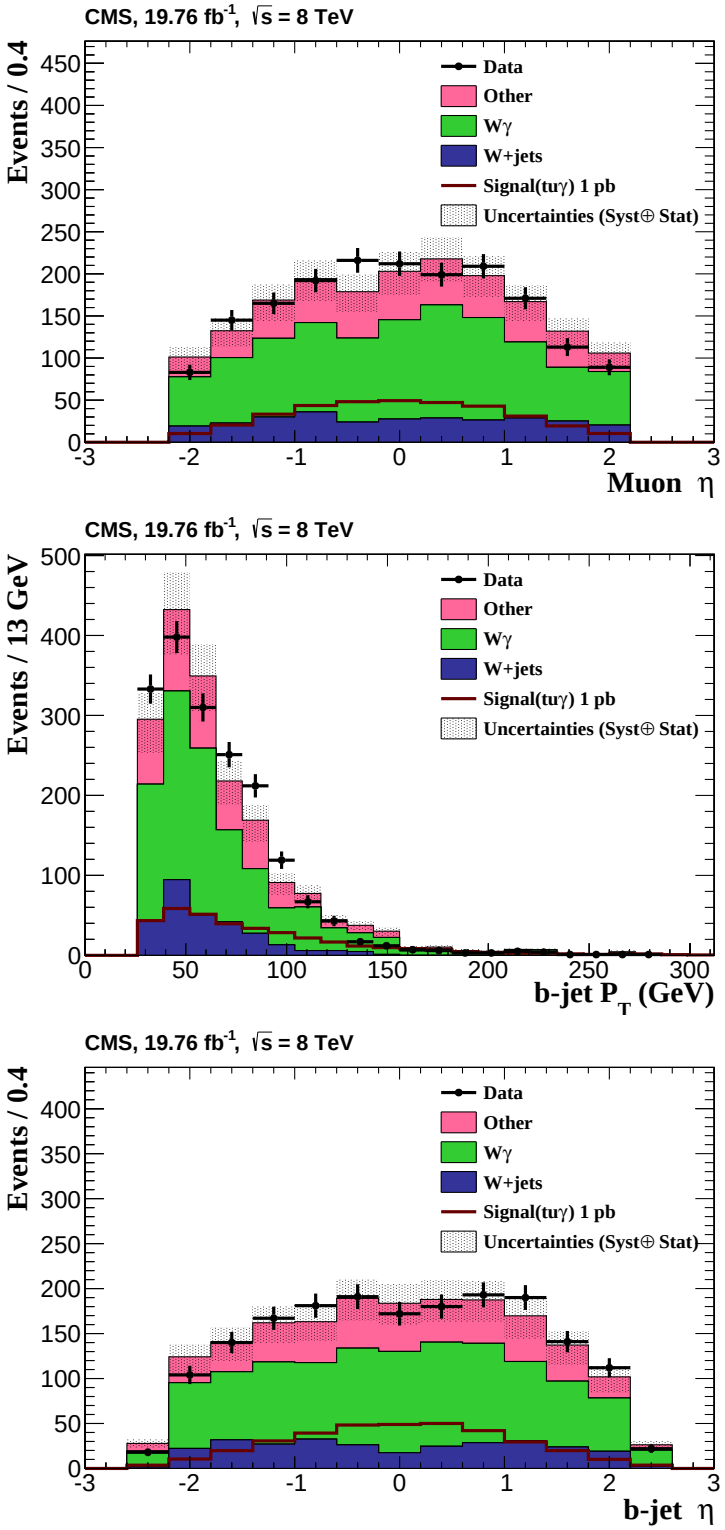

Figure 5.18: Distributions of the pseudorapidity of muon (top), transverse momenta of b-jet (middle) and pseudorapidity of b-jet (bottom) after the selection cuts for data, backgrounds and signal. The W-jets and $W\gamma$-jets contributions are estimated from data. The $tu\gamma$ signal sample is normalized to a cross section of 1 pb. The error bands contain both systematics and statistical uncertainties.

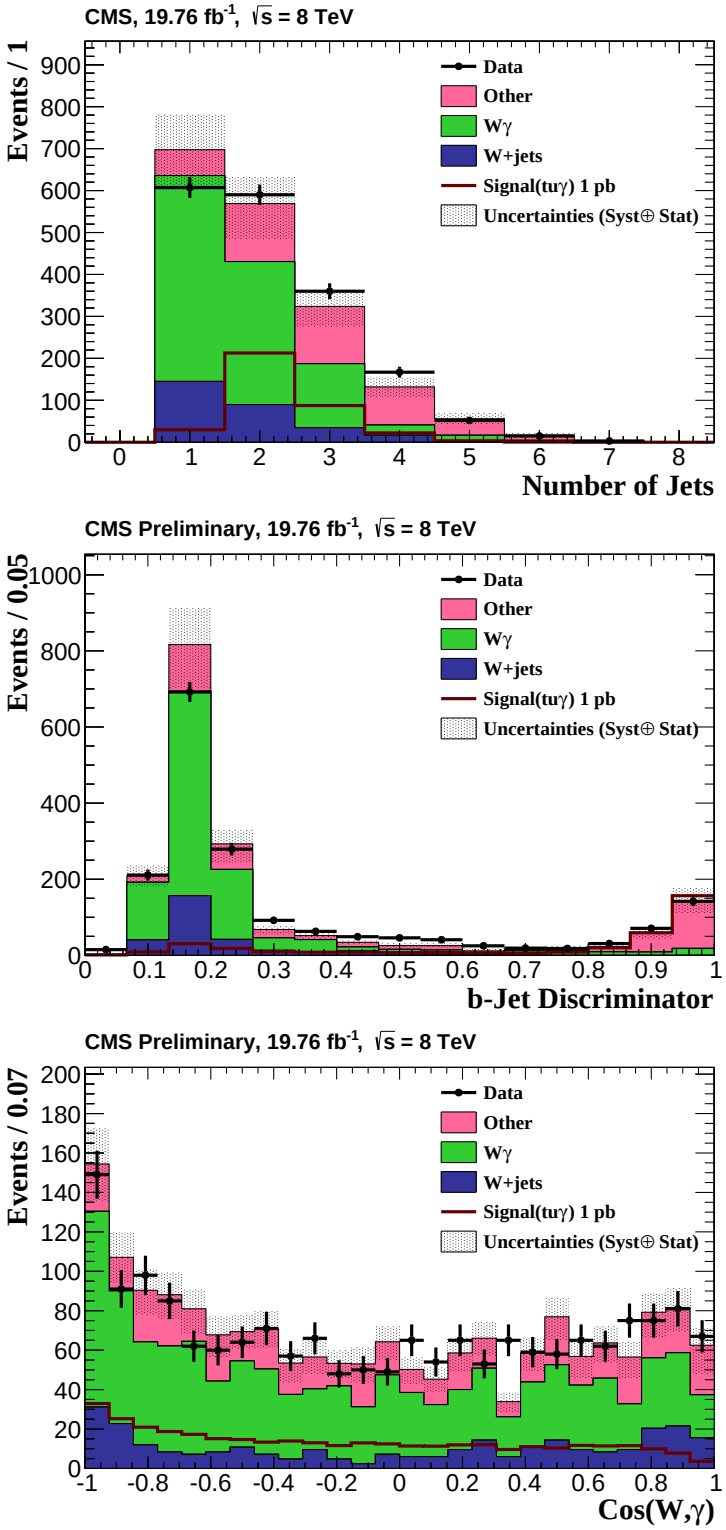

Figure 5.19: Distributions of the jet multiplicity (top), CSV discriminant (middle) and $\cos(\gamma, W)$ (bottom) after the selection cuts for data, backgrounds and signal. The W-jets and $W\gamma$-jets contributions are estimated from data. The $tu\gamma$ signal sample is normalized to a cross section of 1 pb. The error bands contain both systematics and statistical uncertainties.

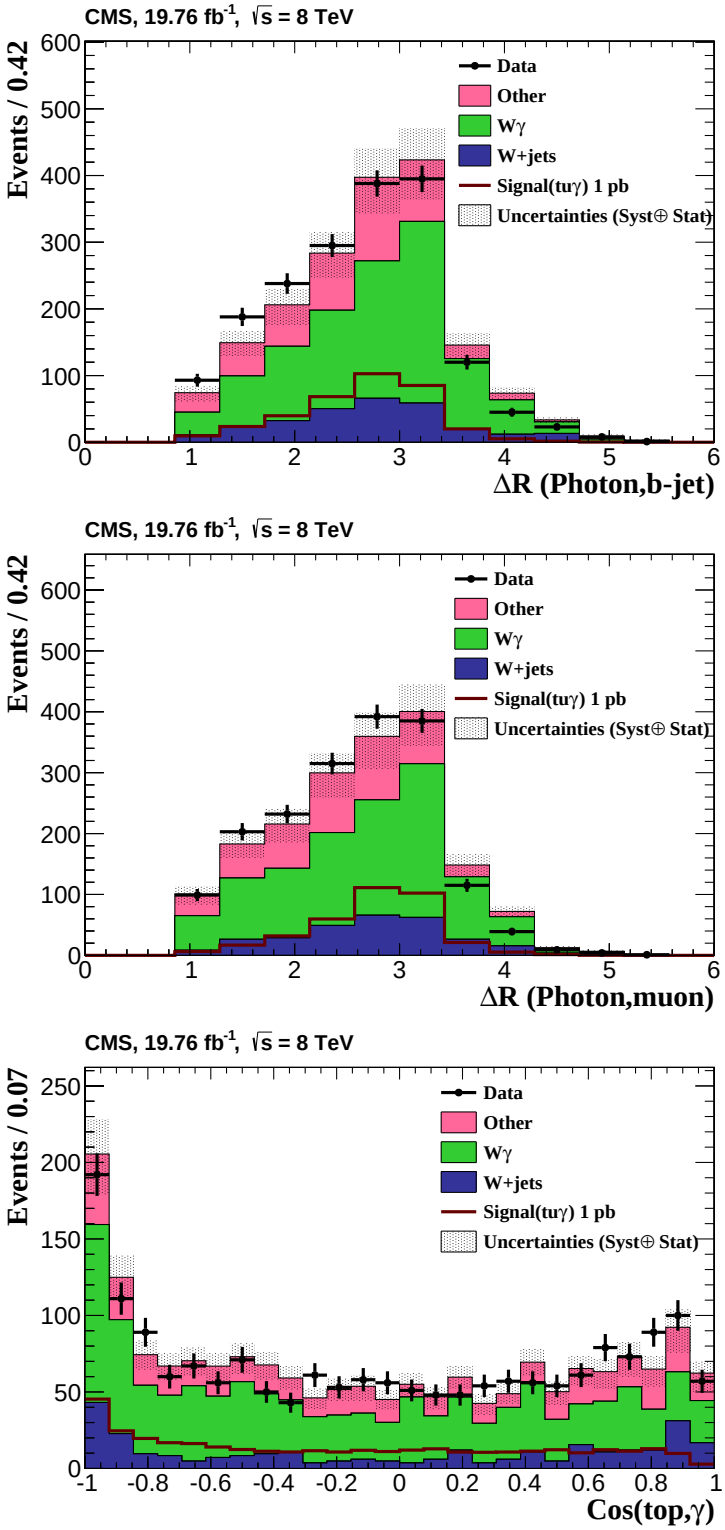

Figure 5.20: Distributions of the $\Delta R(\gamma, b-jet)$ (top), $\Delta R(\gamma, \mu)$ (middle) and $\cos(top, \gamma)$ (bottom) after the selection cuts for data, backgrounds and signal. The W-jets and $W\gamma$-jets contributions are estimated from data. The $tu\gamma$ signal sample is normalized to a cross section of 1 pb. The error bands contain both systematics and statistical uncertainties.

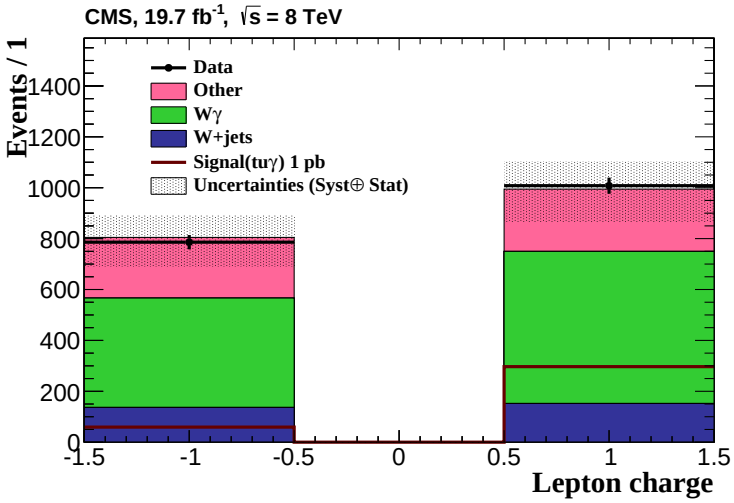

Figure 5.21: Distributions of the muon charge after the selection cuts for data, backgrounds and signal. The W-jets and $W\gamma$-jets contributions are estimated from data. The $tu\gamma$ signal sample is normalized to a cross section of 1 pb. The error bands contain both systematics and statistical uncertainties.

- CSV discriminant value for the b-tagged jet,
- jet multiplicity,
- cosine of the angle between the reconstructed top quark and the photon,
- muon charge (only for $tu\gamma$),

Photon, muon and b-jet properties are distinctive features of signal events in this analysis. CSV discriminant nicely separates SM processes with one b-jet from those with no b-jet. Although ΔR cuts between photon, b-jet and muon are applied in pre-selection, these objects tend to be closer to each other in some SM processes. Jet multiplicity can distinguish between multi-jet SM processes like $t\bar{t}$ and signal. Finally, the cosine of the angle between the reconstructed top quark and the photon contains many properties of the signal events. The variables with the most discriminating power are photon p_T and CSV discriminator.

Distribution of the BDT input variables are shown in figure 5.22 and 5.23. Correlation coefficients between all variables are shown in figure 5.24 for signal and background samples and both signal channel. Selected variables are mostly decorrelated. Nevertheless, TMVA provides decorrelation tools to deal with correlated variables.

Input variables can contribute many times in construction of trees while some of

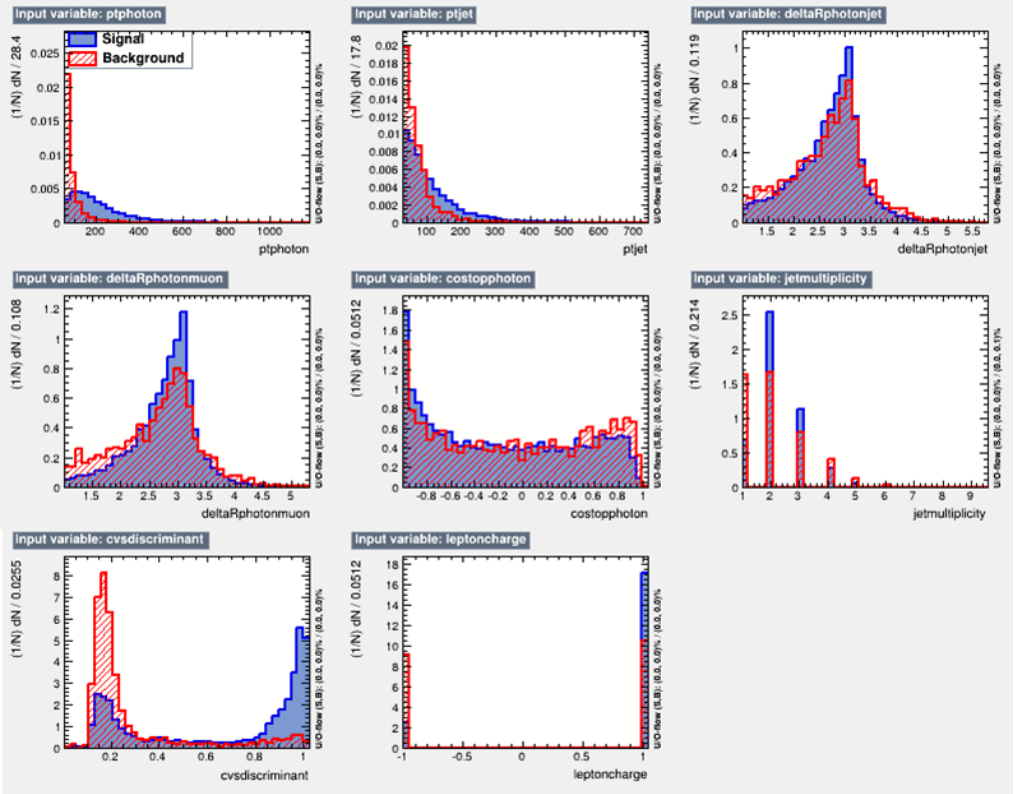

Figure 5.22: The distributions of the BDT input variables for tγu signal channel, Blue is the signal and red is the combined background.

them are used more because they can separate signal events with high signal selection efficiency and high background rejection efficiency. Therefore, TMVA provide the importance variable list which shows how important a variable contributed to BDT compared to other variables. Table 5.7 shows the variable importance for tγu and tγc signal channel. As was expected transverse momentum of the selected photon and CSV discriminant value of the selected b-jet play important roles in BDT training.

5.6.2 BDT output

The final BDT output is a single discriminant ranging from -1 to +1, discussed earlier in equation 5.11. Events with higher (lower) BDT output values are signal-like (background like) events. Therefore, one expects to see signal events gathered close to +1 while background events be close to -1. As was discussed in section 5.3, a statistically independent MC sample should be used to test the BDT training. In figure 5.25, the BDT output distribution for test and train samples are shown for both signal channels. There is good agreement between the BDT output distribution

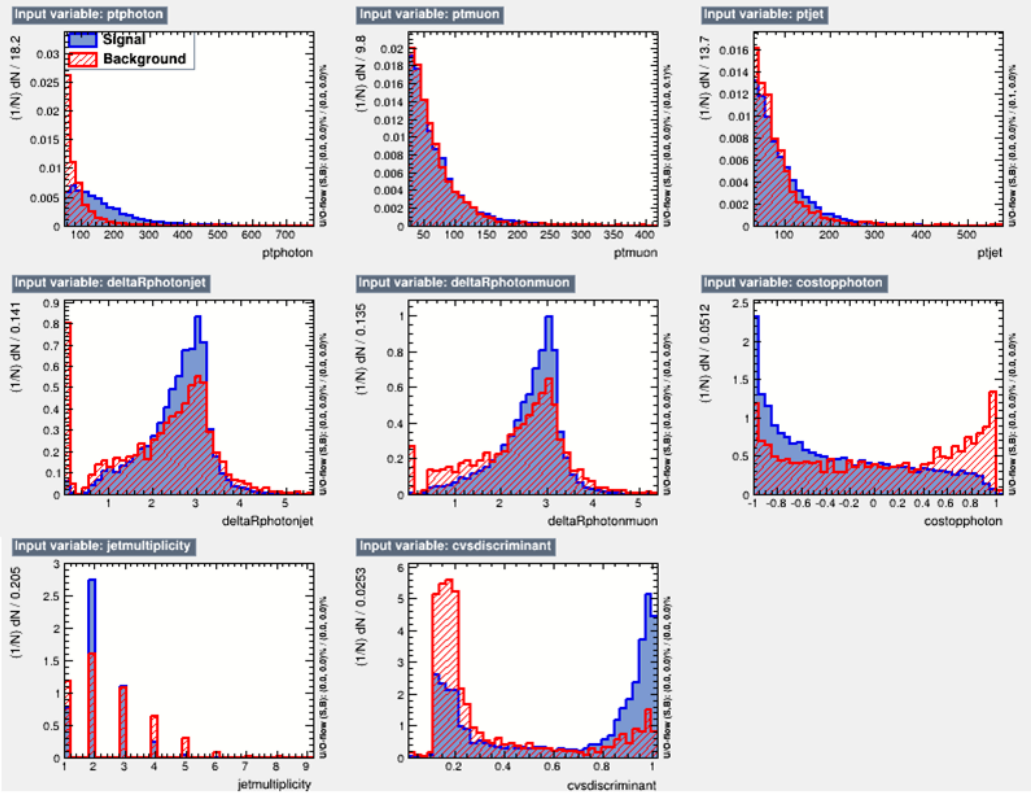

Figure 5.23: The distributions of the BDT input variables for tγc signal channel, Blue is the signal and red is the combined background.

of test and train samples which indicate that the BDT is safe from overtraining. It can also be seen in the Kolmogorov-Smirnov test values for signal and backgrounds which compare the distributions in the training and testing samples numerically.

Quality of training can be found from ROC curve showing the signal efficiency versus background rejection efficiencies, see figure 5.26. Single top and photon in $tu\gamma$ signal channel are produced from the interaction of a valence quark and gluon which leads to more energetic objects in final state. This feature makes $tu\gamma$ training more efficient than $tc\gamma$ training. Therefore, BDT training is more efficient against backgrounds for $tu\gamma$ signal channel compared to $tc\gamma$ signal channel which is illustrated in ROC curves.

5.7 Systematic uncertainties

Numerous sources of systematic uncertainties are associated with both the background estimations and the simulation of the signals. There are three types of systematic effects considered in this analysis: those that affect only the rates of

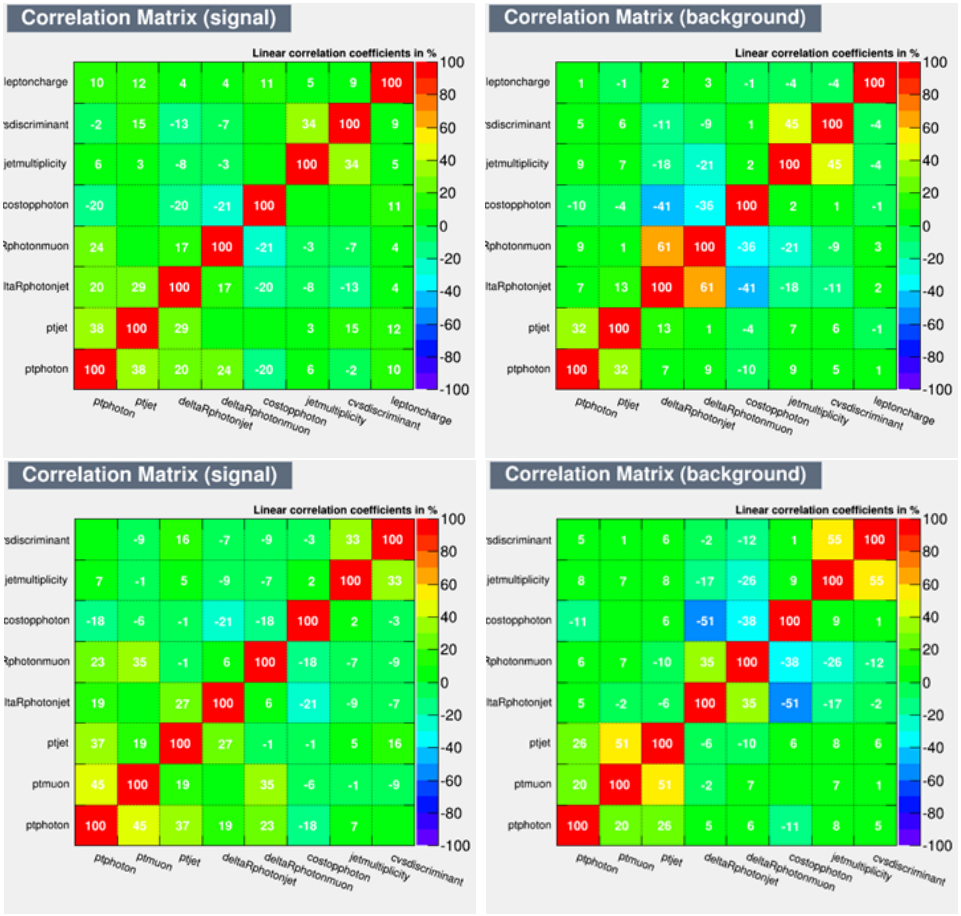

Figure 5.24: The correlation matrices for tγu channel for signal (top-left) and background (top-right) variables. The correlation matrices is also shown for tγc channel for signal (bottom-left) and background (bottom-right) variables.

signal or background processes, those that affect only the shapes of the BDT discriminants for signal or background processes, and those that affect both the rate and the shape. In the last case, the rate and shape effects are treated simultaneously so that they are considered completely correlated. Below is a list of systematic effects considered for this analysis:

- **Luminosity:** The overall uncertainty on the integrated luminosity of the data used in the analysis is estimated based on the cluster counting from the silicon pixel detector [133]. A value of 2.6% error is considered on the signal and background rates except for the backgrounds estimated with data-driven method.

- **Pileup re-weighting:** The systematic uncertainty due to Pileup re-weighting is determined by varying the minimum-bias cross section used to calculate the

Table 5.7: The BDT input variables according to their importance separately for $tu\gamma$ and $tc\gamma$.

variable name	variable importance ($tu\gamma$)	variable importance ($tc\gamma$)
Photon p_T	0.185	0.187
CSV disc	0.179	0.156
p_T of muon	-	0.114
$\Delta R(\mu, \gamma)$	0.094	0.151
p_T of bjet	0.136	0.108
Jet Multiplicity	0.081	0.120
$\cos(top, \gamma)$	0.125	0.074
$\Delta R(bjet, \gamma)$	0.104	0.087
Muon charge	0.093	-

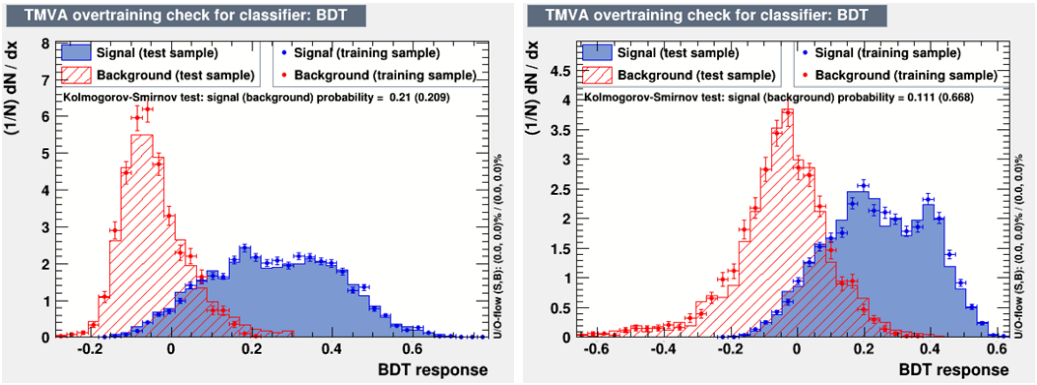

Figure 5.25: The BDT output distribution for overtraining check fot tγu (left) and tγc (right).

pileup re-weighting by 5% from the default value of 69.3 mb. New pileup weights are applied to determine the uncertainty on both the rate and shapes [134].

- **Muon, photon and trigger scale factors:** The scale factors used to take into account the muon, photon and trigger efficiencies differences between measured data and simulation are varied up and down by their statistical and systematic uncertainties [135, 136]. These variations are small and vary the shape and rates of the signal and background processes slightly.

- **Photon Energy Scale:** The uncertainty on the nominal photon energy scale is considered to be 1% in barrel and 3% in endcap [136]. This uncertainty can vary both the shape and rate of background and signal processes. However, the effects on shape is more significant because photon p_T is the most important

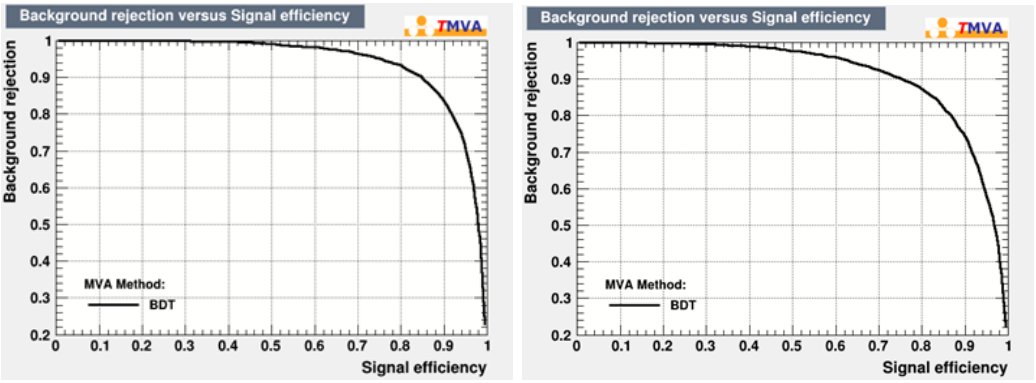

Figure 5.26: ROC-Curve, i.e. signal efficiency versus background rejection plot fot tγu (left) and tγc (right).

variable in BDT training.

- **Jet Energy Scale:** The uncertainty on the jet energy scale (JES) is evaluated by shifting the jet energy scale applied to the reconstructed jets up and down by one standard deviation. E_T^{miss} is recalculated due to the variation of the jet energy scale [137].

- **Jet Energy Resolution:** The uncertainty on jet energy resolution (JER) is taken into account by smearing the jets energies according to the known difference in JER w.r.t data [114]. The effect of JER is carried over to the calculation of the E_T^{miss} in the event.

- **B-tagging:** As was discussed in section 5.5.3, the b-tag reshaping procedure is accompanied with uncertainty bands for b-jet, c-jet and light jets. These uncertainties are taken into account by varying the b-discriminant values of the simulated jets using modified up and down curved shown in figure 5.15.

- **Cross Sections:** The expectation for some of the background processes yields are derived from theoretical predictions. Uncertainties affecting these normalizations are taken to be 30% conservatively.

- **Background estimations:** As discussed in Section 5.4.2, different source of uncertainties have influence on the results of the the fit. These errors are considered on the normalizations of W-jets and $W\gamma$-jets processes. The uncertainties on the data driven background rates are calculated to be 17% and 23% on the $W\gamma$-jets and W-jets rates, respectively.

- **Uncertainty due to PDF:** The systematic uncertainty originating from the proton parton distribution functions on the cross section of signal is estimated using the PDF4LHC recommendation [138]. In this method the cross section of $t\gamma$ production due to the anomalous $tu\gamma$ and $tc\gamma$ interaction is calculated by the 22 eigenvalues of the CTEQ PDF sets as a function of photon p_T. Table 5.8 shows PDF error in different photon p_T bins which can change both shape and rate of the BDT output of signal distribution.

Table 5.8: PDF uncertainty as a function if the photon p_T for the signal sample.

P_T^γ	$[50-100]$	$[100-150]$	$[150-200]$	$[200-250]$	$[250-300]$	$[300-350]$
PDF Unc.	0.011	0.014	0.027	0.028	0.031	0.044
P_T^γ	$[350-400]$	$[400-450]$	$[45-500]$	$[500-550]$	$[600-650]$	>650
PDF Unc.	0.048	0.051	0.063	0.068	0.075	0.078

- **Signal NLO corrections:** In section 5.1.1, the NLO k-factor is given as a function of photon p_T. An uncertainty of 5% is assumed on the reported k-factors in [119].

- **Renormalization/Factorization scale:** Two different signal samples are produced with the Q-scale multiplied and divided by a factor of two to estimate the effect of Q-scale variation. Then the differences between the the output of varied samples and the nominal sample enable us to estimate this systematics.

- **Top quark mass:** To estimate this uncertainty, two new samples for the signal are produced with the top mass shifted by 2 GeV from the nominal value of 172.5 GeV. Then the differences between the varied and the nominal samples provide the uncertainty from top mass.

All systematic uncertainties discussed above are accounted for in the limit calculation via nuisance parameters which are discussed in section 5.8. It is worth mentioning again that among the systematic uncertainties, the luminosity uncertainties only affect the normalization while the uncertainties from the pileup, trigger and lepton and photon selection efficiencies, b tagging, and jet energy scale and resolution affect also the shape of the output of the BDT discriminant of signal or background. The PDF, renormalization and factorization scales, and top quark mass uncertainties affect both the shape and the normalization of the BDT discriminant of signal.

Table 5.9: Relative variation of the expected cross-section limit obtained when omitting the nuisance parameter associated to a certain systematic uncertainty from the fit for both $tu\gamma$ and $tc\gamma$ channels.

Systematic source	Applied on	type	$tu\gamma$ (%)	$tc\gamma$ (%)
Lumi	All MC	Rate	1.8	-4
Trigger scale factor	All MC	Rate+Shape	2.2	-0.4
Pile up scale factor	All MC	Rate+Shape	7	-2.3
Muon scale factor	All MC	Rate+Shape	-0.7	4.4
Photon scale factor	All MC	Rate+Shape	-1.9	-4.5
Photon energy scale	All MC	Rate+Shape	0.5	-3.1
btag and mistag	All MC	Rate+Shape	-1.1	4
Jet energy scale	All MC	Rate+Shape	2.9	-2.2
Jet energy resolution	All MC	Rate+Shape	2.1	-3.4
PDF	Signal	Rate+Shape	3.13	-0.6
Q-scale	Signal	Rate+Shape	0.9	-2.4
Top-mass	Signal	Rate+Shape	2.5	-1
Background normalization	W+jets	Rate	5.6	-3
Background normalization	W+γ+jets	Rate	2.5	-1.1
Background normalization	All MC	Rate	0.3	-1

The uncertainty on the normalization of the SM backgrounds is considered to affect the rate of these processes.

The impact of the systematic uncertainties on the result of the analysis is quantified by their relative impact on the expected cross-section upper limit. For each uncertainty, the limit is derived with and without including the corresponding nuisance parameter in the fit. The relative variation is defined by

$$\Delta\sigma_{exp} = \frac{\sigma_{exp}(\text{without nuisance}) - \sigma_{exp}(\text{with nuisance})}{\sigma_{exp}(\text{with nuisance})} \tag{5.18}$$

The relative variation of the expected cross-section limit obtained for the various uncertainties is listed in table 5.9 for both $tu\gamma$ and $tc\gamma$ channels. It can be seen from table 5.9 that removing sources of systematics leads to tighter upper bounds (negative value for $\Delta\sigma_{exp}$) for most of the uncertainties although it is not the case for all sources. This behaviour is mostly related to the statistical fluctuations and the smallness of the variations due to the certain systematic source. The BDT output for the $tu\gamma$ channel shows more powerful discrimination between signal and backgrounds compare to $tc\gamma$ channel. Therefore the shape and normalisation variations of the SM backgrounds due to the systematic uncertainties have smaller effects in $tu\gamma$ channel and the positive value for $\Delta\sigma_{exp}$ is more probable consequently.

5.8 Results

After estimating contributions of all SM backgrounds, taking into account all the SF and training BDT, the BDT output distributions for signal, backgrounds and data are shown in figure 5.27. As was discussed in section 5.3.1, independent BDTs are trained for $tu\gamma$ and $tc\gamma$ signal channels. It can be seen in figure 5.27 that the $tu\gamma$ and $tc\gamma$ signal distributions are well separated from the SM background distributions. Furthermore, the measured data is described well by the SM prediction in the whole range of the BDT output and there is no evidence for signal events in both channels.

The BDT output distributions of the data driven backgrounds (W-jets and $W\gamma$-jets) are shown separately while all MC estimated backgrounds are summed and shown in pink color in figure 5.27. All the systematic sources, mentioned in section 5.7, are summed quadratically and combined with statistical errors in each bin independently.

As no excess over the SM prediction is observed, we will constraint the contribution of the signal processes and top quark FCNC anomalous couplings consequently.

5.8.1 Limits

The results of these searches are published in reference [67]. The distribution of the BDT discriminant for data, SM backgrounds and signal are used to set upper limits on the signal cross sections. The limit setting procedure is performed using CLs method implemented in the theta framework [139]. The effects of systematic uncertainties on the BDT discriminant templates is modelled by varying each of the systematic sources $\pm 1\sigma$ in simulation and re-deriving the templates of the BDT discriminant. The systematic uncertainties which only change the rate of the background processes are considered on the background and signal normalizations. All systematic uncertainties are quantified as nuisance parameters with a Gaussian prior.

The 95% C.L. upper limits obtained from the shape analysis of the BDT output distributions for $tu\gamma$ and $tc\gamma$ signal are summarized in tables 5.10 and 5.11. The limit setting procedure for leading order and next to leading order is performed including the systematic uncertainties discussed in section 5.7 while the uncertainty on signal NLO corrections is removed for LO calculations.

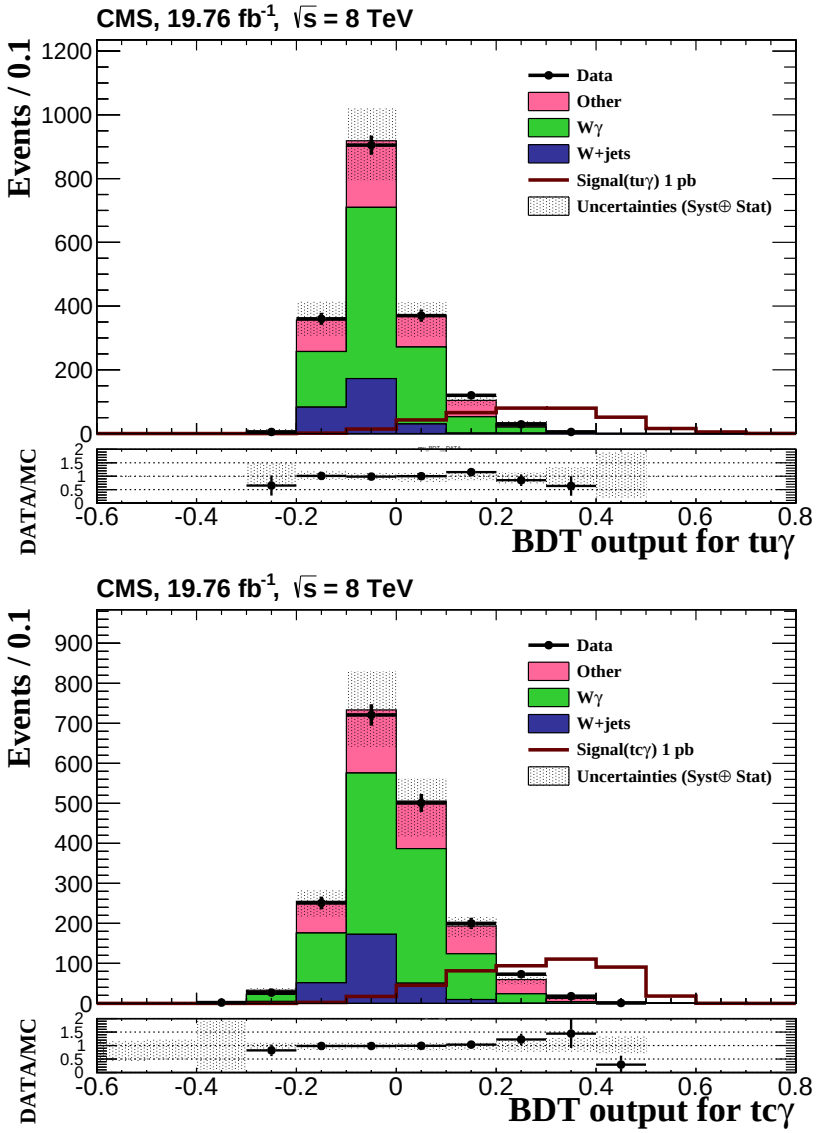

Figure 5.27: The BDT output distribution for data, all backgrounds, and tγu (left) and tγc (right). The W-jets and $W\gamma$-jets contributions are estimated from data. The $tu\gamma$ signal sample is normalized to a cross section of 1 pb. The error bands contain both systematics and statistical uncertainties.

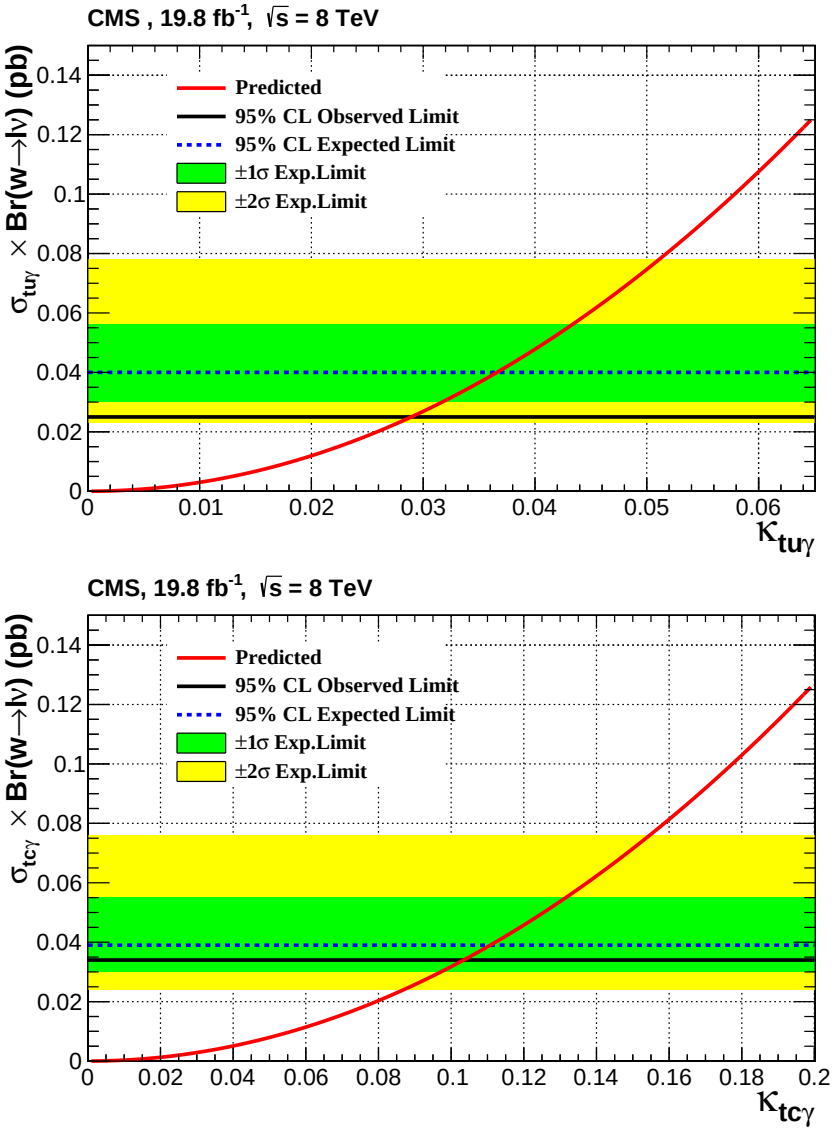

Figure 5.28: The 95% confidence level exclusion limit in terms of the anomalous couplings $tu\gamma$ (top) and $tc\gamma$ (bottom). Expected upper limit on the $\sigma_{tq\gamma} \times Br(W \rightarrow l\nu_l)$ is shown with dash line accompanied with one and two sigma error bands. Observed limit is shown with black line. Red curve shows the theoretical cross section as a function of the anomalous couplings.

Table 5.10: The observed and expected 95% exclusion limits on the signal cross section, anomalous couplings, and branching ratios at leading order.

	Exp. limit (LO)	Obs. limit (LO)
$\sigma_{tu\gamma} \times Br(W \to l\nu_l)$	0.040 pb	0.025 pb
$\sigma_{tc\gamma} \times Br(W \to l\nu_l)$	0.039 pb	0.034 pb
$\kappa_{tu\gamma}$	0.036	0.0279
$\kappa_{tc\gamma}$	0.111	0.094
$Br(t \to u\gamma)$	0.027%	0.017%
$Br(t \to c\gamma)$	0.25%	0.22%

As was discussed in section 5.1.1, the cross section of the anomalous production of single top quark in association with a photon is a function of anomalous couplings. Therefore, the upper limit on the cross sections are used to constrain the $tu\gamma$ and $tc\gamma$ anomalous couplings. In order to calculate the bounds at NLO, it is assumed that k-factor increase the cross section by a factor of 1.375 for both signal channels.

Table 5.11: The observed and expected 95% exclusion limits on the signal cross section, anomalous couplings, and branching ratios with including the QCD higher order corrections on the signal cross section.

	Exp. limit (NLO)	Obs. limit (NLO)
$\sigma_{tu\gamma} \times Br(W \to l\nu_l)$	0.039 pb	0.026 pb
$\sigma_{tc\gamma} \times Br(W \to l\nu_l)$	0.042 pb	0.037 pb
$\kappa_{tu\gamma}$	0.031	0.025
$\kappa_{tc\gamma}$	0.098	0.091
$Br(t \to u\gamma)$	0.019%	0.013%
$Br(t \to c\gamma)$	0.201%	0.17%

The limits on the anomalous couplings can easily be translated to upper bounds on the branching ratios of anomalous top decays using equation 5.4. Therefore, limits on the branching ratios of anomalous top decays obtained in this analysis are indirect limits which can be compared with the results of the direct searches.

It can be seen in tables 5.10 and 5.11 that the upper limits obtained on the $tu\gamma$ anomalous couplings and related branching ratio is stronger than corresponding $tc\gamma$ limits. It is due to the larger cross section of the $tu\gamma$ signal compared to $tc\gamma$ which is directly related to the larger PDF of up-quark compared to c-quark in proton. Therefore, the anomalous production of single top quark in association with a photon is more sensitive to $tu\gamma$ anomalous coupling. As was discussed in section 5.17, this feature enables us to discriminate between the anomalous $tu\gamma$ and $tc\gamma$ interactions

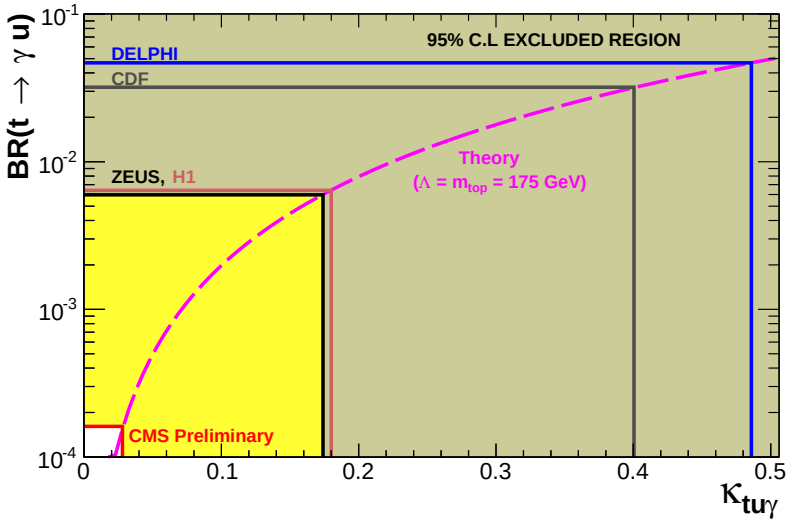

Figure 5.29: The comparison of the 95% CL exclusion limits in the $Br(t \to u\gamma) - k_{tu\gamma}$ plane from ZEUS, H1, DELPHI, CDF, and CMS experiments.

in case of discovery.

In figure 5.29, the results of this analysis are compared with previous results from other experiments in the $Br(t \to u\gamma) - k_{tu\gamma}$ plane. The excluded region by CMS results compared to the best upper bounds of the previous experiments is shown in yellow color. The upper limits on the top quark FCNC anomalous branching ratios obtained in this analysis has improved previous limit by around two orders of magnitude and is the most stringent limit to date.

Chapter 6

Fiducial cross sections

Obtained limits in this analysis which are given in previous section depend on our specific model which predicts the existence of anomalous $tq\gamma$ FCNC couplings. In this section, we provide upper limits as model independent as possible to allow comparison to an arbitrary theoretical prediction.

6.1 Motivations

The results of this analysis which leads to upper limit on the cross section of anomalous single top quark production in association with a photon ($\sigma_{tq\gamma}^{95\%}$) multiplied by leptonic branching ratio of the W boson decay ($\frac{1}{3}$) are calculated in a defined signal region firstly. Events in which a muon, a photon and an invisible particle (for example neutrino) are associated with QCD jets are selected to define a region in the total phase space of pp collisions called signal region. Then upper limits obtained in signal region (restricted phase space) are extrapolated to the total phase space using information extracted from signal models. Although our main purpose is searching for anomalous top quark FCNC coupling restricted phase space can be used to test other new physics models which leads to similar final state objects.

In order to see the dependency of the results to the $tq\gamma$ FCNC model clearly, we can define new variables. 'Visible cross section' is defined as:

$$\sigma_{vis}^{95\%} = \frac{N^{95\%}}{\mathcal{L}} \tag{6.1}$$

where $\sigma_{vis}^{95\%}$ is the 95% CL upper limit on the cross section of any new physics signal

inside the signal region, $N^{95\%}$ is upper limits at 95% CL on the number of new physics events inside the signal region and $\mathcal{L}$ is the integrated luminosity.

In our specific FCNC model, $\sigma_{vis}^{95\%}$ can be written as

$$\sigma_{vis}^{95\%} = \sigma_{tq\gamma}^{95\%} \times Br(W \to l\nu_l) \times A \tag{6.2}$$

A is the signal selection efficiency that accounts for the effect of selection cuts and detector inefficiencies and resolutions. The signal selection efficiencies are the ratio of the remaining events after all selection cuts to the total number of events before applying the cuts using the full leptonic samples which was discussed in section 5.

$$A = \frac{\text{number of events remained after all selection cuts}}{\text{total number of events}} \tag{6.3}$$

A is found to be 1.86% and 2.42% for $tu\gamma$ and $tc\gamma$ samples respectively (see table 5.6). Therefore, one can write

$$\sigma_{tq\gamma}^{95\%} \times Br(W \to l\nu_l) = \frac{\sigma_{vis}^{95\%}}{A} \tag{6.4}$$

It is clear that the upper limits on $\sigma_{tq\gamma}^{95\%} \times Br(W \to l\nu_l)$ given in table 5.10 depends on new physics model through the factor A. Because $\sigma_{vis}^{95\%}$ depends on the number of backgrounds, number of data and uncertainty on the number of background event in signal region if we consider a simple cut and count analysis (uncertainty on signal selection efficiency can also vary $\sigma_{vis}^{95\%}$ a bit which can be accounted for easily) and is independent of new physics model effects.

As was mentioned before, although the signal region defined in this analysis is optimised for the production of anomalous top quark in association with a photon through the FCNC interactions, this signal region can be used to test the signature of other new physics models which leads to the processes with muon, neutrino, b-jet and photon in final state. In other word, we should remove the dependency of the limits to the A factor as much as possible to make the results as model independent as possible. Therefore, $\sigma_{vis}^{95\%}$ is a value which is model independent and can be used to limit any arbitrary new physics models if be reported in experimental particle physics paper.

One should note that the detector level objects which are reconstructed from

detector response in various parts of the CMS detector are used to define signal region. Although reconstructed objects are originated from generated particles they are associated with many complicated detector effects which are known to a reasonable extent and are accounted for full simulation in this analysis. Therefore, if a phenomenologist is going to test a new physics model with the same final state (a muon, a photon, MET and jets) by $\sigma_{vis}^{95\%}$, it is necessary to redo these complicated detector simulation to extract needed information (A) for extrapolating the results from signal region to the total phase space and find the upper limit on the inclusive cross section of the new physics model ($\sigma_{new-physics}^{95\%} = \frac{\sigma_{vis}^{95\%}}{A}$).

For example in [140], authors try to develop global analysis at NLO in QCD of the most constraining limits on top-quark FCNC operators. In this paper many experimental results are examined to constrain the top-quark FCNC couplings in different final states. One of the important final states are single top and photon production channel. If the experimental results are presented in such a way that can be easily used by phenomenologists, the final state can be employed in addition to the results for checking different effects to the same signal (NLO effects, generator effects, ...) or testing other signal models.

Although $\sigma_{vis}^{95\%}$ is widely reported by experimental papers for various final states and is widely employed by phenomenalogist to constraint parameters space of new physics models, the complication of detector simulations and unclear detector inefficiencies makes the interpretation of results a bit vague [45, 141]. The most straightforward way to use experimental results are accessing to the fiducial cross sections. The idea is to report the measured cross section (or upper limit on the cross section) similar to σ_{vis} in a 'simple' restricted phase space. In addition, it is demanded to 'remove detector effects' to get rid of the complex detector simulations.

6.2 Fiducial phase space and cross section definitions

As was noted in previous subsection, model dependency of the results appears in factor A which includes the effects of both selection cuts and detector effects. The selection cut dependency can be removed significantly if we define a restricted phase space similar to the reconstructed signal region. The more similar restricted phase

space to reconstructed signal region the less model dependent results.

Restricted phase space can be defined in different level of events simulation. It could be defined at parton level using the hard interaction output particles which are easily available from matrix element generator. In this case, the effects of the final state radiations and hadronisation should also be removed from the results. On the other hand, final state radiation and fragmentation effects are easily available through general purpose event generators like PYTHIA and HERWIG [92, 93]. Events after final state radiations and fragmentations contain the list of particles that pass through the detector. Events at this step are called particle level events. Therefore, the restricted phase space can be defined in particle level without losing the simplicity of the results application.

Fiducial phase space is defined by applying a set of selection cuts on particle level events. Before listing fiducial phase space requirements, we need to define particle level objects like photon, muon, jets, etc. The photons and leptons are required not to originate from the decay of a hadron. So, lepton candidates are from W boson, Z boson or τ decays. Electrons or muons from τ decays must satisfy the same requirements as prompt leptons. The missing transverse momentum is defined as the vectorial sum of all neutrinos present in the event. Neutrinos from hadron decays are rejected. Jets are reconstructed from all particles with $c\tau > 10$ mm, excluding muons and neutrinos, using the anti-kt algorithm with a radius parameter of 0.5. Reconstructed particle-level jets are tagged using a B-hadron matching, where tagged means that at least one B-hadron is found within the jet. Top quark candidates are reconstructed using muon, MET and b-jet candidates as described in section 5.2.2. If no b-jet was found, the highest P_T jet is used to reconstruct the top quark.

Selected particle level candidates are used to define fiducial phase space which is summarized in table 6.1. It is tried to define a fiducial phase space similar to analysis reconstructed level signal region introduced in section 5 while cuts on more difficult variables like isolation requirements are removed.

In order to find the upper limit on the cross section of new physics in fiducial phase space defined in table 6.1, one should find a map from reconstructed level signal region in which we performed all analysis steps to this almost similar fiducial phase space. Signal selection efficiency for any arbitrary signal model can be written

Table 6.1: Definition of the fiducial region.

Object	Requirement
Single muon	$p_T > 26$ GeV, $\|\eta\| < 2.1$
Veto for additional muons	$p_T > 10$ GeV, $\|\eta\| < 2.5$
Electron veto	$p_T > 20$ GeV, $\|\eta\| < 2.5$
Single photon	$p_T > 50$ GeV, $\|\eta\| < 2.5$ ($1.44 < \|\eta\| < 1.56$ excluded)
At least one jet ($N_{\text{b-jet}} < 2$)	$p_T > 30$ GeV, $\|\eta\| < 2.5$
Missing p_T	$p_T^{\text{miss}} > 30$ GeV
Muon, jets, and photons	$\Delta R(\mu, \gamma)$ and $\Delta R(\text{jet}, \gamma) > 0.7$
Reconstructed top quark mass	$130 < m_{\mu\nu b} < 220$ GeV

as

$$A = \mathcal{A}\,\epsilon \tag{6.5}$$

where $\mathcal{A}$ is the fraction of number of generated signal events at particle level that can pass fiducial phase space requirements defined in table 6.1. It is defined as:

$$\mathcal{A} = \frac{\text{number of events remained in fiducial region}}{\text{total number of events}} \tag{6.6}$$

In equation 6.6, ϵ accounts for the difference between the fiducial phase space and reconstructed level signal region. Due to the similarity of fiducial phase space and signal region definition, ϵ is mostly related to detector inefficiencies and resolutions. Although ϵ seems to be independent of the input model signal characteristics in defined fiducial phase space can effects epsilon [142]. For example, a signal model with photon and jets mostly in barrel experiences different reconstruction efficiency compared to a new physics signal model with photon and jets mostly produced in endcaps. $\mathcal{A}$ and A can be calculated using particle level and full simulated samples, respectively. Therefore, ϵ, which is also denoted as ϵ_{fid}, can be written as

$$\epsilon_{fid} = \frac{A}{\mathcal{A}} \tag{6.7}$$

We can rewrite equation 6.4 using equation 6.5,

$$\sigma_{tq\gamma}^{95\%} \times Br(W \to l\nu_l) = \frac{\sigma_{vis}^{95\%}}{\mathcal{A}\,\epsilon} \tag{6.8}$$

$\mathcal{A}$ is different for each signal model while ϵ and $\sigma_{vis}^{95\%}$ are mostly model independent.

Therefore we can rewrite above equation in the following form

$$\sigma^{95\%}_{tq\gamma} \times \mathcal{A} = \frac{\sigma^{95\%}_{vis}}{\epsilon} \tag{6.9}$$

The value of $\frac{\sigma_{vis}}{\epsilon}$ is called fiducial cross section, σ_{fid}, which is independent of the input signal model to a reasonable extent and all detector effects are lifted.

$$\sigma^{95\%}_{fid} = \frac{\sigma^{95\%}_{vis}}{\epsilon_{fid}} \tag{6.10}$$

We summarize the way that a phenomenalogist can use σ_{fid} for a given fiducial phase space to constraint parameters space of an arbitrary new physics model with a similar final state below.

- find the cross section of new physics model in pp collisions as a function of the model parameters ($\sigma_{new-physics}$).
- generate events and include radiation and hadronization effects.
- apply fiducial phase space requirements and find factor $\mathcal{A}$.
- use ($\sigma_{new-physics}$(model parameters) = $\frac{\sigma_{fid}}{\mathcal{A}}$) to find constraint on new physics parameters.

6.3 Upper limits on fiducial cross sections

In this section upper limit on σ_{fid} is reported. In section 5, signal region is optimised for single top production in association with a photon and the SM contributions from different sources are estimated. In the defined signal region at the detector level, the BDT output distribution of the SM background, $tq\gamma$ signal and the observed data are shown in figure 5.27. Upper limits on the $\sigma_{tq\gamma} \times Br(W \to l\nu_l)$ obtained from shape analysis of the BDT outputs are shown in table 5.10. In table 5.10 upper limits on the cross sections are obtained from the upper limits on the number of signal events in signal region. Therefore, $\sigma^{95\%}_{vis-observed}$ can be found for both signal

channels as:

$$\sigma^{95\%}_{vis-observed}(tu\gamma) = \frac{N^{95\%}_{tu\gamma}}{\mathcal{L}} = \frac{9.12}{19.768} = 0.461 \quad (6.11)$$

$$\sigma^{95\%}_{vis-observed}(tc\gamma) = \frac{N^{95\%}_{tu\gamma}}{\mathcal{L}} = \frac{15.93}{19.768} = 0.806 \quad (6.12)$$

One expects to find $\sigma^{95\%}_{vis-observed}$ independent of the signal model in a defined signal region (considering same values for signal selection efficiency error) but the obtained values for $\sigma^{95\%}_{vis-observed}(tu\gamma)$ and $\sigma^{95\%}_{vis-observed}(tc\gamma)$ are not the same. The reason is that we have done shape analysis to set upper limits and the limits are sensitive to the shape of the BDT output for signal and SM backgrounds. Better separation between SM backgrounds and signal events more stringent upper limits on $\sigma^{95\%}_{vis}$. For example, the $tu\gamma$ signal is better separated from SM backgrounds compared to $tc\gamma$ signal and consequently $\sigma^{95\%}_{vis-observed}(tu\gamma)$ is more stringent than $\sigma^{95\%}_{vis-observed}(tc\gamma)$.

As was discussed, $\sigma^{95\%}_{vis-observed}(tu\gamma)$ and $\sigma^{95\%}_{vis-observed}(tc\gamma)$ can not be used for testing new physics models. On the other hand, they may be used for testing different aspects of the $tq\gamma$ processes such as the effects of the next to leading order to the $tq\gamma$ FCNC processes [140]. Therefore, in addition to the shape dependent upper limits which are given in equation 6.11, we can perform a counting analysis in the signal region to remove BDT shape dependency.

In the signal region, there are 1794 data events and 1805.44 ± 215 background events. One can find the upper limit on the visible cross section performing a simple counting analysis. Considering 10% uncertainty on the signal selection efficiency and using CLs method, one finds

$$\sigma^{95\%}_{vis-observed} = \frac{N^{95\%}}{\mathcal{L}} = \frac{384.92}{19.768} = 19.472 \ fb \quad (6.13)$$

Although this bound could be useful, it is a bit loose due to the applied loose selection cuts to define the signal region and the analysis suffers from large systematics uncertainties. The power of systematic uncertainties are reduced by an excellent signal discrimination power of BDT in the shape analysis. In order to report more useful results, additional requirement is imposed to define a more limited signal region. Events with no b-tagged jets are kept to be able to control the contribution of the W-jets and $W\gamma$-jets from data with enough statistics. After finding their contri-

butions in data, as was discussed in section 5, we can choose events with exactly one b-tagged jet. This requirement rejects the contribution of backgrounds considerably while keeping most of the signal events. In this region, there are 275 data events while 258.71 ± 49.5 background events are estimated. Considering 10% uncertainty on the signal selection efficiency and using CLs method, one can find $\sigma^{95\%}_{vis-observed}$ in the new signal region:

$$\sigma^{95\%}_{vis-observed} = \frac{N^{95\%}}{\mathcal{L}} = \frac{104.86}{19.768} = 5.305 \ fb \tag{6.14}$$

The total number of background events and the number of data events for both signal regions are reported in table 6.2. The uncertainties in the SM expectation include both statistical and systematic uncertainties. The total number of observed events is decreased by a factor of approximately 6.5 after requiring exactly one identified b jet in an event, while the expected number of SM events decreases by a factor of 7. The combined relative uncertainty in the number of expected SM events increases from 12% to 19% when this b jet requirement is included.

Table 6.2: The total number of observed selected events in the data (N_{obs}), the SM expectations (N_{SM}) in the fiducial region, without and with a requirement on the presence of a single accompanying b-jet.

Fiducial region	N_{obs}	N_{SM}
Basic selection (Table 6.1)	1794	1805 ± 215
Basic selection and $N_{\text{b jet}} = 1$	275	258 ± 49

In order to find $\mathcal{A}$, signal samples are generated and with initial conditions similar to those samples which are used for the detector level study. After simulating showering and hadronisation effects with PYTHIA, the selection cuts in table 6.1 are applied to find the number of remained events in the fiducial phase space. The values of $\mathcal{A}^{tq\gamma}$ are found to be:

$$\mathcal{A}^{tu\gamma} = 12.02\% \tag{6.15}$$

$$\mathcal{A}^{tc\gamma} = 12.63\% \tag{6.16}$$

The upper limits on the fiducial cross sections, visible cross sections, A, $\mathcal{A}$ and ϵ_{fid} are summarized in table 6.3 for the shape analysis of BDT output distributions and for the cut and count analysis in two given signal regions. Observed upper limits

on the cross section in a restricted phase space are found to be 122 fb and 102 fb at 95% CL for $tu\gamma$ and $tc\gamma$ production, respectively, when at most one identified b jet is required in the data. These limits are found to be 47 fb and 39 fb at 95% CL for $tu\gamma$ and $tc\gamma$ production, respectively, when exactly one identified b jet is required in the data.

Table 6.3: Model independent results in two fiducial region: 1- a region which is determined by the 'basic selection cuts' of this analysis 2- a region which is determined by the 'basic selection cuts' of this analysis and exactly one b-tag requirement. In fiducial region 1 we use two different method to set limits, shape analysis and counting analysis. The variables are: Upper limits on number of new physics events and cross section ($N^{95\%}_{observed}$ and $\sigma^{95\%}_{vis-observed}$) in fiducial region at detector level, signal selection efficiency at detector level (A) and particle level ($\mathcal{A}$), fiducial efficiency (ϵ_{fid}) and upper limits on the cross section of new physics model in fiducial region at particle level (fiducial cross section $\sigma^{95\%}_{fid-observed}$).

variables	channel	fiducial phase space and analysis type		
		basic selection cut shape analysis	basic selection counting analysis	basic selection+1 b counting analysis
$N^{95\%}_{observed}$	$tu\gamma$	9.08	384.92	104.86
	$tc\gamma$	15.96	384.92	104.86
$\sigma^{95\%}_{vis-observed}$	$tu\gamma$	0.46 fb	19.472 fb	5.305 fb
	$tc\gamma$	0.81 fb	19.472 fb	5.305 fb
A	$tu\gamma$	1.86%	1.86%	1.30%
	$tc\gamma$	2.42%	2.42%	1.71 %
$\mathcal{A}$	$tu\gamma$	11.60%	11.60%	11.45%
	$tc\gamma$	12.61%	12.61%	12.39%
ϵ_{fid}	$tu\gamma$	0.16	0.16	0.113
	$tc\gamma$	0.19	0.19	0.137
$\sigma^{95\%}_{fid-observed}$	$tu\gamma$	2.87 fb	121.70 fb	46.94 fb
	$tc\gamma$	4.26 fb	102.48 fb	38.72 fb

Chapter 7

Conclusion

In this thesis, we have presented a search for $tu\gamma$ and $tc\gamma$ FCNC interactions through the production of single top quark in association with a photon. The search is based on 19.8 fb^{-1} of proton-proton collision data collected with the Compact Muon Solenoid experiment during the 2012 run of the Large Hadron Collider at a center-of-mass energy of $\sqrt{s} = 8$ TeV. The muonic decay of the W boson from top quark decay is just considered in this analysis.

A multivariate analysis is performed to reach the best performance of the analysis after optimizing the preselection cuts. No excess over the SM background predictions is observed and 95 % C.L. upper limit is derived from a shape analysis on the BDT output on the signal cross sections. Upper bounds on the signal cross sections are used to constrain the anomalous $tu\gamma$ and $tc\gamma$ FCNC coupling and the related top quark branching ratios.

The results obtained in this analysis are compared to the previous limits obtained in different experiments in figure 7.1. The results on the anomalous top quark FCNC decay $Br(t \to qZ)$ are also shown on the vertical axis. It can be seen that the CMS results have improved the previous results by around one order of magnitude for both $Br(t \to q\gamma)$ and $Br(t \to qZ)$ using 8 TeV data. Although the SM predicts top quark anomalous branching ratios many order of magnitudes below the current experimental limits, experiments are closing to the regions which are predicted by some beyond SM models.

Run-ll is just beginning at a pp collision energy of 13 TeV, a significant increase compared to the LHC run-l. This new energy frontier will allow researchers to probe new boundaries of the fundamental structure of the matter. This increment

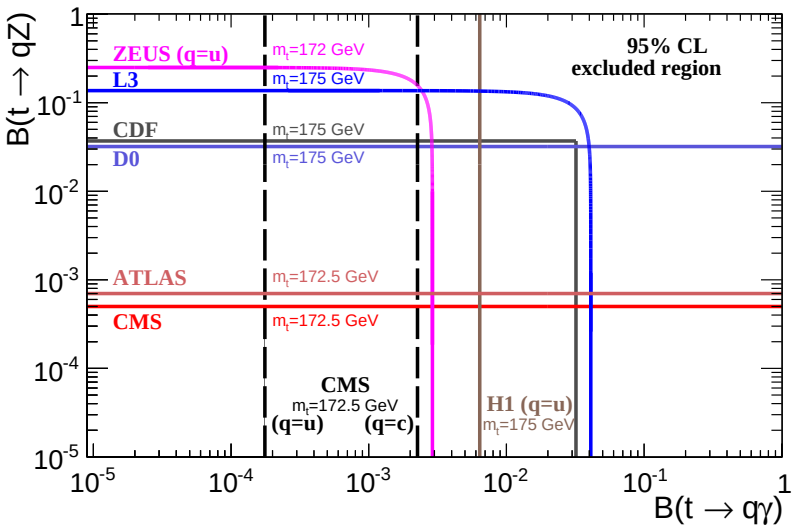

Figure 7.1: The comparison of the 95% CL exclusion limits in the $Br(t \to q\gamma) - Br(t \to qZ)$ plane from ZEUS, H1, DELPHI, CDF, and CMS experiments.

in energy enhances the cross section of the anomalous $t\gamma$ production by a factor of 2.5 and 3.1 for $tu\gamma$ and $tc\gamma$ signal channels, respectively. With this increase in cross sections, it is expected to reach the same exclusion limit by half of the data used in this analysis. However, higher luminosity at RUN 2 of the LHC leads to more pile-up which would effect the analysis reach.

Bibliography

[1] S. Glashow, J. Iliopoulos, and L. Maiani, *Weak Interactions with Lepton-Hadron Symmetry*, *Phys.Rev.* **D2** (1970) 1285–1292.

[2] J. Aguilar-Saavedra, *Top flavor-changing neutral interactions: Theoretical expectations and experimental detection*, *Acta Phys.Polon.* **B35** (2004) 2695–2710, [hep-ph/0409342].

[3] S. Bejar, J. Guasch, and J. Sola, *Loop induced flavor changing neutral decays of the top quark in a general two Higgs doublet model*, *Nucl.Phys.* **B600** (2001) 21–38, [hep-ph/0011091].

[4] J. Aguilar-Saavedra, *Effects of mixing with quark singlets*, *Phys.Rev.* **D67** (2003) 035003, [hep-ph/0210112].

[5] J. J. Liu, C. S. Li, L. L. Yang, and L. G. Jin, $t \to cV$ *via SUSY FCNC couplings in the unconstrained MSSM*, *Phys.Lett.* **B599** (2004) 92–101, [hep-ph/0406155].

[6] G.-r. Lu, F.-r. Yin, X.-l. Wang, and L.-d. Wan, *The Rare top quark decays* $t \to cV$ *in the topcolor assisted technicolor model*, *Phys.Rev.* **D68** (2003) 015002, [hep-ph/0303122].

[7] **ATLAS** Collaboration, *Physics at a High-Luminosity LHC with ATLAS*, *ATL-PHYS-PUB-2012-001* (Aug, 2012).

[8] **CDF , D0 , ATLAS , CMS** Collaboration, R. Goldouzian, *Search for FCNC in top quark production and decays*, [1412.2524].

[9] C. Zhang and S. Willenbrock, *Effective Field Theory for Top Quark Physics*, *Nuovo Cim.* **C033** (2010), no. 4 285–291, [arXiv:1008.3155].

[10] A. Pich, *The Standard Model of Electroweak Interactions*, [1201.0537].

[11] M. et al., *Standard Model of Elementary Particles*, *http://en.wikipedia.org/wiki/File:Standard_Model_of_Elementary_Particles.svg* (2014).

[12] T. Pham, *CKM Matrix Elements*, [1110.6050].

[13] **CDF** Collaboration, F. Abe *et. al.*, *Evidence for top quark production in $\bar{p}p$ collisions at $\sqrt{s} = 1.8$ TeV*, *Phys.Rev.Lett.* **73** (1994) 225–231, [hep-ex/9405005].

[14] **CDF** Collaboration, F. Abe *et. al.*, *Observation of top quark production in $\bar{p}p$ collisions*, *Phys.Rev.Lett.* **74** (1995) 2626–2631, [hep-ex/9503002].

[15] **D0** Collaboration, S. Abachi *et. al.*, *Observation of the top quark*, *Phys.Rev.Lett.* **74** (1995) 2632–2637, [hep-ex/9503003].

[16] G. L. Kane and M. E. Peskin, *A Constraint from B Decay on Models with No T Quark*, *Nucl.Phys.* **B195** (1982) 29.

[17] **ALEPH , CDF , D0 , DELPHI , L3 , OPAL , SLD , LEP Electroweak Working Group, Tevatron Electroweak Working Group, SLD Electroweak and Heavy Flavour Groups** Collaboration, *Precision Electroweak Measurements and Constraints on the Standard Model*, [1012.2367].

[18] **Particle Data Group** Collaboration, K. Olive *et. al.*, *Review of Particle Physics*, *Chin.Phys.* **C38** (2014) 090001.

[19] M. Jezabek and J. H. Kuhn, *QCD Corrections to Semileptonic Decays of Heavy Quarks*, *Nucl.Phys.* **B314** (1989) 1.

[20] C. Arzt, M. Einhorn, and J. Wudka, *Patterns of deviation from the standard model*, *Nucl.Phys.* **B433** (1995) 41–66, [hep-ph/9405214].

[21] W. Buchmuller and D. Wyler, *Effective Lagrangian Analysis of New Interactions and Flavor Conservation*, *Nucl.Phys.* **B268** (1986) 621–653.

[22] B. Grzadkowski, M. Iskrzynski, M. Misiak, and J. Rosiek, *Dimension-Six Terms in the Standard Model Lagrangian*, *JHEP* **1010** (2010) 085, [arXiv:1008.4884].

[23] J. Aguilar-Saavedra, *A Minimal set of top anomalous couplings*, *Nucl.Phys.* **B812** (2009) 181–204, [arXiv:0811.3842].

[24] P. Ferreira, R. Guedes, and R. Santos, *Combined effects of strong and electroweak FCNC effective operators in top quark physics at the CERN LHC*, *Phys.Rev.* **D77** (2008) 114008, [arXiv:0802.2075].

[25] P. J. Fox, Z. Ligeti, M. Papucci, G. Perez, and M. D. Schwartz, *Deciphering top flavor violation at the LHC with B factories*, *Phys.Rev.* **D78** (2008) 054008, [arXiv:0704.1482].

[26] C. Zhang, *Effective field theory approach to top-quark decay at next-to-leading order in QCD*, *Phys.Rev.* **D90** (2014), no. 1 014008, [arXiv:1404.1264].

[27] N. Cabibbo, *Unitary Symmetry and Leptonic Decays*, *Phys.Rev.Lett.* **10** (1963) 531–533.

[28] T. Mannel, *Effective Field Theories in Flavour Physics*. 2004.

[29] S. Bejar, J. Guasch, and J. Sola, *FCNC top quark decays beyond the standard model*, [hep-ph/0101294].

[30] C. S. Li, R. Oakes, and J. M. Yang, *Rare decay of the top quark in the minimal supersymmetric model*, *Phys.Rev.* **D49** (1994) 293–298.

[31] M. J. Duncan, *Flavor Changing Decays of the Z^0 and Supersymmetry*, *Phys.Rev.* **D31** (1985) 1139.

[32] J. Gunion and H. E. Haber, *Higgs Bosons in Supersymmetric Models. 1.*, *Nucl.Phys.* **B272** (1986) 1.

[33] G. Eilam, J. Hewett, and A. Soni, *Rare decays of the top quark in the standard and two Higgs doublet models*, *Phys.Rev.* **D44** (1991) 1473–1484.

[34] S. Bejar, J. Guasch, and J. Sola, *Loop induced flavor changing neutral decays of the top quark in a general two Higgs doublet model*, *Nucl.Phys.* **B600** (2001) 21–38, [hep-ph/0011091].

[35] F. del Aguila, J. Aguilar-Saavedra, and R. Miquel, *Constraints on top couplings in models with exotic quarks*, *Phys.Rev.Lett.* **82** (1999) 1628–1631, [hep-ph/9808400].

[36] I. Baum, G. Eilam, and S. Bar-Shalom, *Scalar flavor changing neutral currents and rare top quark decays in a two H iggs doublet model 'for the top quark'*, *Phys.Rev.* **D77** (2008) 113008, [arXiv:0802.2622].

[37] J. L. Lopez, D. V. Nanopoulos, and R. Rangarajan, *New supersymmetric contributions to $t \to c\ V$*, *Phys.Rev.* **D56** (1997) 3100–3106, [hep-ph/9702350].

[38] J. M. Yang, B.-L. Young, and X. Zhang, *Flavor changing top quark decays in r parity violating SUSY*, *Phys.Rev.* **D58** (1998) 055001, [hep-ph/9705341].

[39] **ATLAS** Collaboration, J. Carvalho *et. al.*, *Study of ATLAS sensitivity to FCNC top decays*, *Eur.Phys.J.* **C52** (2007) 999–1019, [arXiv:0712.1127].

[40] J. Gao, C. S. Li, L. L. Yang, and H. Zhang, *Search for anomalous top quark production at the early LHC*, *Phys.Rev.Lett.* **107** (2011) 092002, [arXiv:1104.4945].

[41] T. Han, M. Hosch, K. Whisnant, B.-L. Young, and X. Zhang, *Single top quark production via FCNC couplings at hadron colliders*, *Phys.Rev.* **D58** (1998) 073008, [hep-ph/9806486].

[42] F. del Aguila and J. Aguilar-Saavedra, *Multilepton production via top flavor changing neutral couplings at the CERN LHC*, *Nucl.Phys.* **B576** (2000) 56–84, [hep-ph/9909222].

[43] Y. Gouz and S. Slabospitsky, *Double top production at hadronic colliders*, *Phys.Lett.* **B457** (1999) 177–185, [hep-ph/9811330].

[44] M. Khatiri Yanehsari, S. Jafari, and M. Mohammadi Najafabadi, *Study of Two Top Production Through FCNC Anomalous Couplings at the LHC*, *Int.J.Theor.Phys.* **52** (2013) 4229–4236.

[45] R. Goldouzian, *Search for top quark flavour changing neutral currents in same-sign top quark production*, *Phys.Rev.* **D91** (2015) 014022, [arXiv:1408.0493].

[46] S. Khatibi and M. M. Najafabadi, *Probing the Anomalous FCNC Interactions in Top-Higgs Final State and Charge Ratio Approach*, *Phys.Rev.* **D89** (2014), no. 5 054011, [arXiv:1402.3073].

[47] **CDF** Collaboration, F. Abe *et. al.*, *Search for flavor-changing neutral current decays of the top quark in $p\bar{p}$ collisions at $\sqrt{s} = 1.8$ TeV*, *Phys.Rev.Lett.* **80** (1998) 2525–2530.

[48] **CDF** Collaboration, T. Aaltonen *et. al.*, *Search for the Flavor Changing Neutral Current Decay $t \to Zq$ in $p\bar{p}$ Collisions at $\sqrt{s} = 1.96$ TeV*, *Phys.Rev.Lett.* **101** (2008) 192002, [arXiv:0805.2109].

[49] **D0** Collaboration, V. M. Abazov *et. al.*, *Search for flavor changing neutral currents in decays of top quarks*, *Phys.Lett.* **B701** (2011) 313–320, [arXiv:1103.4574].

[50] **D0** Collaboration, V. Abazov *et. al.*, *Search for production of single top quarks via tcg and tug flavor- changing neutral current couplings*, *Phys.Rev.Lett.* **99** (2007) 191802, [hep-ex/0702005].

[51] **CDF** Collaboration, T. Aaltonen *et. al.*, *Search for top-quark production via flavor-changing neutral currents in W+1 jet events at CDF*, *Phys.Rev.Lett.* **102** (2009) 151801, [arXiv:0812.3400].

[52] S. Moretti and K. Odagiri, *Single top production at future ep colliders*, *Phys.Rev.* **D57** (1998) 3040–3050, [hep-ph/9709435].

[53] **ZEUS** Collaboration, S. Chekanov *et. al.*, *Search for single top production in ep collisions at HERA*, *Phys.Lett.* **B559** (2003) 153–170, [hep-ex/0302010].

[54] **H1** Collaboration, A. Aktas *et. al.*, *Search for single top quark production in ep collisions at HERA*, *Eur.Phys.J.* **C33** (2004) 9–22, [hep-ex/0310032].

[55] **ZEUS** Collaboration, H. Abramowicz *et. al.*, *Search for single-top production in ep collisions at HERA*, *Phys.Lett.* **B708** (2012) 27–36, [arXiv:1111.3901].

[56] **H1** Collaboration, F. Aaron *et. al.*, *Search for Single Top Quark Production at HERA*, *Phys.Lett.* **B678** (2009) 450–458, [arXiv:0904.3876].

[57] **OPAL** Collaboration, G. Abbiendi *et. al.*, *Search for single top quark production at LEP-2*, *Phys.Lett.* **B521** (2001) 181–194, [hep-ex/0110009].

[58] **L3** Collaboration, P. Achard *et. al.*, *Search for single top production at LEP*, *Phys.Lett.* **B549** (2002) 290–300, [hep-ex/0210041].

[59] **DELPHI** Collaboration, J. Abdallah *et. al.*, *Search for single top production via FCNC at LEP at* $\sqrt{s}$ *= 189-GeV to 208-GeV*, *Phys.Lett.* **B590** (2004) 21–34, [hep-ex/0404014].

[60] **ALEPH** Collaboration, A. Heister *et. al.*, *Search for single top production in* e^+e^- *collisions at* $\sqrt{s}$ *up to 209-GeV*, *Phys.Lett.* **B543** (2002) 173–182, [hep-ex/0206070].

[61] A. Quadt, *Top Quark Physics at Hadron Colliders*. 2006.

[62] **ATLAS** Collaboration, *Detector and physics performance technical design report Volume 1,2*, *CERN-LHCC-99-15, ATLAS-TDR-15* (1999).

[63] **CMS** Collaboration, G. Bayatian *et. al.*, *CMS technical design report, volume II: Physics performance*, *J.Phys.* **G34** (2007) 995–1579.

[64] **ATLAS** Collaboration, G. Aad *et. al.*, *Search for flavour-changing neutral current top-quark decays to qZ in pp collision data collected with the ATLAS detector at* $\sqrt{s} = 8$ *TeV*, arXiv:1508.0579.

[65] **CMS** Collaboration, S. Chatrchyan *et. al.*, *Search for Flavor-Changing Neutral Currents in Top-Quark Decays* $t \to Zq$ *in pp Collisions at* $\sqrt{s} = 8\,TeV$, *Phys.Rev.Lett.* **112** (2014), no. 17 171802, [arXiv:1312.4194].

[66] **CMS** Collaboration, *Search for Flavour Changing Neutral Currents in single top events*, *CMS-PAS-TOP-12-021* (2013).

[67] **CMS** Collaboration, *Search for anomalous single top quark production in association with a photon in pp collisions at sqrt(s) = 8 TeV*, *Submitted to JHEP* (2015) [arXiv:1511.0395].

[68] **CMS** Collaboration, *Search for anomalous Wtb couplings and top FCNC in t-channel single-top-quark events*, *CMS-PAS-TOP-14-007* (2014).

[69] **ATLAS** Collaboration, *Search for single top-quark production via FCNC in strong interaction in* $\sqrt{s} = 8$ TeV *ATLAS data*, *ATLAS-CONF-2013-063, ATLAS-COM-CONF-2013-064* (2013).

[70] L. Evans and P. Bryant, *LHC Machine*, *JINST* **3** (2008) S08001.

[71] **CMS** Collaboration *https://twiki.cern.ch/twiki/bin/view/CMSPublic/LumiPublicResultsPAS*.

[72] **ATLAS** Collaboration, G. Aad *et. al.*, *The ATLAS Experiment at the CERN Large Hadron Collider*, *JINST* **3** (2008) S08003.

[73] **CMS** Collaboration, S. Chatrchyan *et. al.*, *The CMS experiment at the CERN LHC*, *JINST* **3** (2008) S08004.

[74] **ALICE** Collaboration, K. Aamodt *et. al.*, *The ALICE experiment at the CERN LHC*, *JINST* **3** (2008) S08002.

[75] **LHCb** Collaboration, J. Alves, A. Augusto *et. al.*, *The LHCb Detector at the LHC*, *JINST* **3** (2008) S08005.

[76] J.-L. Caron, "Overall view of LHC experiments.. Vue d'ensemble des experiences du LHC.." AC Collection. Legacy of AC. Pictures from 1992 to 2002., May, 1998.

[77] **LHCf** Collaboration, O. Adriani *et. al.*, *The LHCf detector at the CERN Large Hadron Collider*, *JINST* **3** (2008) S08006.

[78] **TOTEM** Collaboration, G. Anelli *et. al.*, *The TOTEM experiment at the CERN Large Hadron Collider*, *JINST* **3** (2008) S08007.

[79] **CMS** Collaboration, *CMS Physics: Technical Design Report Volume 1: Detector Performance and Software*. Technical Design Report CMS. CERN, Geneva, 2006.

[80] **CMS** Collaboration, S. Chatrchyan *et. al.*, *Commissioning and Performance of the CMS Pixel Tracker with Cosmic Ray Muons*, *JINST* **5** (2010) T03007, [arXiv:0911.5434].

[81] **CMS** Collaboration, V. Veszpremi, *Operation and performance of the CMS tracker*, *JINST* **9** (2014) C03005, [arXiv:1402.0675].

[82] **CMS ECAL** Collaboration, W. Lustermann, *The electromagnetic calorimeter of CMS, summary and status*, *J.Phys.Conf.Ser.* **160** (2009) 012044.

[83] **CMS** Collaboration, S. Chatrchyan *et. al.*, *Energy Calibration and Resolution of the CMS Electromagnetic Calorimeter in pp Collisions at* $\sqrt{s} = 7$ *TeV*, *JINST* **8** (2013) P09009, [arXiv:1306.2016].

[84] **CMS** Collaboration, *Search for Heavy Stable Charged Particles with 100 inverse picobarns and 1 inverse femtobarn in the CMS experiment*, .

[85] **CMS** Collaboration, S. Chatrchyan *et. al.*, *Performance of the CMS Hadron Calorimeter with Cosmic Ray Muons and LHC Beam Data*, *JINST* **5** (2010) T03012, [arXiv:0911.4991].

[86] **CMS** Collaboration, *The CMS hadron calorimeter project: Technical Design Report*. Technical Design Report CMS. CERN, Geneva, 1997.

[87] **CMS** Collaboration, S. Chatrchyan *et. al.*, *Precise Mapping of the Magnetic Field in the CMS Barrel Yoke using Cosmic Rays*, *JINST* **5** (2010) T03021, [arXiv:0910.5530].

[88] **CMS** Collaboration, S. Chatrchyan *et. al.*, *The performance of the CMS muon detector in proton-proton collisions at sqrt(s) = 7 TeV at the LHC*, *JINST* **8** (2013) P11002, [arXiv:1306.6905].

[89] R. Placakyte, *Parton Distribution Functions*, arXiv:1111.5452.

[90] J. Stirling, *Parton luminosity and cross section plots*, *http://www.hep.ph.ic.ac.uk/ wstirlin/plots/plots.html*.

[91] A. Buckley, J. Butterworth, S. Gieseke, D. Grellscheid, S. Hoche, *et. al.*, *General-purpose event generators for LHC physics*, *Phys.Rept.* **504** (2011) 145–233, [arXiv:1101.2599].

[92] G. Corcella, I. Knowles, G. Marchesini, S. Moretti, K. Odagiri, *et. al.*, *HERWIG 6: An Event generator for hadron emission reactions with*

interfering gluons (including supersymmetric processes), *JHEP* **0101** (2001) 010, [hep-ph/0011363].

[93] T. Sjostrand, S. Mrenna, and P. Z. Skands, *PYTHIA 6.4 Physics and Manual*, *JHEP* **0605** (2006) 026, [hep-ph/0603175].

[94] T. Gleisberg, S. Hoeche, F. Krauss, A. Schalicke, S. Schumann, *et. al.*, *SHERPA 1. alpha: A Proof of concept version*, *JHEP* **0402** (2004) 056, [hep-ph/0311263].

[95] M. L. Mangano, M. Moretti, F. Piccinini, R. Pittau, and A. D. Polosa, *ALPGEN, a generator for hard multiparton processes in hadronic collisions*, *JHEP* **0307** (2003) 001, [hep-ph/0206293].

[96] S. Alioli, P. Nason, C. Oleari, and E. Re, *A general framework for implementing NLO calculations in shower Monte Carlo programs: the POWHEG BOX*, *JHEP* **1006** (2010) 043, [arXiv:1002.2581].

[97] F. Maltoni and T. Stelzer, *MadEvent: Automatic event generation with MadGraph*, *JHEP* **0302** (2003) 027, [hep-ph/0208156].

[98] **CTEQ** Collaboration, R. Brock *et. al.*, *Handbook of perturbative QCD: Version 1.0*, *Rev.Mod.Phys.* **67** (1995) 157–248.

[99] J. C. Collins, *Sudakov form-factors*, *Adv. Ser. Direct. High Energy Phys.* **5** (1989) 573–614, [hep-ph/0312336].

[100] B. Andersson, G. Gustafson, G. Ingelman, and T. Sjostrand, *Parton Fragmentation and String Dynamics*, *Phys.Rept.* **97** (1983) 31–145.

[101] **CMS** Collaboration, S. Chatrchyan *et. al.*, *Description and performance of track and primary-vertex reconstruction with the CMS tracker*, *JINST* **9** (2014), no. 10 P10009, [arXiv:1405.6569].

[102] E. Chabanat and N. Estre, *Deterministic annealing for vertex finding at CMS*, .

[103] **CMS** Collaboration, *Particle-Flow Event Reconstruction in CMS and Performance for Jets, Taus, and MET*, Tech. Rep. CMS-PAS-PFT-09-001, CERN, 2009. Geneva, Apr, 2009.

[104] **CMS** Collaboration, V. Khachatryan *et. al.*, *Performance of photon reconstruction and identification with the CMS detector in proton-proton collisions at* $\sqrt{s} = 8$ *TeV*, arXiv:1502.0270.

[105] E. Meschi, T. Monteiro, C. Seez, and P. Vikas, *Electron Reconstruction in the CMS Electromagnetic Calorimeter*, .

[106] M. Cacciari, G. P. Salam, and G. Soyez, *FastJet User Manual*, *Eur.Phys.J.* **C72** (2012) 1896, [arXiv:1111.6097].

[107] M. Cacciari and G. P. Salam, *Pileup subtraction using jet areas*, *Phys.Lett.* **B659** (2008) 119–126, [arXiv:0707.1378].

[108] **CMS** Collaboration, V. Khachatryan *et. al.*, *Performance of electron reconstruction and selection with the CMS detector in proton-proton collisions at* $\sqrt{s} = 8$ *TeV*, arXiv:1502.0270.

[109] **CMS** Collaboration, *Performance of muon identification in pp collisions at* $\sqrt{s} = 7$ *TeV*, .

[110] **CMS** Collaboration, S. Chatrchyan *et. al.*, *Performance of CMS muon reconstruction in pp collision events at* $\sqrt{s} = 7$ *TeV*, *JINST* **7** (2012) P10002, [arXiv:1206.4071].

[111] G. P. Salam, *Towards Jetography*, *Eur.Phys.J.* **C67** (2010) 637–686, [arXiv:0906.1833].

[112] M. Cacciari, G. P. Salam, and G. Soyez, *The Anti-k(t) jet clustering algorithm*, *JHEP* **0804** (2008) 063, [arXiv:0802.1189].

[113] **CMS** Collaboration, *Plans for Jet Energy Corrections at CMS*, .

[114] **CMS** Collaboration, S. Chatrchyan *et. al.*, *Determination of Jet Energy Calibration and Transverse Momentum Resolution in CMS*, *JINST* **6** (2011) P11002, [arXiv:1107.4277].

[115] **CMS** Collaboration, S. Chatrchyan *et. al.*, *Identification of b-quark jets with the CMS experiment*, *JINST* **8** (2013) P04013, [arXiv:1211.4462].

[116] **CMS** Collaboration, V. Khachatryan *et. al.*, *Performance of the CMS missing transverse momentum reconstruction in pp data at* $\sqrt{s} = 8$ *TeV*, *JINST* **10** (2015), no. 02 P02006, [arXiv:1411.0511].

[117] **CMS** Collaboration, S. Chatrchyan *et. al.*, *Missing transverse energy performance of the CMS detector*, *JINST* **6** (2011) P09001, [arXiv:1106.5048].

[118] J. A. Aguilar-Saavedra, *Zt, gamma t and t production at hadron colliders via strong flavour-changing neutral couplings*, *Nucl. Phys. B* **837** (2010) 122.

[119] Y. Zhang, B. H. Li, C. S. Li, J. Gao, and H. X. Zhu, *Next-to-leading order QCD corrections to the top quark associated with* γ *production via model-independent flavor-changing neutral-current couplings at hadron colliders*, *Phys.Rev.* **D83** (2011) 094003, [arXiv:1101.5346].

[120] *https://twiki.cern.ch/twiki/bin/view/CMS/MuonReferenceEffs*.

[121] J. M. Campbell, R. K. Ellis, and C. Williams, *Vector boson pair production at the LHC*, *JHEP* **1107** (2011) 018, [arXiv:1105.0020].

[122] K. Melnikov and F. Petriello, *Electroweak gauge boson production at hadron colliders through O(alpha(s)**2)*, *Phys.Rev.* **D74** (2006) 114017, [hep-ph/0609070].

[123] S. Alioli, P. Nason, C. Oleari, and E. Re, *NLO single-top production matched with shower in POWHEG: s- and t-channel contributions*, *JHEP* **0909** (2009) 111, [arXiv:0907.4076].

[124] N. Kidonakis, *Differential and total cross sections for top pair and single top production*, arXiv:1205.3453.

[125] U. Baur, T. Han, and J. Ohnemus, *QCD corrections to hadronic* $W\gamma$ *production with nonstandard* $WW\gamma$ *couplings*, *Phys.Rev.D* **48** (1993) 5140.

[126] V. Abramov, D. Konstantinov, S. Slabospitsky, M. M. Najafabadi, A. Giammanco, R. Tenchini, E. Boos, L. Dudko, V. Savrin, A. Sherstnev, S. Kalinin, and A. A. Drozdetsky, *Selection of Single Top Events with the*

CMS Detector at LHC, Tech. Rep. CMS-NOTE-2006-084, CERN, Geneva, May, 2006.

[127] **CMS** Collaboration, S. Chatrchyan *et. al.*, *Measurement of the t-channel single top quark production cross section in pp collisions at* $\sqrt{s} = 7$ *TeV*, *Phys. Rev. Lett.* **107** (2011) 091802, [arXiv:1106.3052].

[128] P. Speckmayer, A. Hocker, J. Stelzer, and H. Voss, *The toolkit for multivariate data analysis, TMVA 4*, *J.Phys.Conf.Ser.* **219** (2010) 032057.

[129] Y. Freund and R. Schapire, *A Decision-Theoretic Generalization of On-Line Learning and an Application to Boosting* , *journal of computer and system sciences* **55** (1997) 119.

[130] S. Haykinl, *Neural Networks and Learning Machines*. 1994.

[131] D. Wlodzislaw and H. D. Geerd, *Neural networks as tools to solve problems in physics and chemistryr*, *Computer Physics Communications* **82** (1994) 91.

[132] *https://twiki.cern.ch/twiki/bin/view/CMS/MuonTagAndProbe*.

[133] **CMS** Collaboration, *CMS Luminosity Based on Pixel Cluster Counting - Summer 2013 Update*, Tech. Rep. CMS-PAS-LUM-13-001, CERN, Geneva, 2013.

[134] **CMS** Collaboration, S. Chatrchyan *et. al.*, *Measurement of the inelastic proton-proton cross section at* $\sqrt{s} = 7$ *TeV*, *Phys. Lett.* **B722** (2013) 5–27, [arXiv:1210.6718].

[135] **CMS** Collaboration, V. Khachatryan *et. al.*, *Measurements of Inclusive W and Z Cross Sections in pp Collisions at* $\sqrt{s} = 7$ *TeV*, *JHEP* **01** (2011) 080, [arXiv:1012.2466].

[136] **CMS** Collaboration, S. Chatrchyan *et. al.*, *Measurement of the* $W\gamma$ *and* $Z\gamma$ *inclusive cross sections in pp collisions at* $\sqrt{s} = 7$*??TeV and limits on anomalous triple gauge boson couplings*, *Phys. Rev.* **D89** (2014), no. 9 092005, [arXiv:1308.6832].

[137] T. C. collaboration, *Determination of jet energy calibration and transverse momentum resolution in CMS*, *Journal of Instrumentation* **6** (2011), no. 11.

[138] M. Botje, J. Butterworth, A. Cooper-Sarkar, A. de Roeck, J. Feltesse, *et. al.*, *The PDF4LHC Working Group Interim Recommendations*, arXiv:1101.0538.

[139] T. Muller, J. Ott, and J. Wagner-Kuhr, *Theta - a framework for template based modelling and inference*, *CMS Internal Note* **CMS-IN 2010/017** (2010).

[140] G. Durieux, F. Maltoni, and C. Zhang, *Global approach to top-quark flavor-changing interactions*, *Phys. Rev.* **D91** (2015), no. 7 074017, [arXiv:1412.7166].

[141] **CMS** Collaboration, S. Chatrchyan *et. al.*, *Search for new physics in events with same-sign dileptons and b jets in pp collisions at* $\sqrt{s} = 8$ *TeV*, *JHEP* **03** (2013) 037, [arXiv:1212.6194]. [Erratum: JHEP07,041(2013)].

[142] **ATLAS** Collaboration, G. Aad *et. al.*, *Search for new phenomena in events with three or more charged leptons in pp collisions at* $\sqrt{s} = 8$ *TeV with the ATLAS detector*, *JHEP* **08** (2015) 138, [arXiv:1411.2921].